DEVELOPMENT AND CHARACTERIZATION OF TRANSITION METAL
PHOSPHIDE MATERIALS FOR ELECTROCHEMICAL CAPACITORS AND
OER CATALYSIS

A THESIS SUBMITTED TO
THE GRADUATE SCHOOL OF NATURAL AND APPLIED SCIENCES
OF
MIDDLE EAST TECHNICAL UNIVERSITY

BY

KADİR ÖZGÜN KÖSE

IN PARTIAL FULFILLMENT OF THE REQUIREMENTS
FOR
THE DEGREE OF DOCTOR OF PHILOSOPHY
IN
METALLURGICAL AND MATERIALS ENGINEERING

May 2024

Approval of the thesis:

DEVELOPMENT AND CHARACTERIZATION OF TRANSITION METAL PHOSPHIDE MATERIALS FOR ELECTROCHEMICAL CAPACITORS AND OER CATALYSIS

submitted by **KADİR ÖZGÜN KÖSE** in partial fulfillment of the requirements for the degree of Doctor of Philosophy **in** Metallurgical and Materials Engineering**, Middle East Technical University** by,

Prof. Dr. Naci Emre Altun
Dean, **Graduate School of Natural and Applied Sciences**

Prof. Dr. Ali Kalkanlı
Head of the Department, **Metallurgical and Materials Eng, METU**

Prof. Dr. M. Kadri Aydınol
Supervisor, **Metallurgical and Materials Eng, METU**

Examining Committee Members:

Prof. Dr. H. Emrah Ünalan
Metallurgical and Materials Eng, METU

Prof. Dr. M. Kadri Aydınol
Metallurgical and Materials Eng, METU

Assoc. Prof. Dr. Burak Ülgüt
Chemistry, Bilkent University

Assoc. Prof. Dr. Batur Ercan
Metallurgical and Materials Eng, METU

Assist. Prof. Dr. Şahin Coşkun
Metallurgical and Materials Eng, ESOGÜ

Date: 17.05.2024

I hereby declare that all information in this document has been obtained and presented in accordance with academic rules and ethical conduct. I also declare that, as required by these rules and conduct, I have fully cited and referenced all material and results that are not original to this work.

Name Last name : Kadir Özgün Köse

Signature :

ABSTRACT

DEVELOPMENT AND CHARACTERIZATION OF TRANSITION METAL PHOSPHIDE MATERIALS FOR ELECTROCHEMICAL CAPACITORS AND OER CATALYSIS

Köse, Kadir Özgün
Doctor of Philosophy, Metallurgical and Materials Engineering
Supervisor : Prof. Dr. Mehmet Kadri Aydınol

May 2024, 101 pages

The pursuit of optimal energy utilization necessitates the exploration of new storage mechanisms and the enhancement of existing ones, driven by dwindling energy resources. Consequently, both academic and industrial efforts have intensified to refine electrochemical energy storage tools such as fuel cells, metal-air batteries, and electrochemical capacitors (EC). While electrochemical capacitors are typically recognized as low-energy high-power devices, fuel cells and metal-air batteries boast exceptional energy densities. Active material development plays a pivotal role in all these systems. Transition metal phosphides (TMPs) have emerged as a promising class of materials for above-mentioned electrochemical energy storage systems.

Electrochemical capacitors primarily rely on the electrostatic accumulation of ions at electrode surfaces during charging. Scientists have struggled to increase their energy density by exploring alternative materials, including phosphides known for their high electrical conductivity. This study focuses on decorating activated carbon (AC) surfaces with TMP particles to create composite structures, aiming to boost both specific capacitance and power density. Investigating the effects of bimetallic

TMP composites further expands the understanding of their potential in EC applications.

The Oxygen Evolution Reaction (OER) is crucial in fuel cells and metal-air batteries, directly influencing their performance by controlling over oxygen generation at the cathode. Efficient OER catalysts are pivotal for energy conversion efficiency and durability enhancement. Transition metal phosphides demonstrate promising catalytic activity, stability, and conductivity in OER-based systems, highlighting their potential for widespread implementation in renewable energy technologies, particularly in conjunction with AC/TMP composites In this study, this promising class of materials synthesized and utilized as OER catalysts.

Keywords: Electrochemical capacitors, OER catalysis, AC/TMP composite synthesis

ÖZ

ELEKTROKİMYASAL KAPASİTÖRLER VE OER KATALİZİ İÇİN GEÇİŞ METALİ FOSFİTLERİNİN GELİŞTİRİLMESİ VE KARAKTERİZASYONU

Köse, Kadir Özgün
Doktora, Metalurji ve Malzeme Mühendisliği
Tez Yöneticisi: Prof. Dr. Mehmet Kadri Aydınol

Mayıs 2024, 101 sayfa

Optimum enerji kullanımı arayışı, azalan enerji kaynakları nedeniyle yeni depolama mekanizmalarının araştırılmasını ve mevcut olanların geliştirilmesini gerektirmektedir. Sonuç olarak, yakıt hücreleri, metal-hava bataryaları ve elektrokimyasal kapasitörler (EC) gibi elektrokimyasal enerji depolama araçlarını geliştirmek için hem akademik hem de endüstriyel çabalar yoğunlaşmıştır. Elektrokimyasal kapasitörler genellikle düşük enerjili, yüksek güçlü cihazlar olarak tanınırken, yakıt hücreleri ve metal-hava pilleri olağanüstü enerji yoğunluklarına sahiptir. Aktif malzeme geliştirme tüm bu sistemlerde çok önemli bir rol oynamaktadır. Geçiş metali fosfitleri (TMP'ler), yukarıda bahsedilen elektrokimyasal enerji depolama sistemleri için umut verici bir malzeme sınıfı olarak ortaya çıkmıştır.

Elektrokimyasal kapasitörler öncelikle şarj sırasında elektrot yüzeylerinde iyonların elektrostatik birikmesine dayanır. Araştırmacılar, yüksek elektrik iletkenlikleri ile bilinen fosfitler de dahil olmak üzere alternatif malzemeleri keşfederek enerji yoğunluklarını artırmaya çalışmışlardır. Bu çalışma, hem spesifik kapasitansı hem de güç yoğunluğunu artırmayı amaçlayan kompozit yapılar oluşturmak için aktif

karbon (AC) yüzeylerinin TMP parçacıklarıyla dekore edilmesine odaklanıyor. Bimetalik TMP kompozitlerin etkilerinin araştırılması, bunların EC uygulamalarındaki potansiyellerinin anlaşılmasını daha da genişletecektir.

Oksijen Yükseltgenme Reaksiyonu (OER), katottaki oksijen üretimini yöneterek performanslarını doğrudan etkileyen yakıt hücreleri ve metal-hava pillerinde çok önemlidir. Verimli OER katalizörleri, enerji dönüşüm verimliliğini ve sistem dayanıklılığını artırmak için çok önemlidir. Geçiş metali fosfitleri, OER bazlı sistemlerde umut verici katalitik aktivite, stabilite ve iletkenlik sergileyerek, özellikle AC/TMP kompozitleri ile birlikte yenilenebilir enerji teknolojilerinde yaygın uygulama potansiyellerini vurgulamaktadır.

Anahtar Kelimeler: Elektrokimyasal kapasitörler, OER katalizi, AC/TMP kompozit sentezi

To my wife

ACKNOWLEDGMENTS

TABLE OF CONTENTS

LIST OF TABLES

LIST OF FIGURES

FIGURES

CHAPTER 1

INTRODUCTION

The development of new energy storage devices holds keen importance in addressing the energy challenges confronting the world today. These devices play an eminent role in enabling the efficient integration of renewable energy sources like solar and wind into the power grid by storing unused energy for times of high demand or low generation. Moreover, advanced energy storage technologies can amplify grid stability, reduce leaning on fossil fuels, and mitigate the intermittency issues inherent in renewable energy production. By opening the door for the transition towards a more sustainable and resilient energy infrastructure, innovative energy storage solutions have the potential to remarkably decrease carbon emissions and pave the way towards a cleaner, more sustainable energy future for all.

Among these systems, electrochemical capacitors (supercapacitors) distinguish themselves with their prominent power densities, whereas batteries and fuel cells find utility in applications demanding high energy density. Despite their extensive use, batteries incur a high cost per unit of energy, despite their superior energy densities compared to electrochemical capacitors. Particularly, asymmetric electrochemical capacitors with aqueous electrolytes show a promising alternative due to their cost-effectiveness and higher energy densities relative to electrical double layer capacitors. Achieving efficient electrochemical capacitors hinges on increasing the device's energy density without compromising power density or cycling stability. Research in this area typically aims at optimizing active material synthesis and utilization to meet these objectives.

The diagram labeled as Figure 1 is generally referred to as a Ragone plot, demonstrating specific power against specific energy, providing insight into the

energy and power characteristics of an energy storage device. It is evident that supercapacitors are supreme in power characteristics compared to batteries, albeit with lower energy densities. This discrepancy stems from the charge storage mechanisms: batteries rely on redox reactions for energy, which come across kinetic barriers such as ion diffusion to the electrode surface and electron transfer at the electrode. On the other hand, electrochemical double-layer capacitors (EDLC) operation is based on ion accumulation at the double layer, which generates non-faradaic current. The broad region occupied by electrochemical capacitors on the plot is due to the potential for enhanced energy densities through the introduction of rapid redox reactions, illustrating the principle of pseudo-capacitors. Additionally, hybrid configurations extra enhance energy density, with the utilization of Li^+ intercalation anodes proceeding towards battery-like energy densities.

Among the various energy systems driven by electrochemical reactions, fuel cells, water splitting, and metal-air batteries protrude as the simplest, most efficient, and reliable classifications. These systems utilize core reactions such as the water oxidation reaction or oxygen evolution reaction to clear the way for their reversible processes, besides the oxygen reduction reaction (ORR) and/or hydrogen evolution reaction (HER). In the OER, molecular oxygen is generated through several proton/electron-coupled procedures. This reaction is highly dependent on pH, with acidic and neutral conditions bring about the oxidation of two water molecules into four protons and an oxygen molecule, while in alkaline environments, hydroxyl groups experience oxidation to form H_2O and O_2. The equilibrium half-cell potentials (E°) at 1 atm and 25°C for OER are as follows:

$4\ OH^- \leftrightarrow 2\ H_2O(l) + O_2(g) + 4e^-$ E° = 0.404 V alkaline solution

$2\ H_2O(l) \leftrightarrow 4H^+ + O_2(g) + 4e^-$ E° = 1.23 V acidic solution
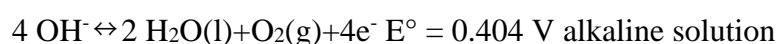
The generation of an O_2 molecule requires the transfer of four electrons, and the favorable kinetics of the OER typically arise through multi-step reactions, each including single-electron transfers. Consequently, energy augmentation at each step

contributes to stagnant OER kinetics and remarkable overpotential. Thus, an electrocatalyst with high activity becomes inevitable to surmount this energy barrier. Ideally, an electrocatalyst employed in OER should exhibit minimal overpotential, exceptional stability, and a small Tafel slope.
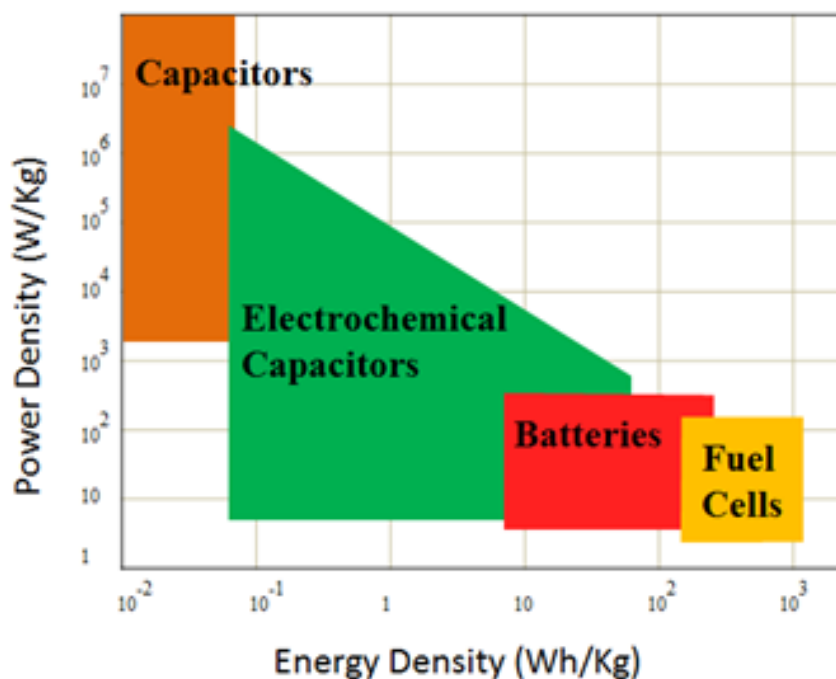
Figure 1. Ragone plot for different electrochemical systems.

Activated carbon materials are widely utilized in electrochemical capacitors due to their extraordinary properties. These materials highlight a highly porous structure with a large specific surface area, which enables the rapid adsorption and desorption of ions. This substantial specific surface area, combined with good electrical conductivity, enables activated carbon to store noteworthy amounts of energy through electrostatic charge accumulation at the electrode-electrolyte interface. Moreover, activated carbon materials are cost-effective, stable in both acid and alkaline conditions, and environmentally benign, making them one of the best choices for high-performance, sustainable electrochemical capacitors. Their

versatility gives rise to various modifications and functionalizations to further enhance their capacitance and energy density, addressing the growing request for efficient energy storage solutions.

Transition metal phosphide (TMP) materials are receiving attention for use in electrochemical capacitors due to their unique electrochemical properties. These materials, exhibit high electrical conductivity and outstanding electrochemical activity, making them suitable for energy storage applications. TMP's hold a robust structure that increases the charge storage capacity and cycle stability of electrochemical capacitors. They are capable of facilitating rapid charge and discharge processes, owing to their ability to form conductive networks and support facile ion transport. They have intrinsically higher electrical conductivities as compared to their oxide and hydroxide counterparts, due to the delocalized M-P bonds having metalloid characteristics. As a result, they showed improved capacitive response when compared to the transition metal oxides. Moreover, capacitive properties can be further increased with the utilization of the second transition metal and having bimetallic TMP structure. Since transition metals such as Co has also reversible redox reactions in alkaline media, their incorporation into TMP is beneficial regarding the capacitive response.

Above mentioned intrinsic properties of TMP materials makes them promising catalysts for OER due to their remarkable electrochemical properties and stability. TMP's enable the formation of key intermediate products necessary for OER, and their structure can transform into active oxide or hydroxide phases under reaction conditions, further improving their catalytic performance. The synergistic interaction between the metal and phosphorus atoms in TMP's assist to lower the overpotential and enhance the reaction kinetics. Moreover, TMPs are considered as durable and corrosion resistant in alkaline media, which are crucial for long term stability. Furthermore, utilization of two or more transition metals in TMP (bimetallic TMP) brings about two (or more) catalytically active center for OER, further increasing the OER catalytic activity. Research continues to optimize the composition and

morphology of TMPs to maximize their efficacy as OER catalysts, contributing to the development of efficient and sustainable water-splitting technologies.

Carbon composites have also increased attention for both electrochemical capacitors and OER catalysis. The high surface area and good conductivity of activated carbon improve the electrochemical performance of TMPs, leading to improved charge storage and rapid ion transport in EC's. This composite material supports the robust catalytic activity of TMPs for OER, enabling efficient formation of intermediate products and lowering overpotential. Moreover, the AC matrix supports the dispersion of TMP nanoparticles, suppressing agglomeration and assuring a more uniform and active catalytic surface. The combination of these materials results in composites that exhibit high capacitance, good cycle stability, and enhanced catalytic efficiency, making them highly effective for advanced electrochemical capacitors and OER catalysts.

After emphasizing the importance of the material group chosen for both the electrochemical capacitor and OER catalysis, it would be appropriate to emphasize the AC/TMP material production strategy, which contributes significantly to the originality of the thesis work. It has been seen in previous studies conducted by our group that after biomass is activated with phosphoric acid and activated carbon is obtained, a significant amount of surface phosphorus functionals remain on the carbon surface. These phosphorus functionals remaining on the surface served as precursor materials for the production of transition metal phosphide by impregnating transition metal salts and subjecting them to a second heat treatment. In this way, the activated carbon surface is decorated with transition metal phosphides. To the best of our knowledge, this method has not been tried before. This original strategy constitutes the main framework of the production of the composite structured material group in the thesis study.

Active material system chosen for this study, transition metal phosphides (TMP) and activated carbon (AC), were utilized in both EC and OER catalyst applications and exceptional results were published. Besides, AC is not only the most widely applied

material in EC, especially in EDLC studies, but also a well-known catalyst support for OER catalysis research. Thus, bifunctional AC/TMP active material synthesis and utilization in both EC and OER catalyst is aimed at this study. Besides, bimetallic TMP's were developed and utilized for both electrochemical applications to obtain the synergistic effect.

In the first part of the current study, it is aimed to produce AC/TMP composites for EC fabrication (in aqueous electrolyte) and OER catalyst. Transition metal used in this part of the study is Ni. Production of this composite is based on the surface phosphorus groups of the phosphoric acid AC's; no another phosphorus source is used. This provides us an efficient and facile way to produce active materials. By this way, it is aimed to increase specific capacitance and energy density of the bare AC's. Also, power and possibly energy density of TMP will be tried to increase, as a result of fine dispersion of TMP's and electrical conductivity enhancement. It is expected that having a composite structure will impose a synergistic effect and efficient active materials can be produced.

In the second part of the study, AC/bimetallic TMP's were produced and tried in EC with aqueous electrolyte and OER catalyst. Ni was kept constant, the other transition metals are Co, Mn, Fe and Cu. The aim was maintaining the Ni_2P crystal structure and systematically investigate the effect of the second element for both EC and OER catalyst application. The production method was the same as in the first part. In this stage of the study, AC was the same for all samples to simplify the parameters. Bimetallic TMP phases were produced on the surface of AC and utilized in the EC fabrication and OER catalysis. The phase, morphology and catalyst loading of the samples are performance determining; therefore, suitable phases with favorable morphologies are intended to be produced with proper methods. Especially if the amount of TMP on AC surface can be increased, the performance of the active materials produced by this method is promising.

6

In the third part of the study, Ni$_x$CoP samples were synthesized and their electrochemical properties were characterized in both EC and OER catalysis applications. Although there are lots of studies on TMP's, the nature of redox reactions that occurs during cycling is unclear. Therefore, the purpose of the current study is preparation and characterization of AC/TMP composites and bare TMP's, as well as their reaction mechanisms in EC utilization.

CHAPTER 2

LITERATURE REVIEW

2.1. TMP Development in EC and OER Catalyst Studies

2.1.1. TMP Development in EC Studies

There are numerous studies based on the utilization of TMP's as active materials for EC. The capacitive performance of the TMP varies as a result of change in transition metal, production method, morphology and size of the TMP, electrolyte used etc. Transition metals commonly applied in these studies include Ni [1–3] , Cu [4–6], Co [7–9]. Also, there are numerous synthesis methods including hydrothermal/solvothermal synthesis, thermal phosphidation, hydrothermal/solvothermal synthesis followed by phosphidation, high energy ball milling, electrodeposition. Red/white phosphorus, NaH_2PO_2 and $(NH_4)_2(HPO_4)$ are the main phosphorus sources for TMP production.

2.1.2. Synthesis Methods for TMP Materials

The synthesis methods have a huge impact on the physical properties of the TMP materials, such as size and morphology of the particles. The physical properties of the TMP affect the electrochemical response. Thus, the production method has a particular importance on the final performance of the TMP active materials. As a consequence, the synthesis methods are eloborated in the following sections.

2.1.2.1. Hydrothermal or Solvothermal Synthesis

Hydrothermal synthesis is an inorganic material production method, in which water soluble transition metal salts are subjected to high pressure via a pressurized vessel at elevated temperatures. In a typical synthesis route, a phosphorus supplying precursor (red/white phosphorus, sodium hypophosphite etc.) is mixed with a transition metal salt like nitrate or chloride in water. This solution is placed in a pressurized reactor, and the process is conducted at a temperature greater than 100 °C. The size and morphology control is typically obtained with the utilization of a surfactant such as CTAB or SDS. Solvothermal synthesis is conducted in a similar manner, except different solvents such as alcohol, ammonia or DMF are utilized.

There are numerous studies based on hydrothermal/solvothermal synthesized TMP' EC applications. In one of them, bimetallic NiCoP nanoparticles were produced by hydrothermal method at 200 °C for 10 hours. The resulting active materials yielded 571 C/g specific capacity at 1 A/g [10]. In another study, $Ni_{12}P_5$ hollow nanocapsules were synthesized via hydrothermal method with Ni acetate and red phosphorus precursors. The resulting materials showed 949 F/g specific capacitance at 1 A/g [11]. In the study of Ding et al.[12], the solvothermal method was utilized, with a solution of water and DMF. The obtained active material (Ni_8Co_1P) was mesoporous with 257 m^2/g surface area, and showed 1448 F/g specific capacitance.

2.1.2.2. Thermal Phosphidation

Thermal decomposition of a phosphorus source such as NaH_2PO_2, $(NH_4)_2(HPO_4)$ is utilized in this method. Typically, transition metal salts like chlorides or nitrates are placed in one end of a quartz tube, and the phosphorus source to be decomposed is placed in the other end. The process is conducted under inert atmosphere, and the flow of the inert gas (typically Ar) is arranged from phosphorus source to the transition metal salt. By the decomposition of the phosphorus source, PH_3 gas forms

and this gas is used for the phosphidation process. The annealing temperature is around 300 °C. Although this method is facile, poisonous PH_3 gas formation is a major drawback[13].

2.1.2.3. Hydrothermal or Solvothermal Synthesis Followed by Phosphidation

In this method, hydrothermal or solvothermal synthesis is used for the production of precursors such as transition metal hydroxides or carbonate hydroxides. The obtained powders are utilized as precursors for TMP production, in which a gaseous phosphidation method is applied afterwards. The size and morphology of the final active materials are dependent on the precursors produced by hydrothermal or solvothermal method. As a result, size and morphology controlling strategies are frequently applied for the hydroxide precursor production. Furthermore, phosphidation treatment parameters and transition metal to phosphidation source amount are regarded as two critical parameters[14]. In one of the studies making use of this strategy, $Ni(SO_4)_{0.3}(OH)_{1.4}$ nanobelt precursors were produced via hydrothermal method, and this material was heat treated at 300 °C with NaH_2PO_2 under Ar atmosphere[15]. The resulting product (Ni_2P) had 1074 F/g specific capacitance at 0.625 A/g. In another study, NiCoOH precursors were synthesized via hydrothermal treatment at 120 °C for 6 h, and then heat treated at 350 ° C with NaH_2PO_2 under Ar atmosphere [16]. As a result, NiCoP product after phosphidation treatment showed 653 C/g at 1 A/g. Moreover, urchin like NiCoP hollow spheres were produced via similar procedure [17]. In this study, Ni-Co carbonate hydroxide was produced via solvothermal route, in which water and ethanol soltion was used as solvent. Then, obtained precursor was heat treated with NaH_2PO_2 under inert atmosphere to produce NiCoP phase. The prepared material had 761 C/g specific capacity at 1 A/g.

2.1.2.4. High Energy Ball Milling

High energy ball milling is a mechanochemical method, not only utilized for TMP synthesis, but also suitable for other ceramic materials [18]. In this method, the precursor materials put in a grinding medium, which is generally covered by stainless steel or zirconia balls rotating at high speed. Ball milling typically produces low crystalline materials with high defect content. As a result, post annealing treatment is necessary in TMP material synthesis. Controlling the chemical composition by varying the precursor material ratio is straightforward by this method. Ball to precursor ratio, rotation speed and processing time are the main parameters to be adjusted for particular applications. In a study conducted by Wang et al.[2], Ni phosphide phase (either Ni_2P or Ni_5P_4) was controlled by the post annealing parameters. As a consequence, Ni_2P and Ni_5P_4 showed 843 and 801 F/g specific capacitance, respectively.

2.1.2.5. Electrodeposition

The electrodeposition method is a versatile technique for preparing TMP's without causing pollution and detrimental effects of phosphine (PH_3) gas. In a typical experiment, a conductive substrate serves as the working electrode, while an electrolyte containing metal salts and NaH_2PO_2 supplies the metal ions and phosphorus source. The resulting TMP grown substrate such as nickel foam and carbon cloth can then be directly used as a EC electrode. This method provides a binder free electrode, which is beneficial for both electrical conductivity and active surface utilization. In a study by Zhang et al. [19], Mn-CoP nanosheets were synthesized on nickel foam by a facile electrodeposition method. The researchers used an electrodeposition bath consisting of transition metal nitrate salts, urea and sodium hypophosphite as phosphorus source. The obtained electrode had 456 C/g specific capacity at 0.5 A/g. Moreover, Ni phosphide supported by carbon cloth was produced by Chebrolu et al. [20]. The electrodeposition bath was consisting of

transition metal nitrate, sodium hypophosphite and 3-mercaptopropionic acid (3-MPA). It was claimed that the presence of 3-MPA increased the electrical conductivity of the active material. The produced electrode showed 227 F/g specific capacitance at 0.5 A/g. Furthermore, bimetallic amorphous Ni-Co-P thin film electrodes on nickel foam was produced by electrodeposition [21]. In this study, an aqueous solution of transition metal chlorides, sodium hypophosphite, boric acid and sodium chloride was used as electrodeposition bath. Consequently, the electrodes show 42.2 mAh/g specific capacity at 1 A/g.

As one can see in Table 1 below, all TMP production methods have advantages and disadvantages. To summarize, methods based on thermal phosphidation are problematic due to the use of toxic phosphine gas, while hydrothermal methods are problematic due to the risk of explosion and low yield. In addition, contamination from the balls and vessels during high energy ball milling creates problems with uniform chemical composition. Additionally, particle crystallinity, size and morphology are difficult to control in this method. Although electrodeposition stands out among these methods with its scalability and low cost, it is not a universal method that can be used in every application due to its difficulty in deposition control and not being suitable for every substrate. As a result, it is clear that it is necessary to find a novel method in TMP production that will eliminate the problems mentioned here.

2.1.3. Charge Storage in TMP Materials in Alkaline Media

Among TMP's, Ni_2P is the most widely applied one in EC studies, due to both high specific capacitance and good electronic conductivity. When comparing the conductivities of NiO and Ni_2P, the variance can be attributed to the discrepancy in the binding energies of Ni $2p_{3/2}$ and P $2p_{3/2}$ in Ni_2P compared to oxidized species like Ni_xO and P_2O_5. Consequently, Ni-P bonds exhibit greater delocalization in nickel phosphides, leading to significantly enhanced conductivity compared to their oxide

counterparts. In Ni-based electrode materials, the storage of charge in an alkali environment is attributed to the Ni^{2+}/Ni^{3+} pair, which can be elucidated by the following equations:

$$Ni^{2+} + 2OH^- = Ni(OH)_2$$
$$Ni(OH)_2 + OH^- = NiOOH + H_2O + e^-$$

Table 1. Comparison of TMP production methods.

TMP Production Methods	Advantages	Disadvantages
Hydrothermal or Solvothermal Synthesis	High crystallinity and purity Controlled morphology & size Low temperature synthesis	High pressure (explosion risk) Low yield Long reaction times
Thermal Phosphidation	Easy processing Simple powder mixing High yield	Protective atmosphere requirement Poisonous PH_3 gas formation Uncontrollable size & morphology
Hydrothermal/Solvothermal + Phosphidation	Microstructure control High performing materials	Risks related to thermal phosphidation Complicated processing
High Energy Ball Milling	Nano-sized active materials Easy compositional control Low temperature operation	Poor crystallinity of active materials Contamination risks Wide particle size distribution
Electrodeposition	Uniformly coated material synthesis Scalability Low cost	Difficult control of composition Complex electrolyte management Substrate dependence

In a study on Ni phosphide application in EC, amorphous Ni-P is synthesized and argued that loose structure of it is favorable for diffusion of the electrolyte and it improves the power performance. The specific capacitance was 1597 F/g at 0.5 A/g. An asymmetric capacitor with negative electrode of AC was fabricated and 29.2 Wh/kg at 400 W/kg was achieved. In experiments evaluating Ni_2P and Ni_5P_4 as electrode materials for EC, Ni_2P exhibited superior electrochemical performance, demonstrating higher specific capacitance, improved rate capability, and enhanced stability compared to Ni_5P_4. In the study of Zhou et al.[1], first $Ni(OH)_2$ was produced on Ni foam with a hydrothermal process. Then, a low temperature phosphorization process was applied. By this way, Ni_2P nanoarrays were successfully prepared on Ni foam.

Bimetallic TMP research on EC has been focused on Ni and Co transition metals. As TMP phases typically serve as positive electrodes in hybrid capacitors utilizing aqueous alkali electrolytes, the primary strategy involves combining and leveraging the synergistic effects of these transition metals in an alkali environment. In one of these studies, an asymmetric capacitor was built using the $Co_xNi_{1-x}P$ active material [22]. This phase was formed on carbon nanofibers. It is suggested that the notable increase in capacitance/capacity observed in $Co_xNi_{1-x}P$/CNF, in contrast to monometallic NiP/CNF and CoP/CNF, is due to the heightened density of states near the Fermi level. In another investigation, the advantages of bimetallic "NiCoP" electrode systems are outlined as follows: (1) The Ni-Co-P configuration typically enhances overall Faradaic performance due to its intrinsic metalloid characteristics, boasting high electrical conductivity and a dense distribution of electro-active centers. (2) The higher conductivity of bimetallic phosphide materials primarily stems from the ease of delocalization in the metal sub-lattice within the phosphides. (3) Phosphorus, being a low electronegative element, facilitates the existence of various redox couples within heterogeneous metal phosphides. For NiCoP, this

commonly involves Ni^{2+}/Ni^{3+} and Co^{2+}/Co^{3+} redox couples, consequently augmenting the energy density of the bimetallic TMP compound [23].

2.2. TMP Materials in OER Catalysis

2.2.1. OER Catalysis Mechanisms on TMP Materials in Alkaline Media

In an alkaline environment, the abundance of OH^- ions reduces the energy needed to break the O-H bond compared to breaking two O-H bonds in acidic conditions. This facilitates the formation of key intermediates, OH* and O*, during OER. Consequently, the catalyst exhibits high OER activity under alkaline conditions[24]. For industrial electrolysis of water, corrosive environments are to be avoided; therefore, 1M KOH is more suitable for this application. On the other hand, metal-air batteries typically reside in the upper limits of the alkaline environment mainly to increase electrolyte conductivity[25]. For these cases, 6M KOH is a more suitable electrolyte choice.

Following two key aspects become critical to enhance the performance of an electrocatalysts: the number of active sites and the intrinsic activity of these sites. To increase the number of active sites, they often adjust the catalyst's surface area, size, and morphology, as well as enhance the contact area between the catalyst and the electrolyte. To improve the intrinsic activity, they explore methods to bring the OER potential closer to the thermodynamic limit, based on a thorough understanding of the OER mechanism.

2.2.2. Phase Transformation on TMP Materials in OER Conditions

Although the exact reaction mechanism of the OER process is not well understood, numerous experiments have demonstrated that metal-based phosphides transform

into corresponding oxides or hydroxides during OER, which are the true active species. This transformation may occur within electrochemical scanning cycles during OER operation[26]. Interestingly, the OER catalytic performance of transition metal phosphides often surpasses that of their oxides or hydroxides[27]. This could be because phosphating helps the active metal center convert into a more catalytically active oxide/hydroxide phase near the conductive platform[28]. Additionally, the active OER species can form heterostructures with phosphate species, facilitating electron transfer and enhancing the OER process[29]. The presence of phosphorus species also dilutes the density of metal atoms, weakens metal-metal bond strength, and aids the coupling of intermediates with metal atoms[30]. The elongation of the metal-phosphorus bond in TMPs accelerates the oxidation of metal atoms at high potentials, leading to the formation of metal oxide or hydroxide shells[31]. The internal TMP core acts as a conductive scaffold for these active sites[32]. For instance, oxides formed by TMP and metal create a TMP/MO_x core-shell structure, where the TMP core serves as a catalyst center and stabilizes the shell, and the MO_x shell accelerates the oxidation of intermediates and serves as an active site for OER[33]. This structure enhances OER catalysis. Additionally, the formation of an amorphous oxide/hydroxide phase may also enhance catalytic activity.

2.2.3. TMP Based OER Catalyst Development Studies

Considering OER catalysis applications, the most widely used TMP structures are based on transition metals Co, Ni and Mn [34]. For example, Zhu and colleagues utilized electrodeposition to create well-defined mesoporous arrays of CoP nanorods on Ni foam, which resulted in outstanding electric connectivity and improved mass transport [35]. The alteration of Co^{2+} oxidation state from 2 to higher states implies the dominant role of cobalt in achieving high activity. Similarly, phosphides based on Ni and Mn, such as NiP, Ni_2P, and MnP, have been explored for OER, albeit with limited studies available. Recent research has notably enhanced their performances through morphology and porosity modulation, as well as combining them with

various materials. Yu et al. produced carbon-coated porous nickel phosphide (NiP) nanoplates from MOFs, incorporating Ni_2P and Ni_5P_4 mixed phases [36]. They also synthesized NiO and $Ni(OH)_2$ porous nanoplates from the same precursor with similar morphology for comparison, revealing NiP's superior and stable activity. In another investigation, Stern et al. demonstrated that Ni_2P nanoparticles could serve as an excellent OER catalyst (290 mV at 10 mA/cm^2) in 1 M KOH solution [37]. In another study, the core-shell structured $Ni_{12}P_5/Ni_3(PO_4)_2$ hollow spheres demonstrate high activity and stability for both HER and OER in strong alkaline media. In 1 M KOH, they achieve a current density of 10 mA/cm^2 at an overpotential of 114 mV for HER and 318 mV for OER[38].

Bimetallic TMP structures were also tried in electrocatalysis applications. Bimetallic TMP structures exhibit adjustable energy levels and electron filling within their resulting electronic band structures, leading to diverse surface synergistic chemistry and optimized catalytic activities for the electrochemical OER. In one of the studies based on above mentioned logic, NiMP nanoparticles were produced, and it was observed that the crystal structure of Ni_2P is not deteriorated [39]. As a second element, Fe, Mn, Co and Mo were tried. It was claimed that their catalytic performances are comparable to that of RuO_2, which is accepted as the best one. Among these phases, NiFeP demonstrates the most superior performance. This finding was attributed to a synergistic effect; the robust Fe-O bond promotes the adsorption of OH-, with the oxyhydroxide formation primarily occurring on Fe to generate Fe-O, followed by Ni catalyzing the rupture of the Ni-O bond for O_2 formation.

Bimetallic TMPs, particularly those incorporating nickel and cobalt, exhibit remarkable catalytic activity in the oxygen evolution reaction [40,41]. Additionally, various transition metals are introduced into these phosphides to create bimetallic TMPs, further enhancing OER activity by altering electronic structure and bond coordination. Among the transition metals frequently combined with Ni and Co phosphides in bimetallic TMP catalysts are Fe [42,43] and Mn [44,45]. In one study, NiCoP

18

microflowers displayed a 314 mV overpotential at a current density of 10 mA/cm^2 and a Tafel slope of 68 mV/dec, maintaining stable behavior over 12 hours of chronoamperometry [46]. Furthermore, dispersed nanoscale NiFeP exhibited a 270 mV OER overpotential at 10 mA/cm^2 current density with a Tafel slope of 60 mV/dec [47].

2.3. AC Based Composites in EC and OER Catalysis Studies

2.3.1. AC and Carbon Based Composite Development in EC Studies

Enhancing energy and power density constitutes a pivotal focus in the advancement of electrochemical capacitor technology, with various methodologies aimed at achieving this objective. One such approach involves supplementing the primary active material, AC with additional active materials [48]. The production of AC generally includes a carbon source (mostly biomass) and two different activation mechanisms: physical and/or chemical activation [49]. In physical activation, the carbon source is initially carbonized and subsequently activated using CO_2 or H_2O gas. Conversely, chemical activation entails impregnating the carbon source with an activating agent such as $ZnCl_2$, KOH, or H_3PO_4, followed by heat treatment under an inert atmosphere. Both routes yield a high surface area and moderately conductive active material by the process's conclusion.

The characteristics of activated carbon (AC) play a pivotal role in shaping the final attributes of electrochemical capacitors (EC) utilizing AC-based composite active materials. Specific capacitance and rate capability of the device hinge upon the pore size and distribution of the AC. Ideal carbon electrodes possess a hierarchical pore arrangement, comprising larger macropores that serve as reservoirs for ion buffering, mesopores ranging from 2 to 50 nanometers facilitating ion transport, and nanopores smaller than 2 nanometers, which enhance charge storage. While nanoporous AC bolsters specific capacitance, mesopores with larger sizes and shorter ion diffusion lengths can diminish ion transport barriers, thereby enhancing power characteristics.

Optimization of pore structure involves maximizing pore volume for energy storage, establishing suitable ion transport channels for swift ion carriage into the electrode, and ensuring active pore walls to augment specific capacitance. [50].

Although the methods mentioned above yield nanoporous structures with activated carbons (AC), their textural and physicochemical properties exhibit significant variations. For instance, it has been argued that the activation temperature and impregnation ratio are the most crucial parameters affecting the properties of $ZnCl_2$ activated carbons. [51]. The same parameters are also effective for phosphoric acid activation. Besides, surface is rich in phosphorus in phosphoric acid activated carbons, and the enhancement of activation temperature increases the surface functional group content of the AC's [52]. This phenomenon not only impacts the adsorption properties of the activated carbon (AC), but these functionalities can also serve as a source of phosphorus for reducing metal ions and producing transition metal phosphides (TMPs).

One of the good examples on utilization of AC matrix composite studies is on NiO. This substance exhibits elevated specific capacity and structural robustness, qualifying it for use as a positive electrode in a hybrid electrochemical configuration. NiO composites offer significant advantages over pure NiO, particularly in electrical conductivity and electrochemical stability, attributed to the beneficial synergistic effects of integrating NiO within the carbonaceous network. [53]. Incorporating NiO into AC electrodes enhances the specific capacity, leveraging the porous morphology of AC to optimize the exposure of metal oxides to the electrolyte solution. In some instances, specific capacitance can increase up to fivefold compared to pristine oxide materials.

Carbon based composite structures were also tried for TMP's in EC fabrication. In a study conducted by An et al.[54], Ni_2P particles were synthesized on reduced graphene oxide (rGO) and tested in EC. In this study, the performances of bare Ni_2P and Ni_2P

on rGO were compared. Firstly, Ni_2P was synthesized from NiS_2 and it was decorated on GO and then reduced. The maximum specific capacitance (at 5 mA/cm^2) of bare Ni_2P was calculated as 1505 $F.g^{-1}$, whereas that of Ni_2P/rGO composite was calculated as 2266 $F.g^{-1}$ at the same current density. The authors attribute the Ni_2P/rGO composite's superior performance to three reasons. Firstly, production route of the composite structure enables so called "molecular level dispersion of Ni_2P, providing higher interaction area. Secondly, Ni_2P being on the graphene sheets, provides electron superhighways and increases the conductivity. Finally, this composite structure excludes the possibility of agglomeration and free surface is active for all times.

2.3.2. Carbon Based TMP Composites in OER Catalysis Studies

All these catalysts require small particle sizes to achieve a high specific surface area, enabling the creation of thin catalyst layers crucial for maintaining high performance in fuel cells and electrolyzers. Large catalyst particle sizes result in thick layers that hinder reactant mass transport and lead to high mass transport overpotentials. One common approach to reducing electrocatalyst particle size is by using a support material. Carbon is the most prevalent support material for electrochemical systems due to its affordability, high electrical conductivity, and relatively good stability under operating conditions. In a study investigating carbon-supported transition metal phosphides (TMPs) for OER catalysis, metals such as Mo, Cr, W, Ni, and Co were utilized. Ni_2P exhibited the best performance, comparable to commercial IrO2. The notable oxidation and reduction peaks are attributed to the surface oxidation of nickel to Ni^{3+} and its subsequent reduction. Co_2P and CrP-40 demonstrated moderate OER activity, with an onset potential close to 1.6 V vs RHE, while other metal phosphides did not exhibit significantly better performance than the support material[55].

The OER performances of TMP materials are summarized in Table 2 below. As one can see from the table, overpotential values at 10 mA/cm^2 current density generally

vary between 250 - 350 mV. The general character seen in the studies is that studies that effectively used the above-mentioned strategies achieved a higher OER catalyst performance[24,56,57]. To briefly summarize these strategies, it is to increase the number of active sites and increase the intrinsic activity of these active sites. However, caution should be exercised when interpreting OER activity values given in the literature. Because it has been shown that the given OER overpotential values vary depending on the substrate used, and a lower overpotential is measured in samples using nickel foam[58]. Additionally, it has been observed that the oxidation peak occurring before OER causes an extreme decrease in overpotential values, especially in samples containing high active material loading[59].

Table 2. OER activity comparison of the TMP materials.

Catalyst	Overpotential at 10 mA/cm^2 (mV)	Tafel Slope (mV/dec)	Electrolyte	Reference
$Ni_{12}P_5/Ni_3(PO_4)_2$	318	51.7	1 M KOH	[38]
Ni_2P	290	47	1 M KOH	[37]
$Ni_{12}P_5$	290	49.8	1 M KOH	[11]
Ni_5P_4	320	72.2	1 M KOH	[60]
Ni_5P_4-Ni_2P	300	64	1 M KOH	[36]
Ni-P on NF	309	58	1 M KOH	[61]
Cu_3P-Co_2P	334	132	1 M KOH	[62]
CoP-Co_2P	317	58.9	1 M KOH	[63]
Co–P/Cu	345	47	1 M KOH	[64]
Al–CoP/NF	330	69	1 M KOH	[65]
NiCoP/NF	280	87	1 M KOH	[66]
NiCoP/rGO	270	65.7	1 M KOH	[67]
CoFeP/NF	198	42	1 M KOH	[68]
Mn-CoP	288	77.2	1 M KOH	[69]

CHAPTER 3

EXPERIMENTAL PROCEDURE

3.1. Production of Activated Carbon (AC), Activated Carbon/Nickel Phosphide (AC/Ni-P) Composite and Activated Carbon/Bimetallic TMP Materials

As a first step of AC production, pine cone (Pinus Pinea) petals were cut and kept in ethyl acetate in order to remove pine resin. Then, preliminary crushing was conducted in automatic mortar. Crushed petals were ball milled at 200 rpm for 15 minutes to obtain pine cone powder. The powder was then impregnated by H_3PO_4, with impregnation ratios (the ratio of activating agent to biomass) of 1 and 4. The impregnated samples were kept at 110 °C overnight in drying oven. Then, the samples were heat treated under 1 l/min Ar flow at 500 °C with heating rate of 5 °C/min. Collected AC powder were crushed in agate mortar and washed 2 lt of distilled water. The samples after this step is designated as 1IR and 4IR, the numbers indicating the impregnation ratio.

After production of AC, secondary impregnation step was conducted. AC powder (about 1g) was immersed in 20 ml of aqueous solution of $NiNO_3.6H_2O$. The molarities of the solutions were arranged in such a way that Ni loadings (wt % of Ni in AC/Ni phosphide composite) were 1, 5 and 10. After the water was evaporated at 110 °C, the samples were heat treated at 800 °C under Ar-H_2 atmosphere, with the same treatment parameters in AC production step. The production steps and the corresponding microstructures of the active materials are schematically given in Figure 2. The collected composite powders were then crushed in agate mortar. The designation after this step was as follows: designation of AC-Ni loading. For example, the composite that consists of AC with 1 impregnation ratio, loaded with 5 wt% of Ni is designated by 1IR-5Ni. In order to understand the effect of activation

temperature on electrical conductivity, a control sample was produced, which was activated at 800 °C and designated as 1IR-8.

The AC/bimetallic TMP composite production procedure was based on secondary wet impregnation. This procedure is conducted with transition metal nitrates ($Ni(NO_3)_2.6H_2O$, $Co(NO_3)_2.6H_2O$, $Mn(NO_3)_2.6H_2O$, $Fe(NO_3)_3.9H_2O$), followed by secondary heat treatment at 800 °C under 1 lt/min flow of Ar-H_2 gas mixture. All heat treatments lasted for two hours, with 5 °C/min heating rate. The secondary treatment aimed to reduce the transition metal ions and produce bimetallic TMP, using surface phosphorus on AC. The mass loading of TMP on AC was based on 10 wt% transition metal for each sample. In all samples, 5 wt% Ni loading was kept constant, and the other 5 wt% was one of Co, Mn and Fe. Since the loading amount was the same and the second transition metal was different, the materials were designated accordingly. For example, bimetallic TMP using Ni and Co on 1IR AC is designated as 1IR-NiCoP.

Bare bimetallic phosphides were produced via thermal phosphidation method. $NiCl_2.6H_2O$ and $CoCl_2.6H_2O$ were used as the transition metal precursors. These powders were mixed and ground in an agate mortar. The mass of the powders were chosen according to the aimed molar ratio. Then, NaH_2PO_2 is added as a phosphiding agent. The mass of NaH_2PO_2 was two times the mass of the precursor powders combined. All the powders were ground together to form a seemingly homogeneous mixture. These mixtures were heat treated under Ar atmosphere at 300 °C. The flow rate of the Ar was 1 lt/min. Ni_2P was also produced by this method for comparison. The samples were named as $Ni_{0.25}Co_{0.75}P$, NiCoP, $Ni_{0.75}Co_{0.25}P$.

3.2. Chemical and Structural Characterization of Active Materials

Electrochemical performance determining chemical and structural properties of active materials were characterized by N_2 adsorption, SEM, XRD, DC electrical

conductivity, FTIR spectroscopy, ICP-OES and XPS. N_2 adsorption experiments were conducted at -196 °C in Autosorb-6. Prior to the measurements, the samples were degassed at 300 °C for 12 h, in order to remove adsorbed species at the surface of active materials. BET surface areas of the samples were computed using 0.01-0.1 relative pressure range. XRD analyses were conducted using X-ray diffractometer (XRD, Bruker D8 Advance) with CuKα radiation. MAUD software was utilized for Rietveld refinement, in order to compute weight fractions of the phases. FTIR spectroscopy was applied in ATR mode (Perkin Elmer Frontier) without any addition to active materials. XPS analyses were conducted in XPS, PHI 5000 VersaProbe. The binding energy regions of C, O, P and Ni elements were partially scanned.

SEM micrographs were taken 20 kV of accelerating voltage and 3.5 spot size (FESEM, Nova NanoSEM 430). Powders were adhered to carbon tape on aluminum holders for analysis. SEM micrographs were captured at various magnifications (500X, 1000X, 2000X, 8000X) to examine the particle morphology. An accelerating voltage of 20 kV and a spot size of 3.5 were used for imaging. Chemical composition analyses were conducted using Energy Dispersive Spectroscopy (EDS), with the accelerating voltage increased to 30 kV to raise the dead time. To avoid interference from the carbon tape, the electron beam was focused on larger particles at a high magnification (approximately 10000X). Given the challenges of EDS analysis for carbon due to its low atomic number, the spectra were used primarily for comparative purposes.

Obtained AC/TMP materials were ball milled at a frequency of 25 Hz for 10 minutes to produce smaller particles with a uniform size distribution, aiming to reduce contact resistance. Measurements were conducted on the powdered ACs without any additives. A specialized apparatus was designed for direct electrical conductivity measurements from powders. This setup included two brass plugs positioned with clips around the powder, which was contained within a PEEK cylinder. The height of the AC powder was maintained around 1 mm to ensure consistent force

application by the clips during conductivity measurements. After assembling this apparatus, the electrical conductivities of the ACs were measured using the Modulab MTS Solartron Analytical module, suitable for highly conductive materials. Conductivity measurements were performed using a DC current at a constant voltage of 5 mV for 10 minutes. Resistance was calculated from the average values of voltage and current according to Ohm's law.

3.3. Electrochemical Characterization

The electrochemical performances of the active materials were tested in two different configurations: rotating disc electrode (RDE) and standard three electrode setup. Cyclic voltammograms and OER characteristics were tested in RDE, whereas standard setup was utilized in galvanostatic charge-discharge cycles for capacitance determination. Electrode preparation steps for both systems are given as follows:
In order to prepare RDE electrode, firstly, 60 mg of active material was mixed with 8 ml of deionized water and 2 ml of isopropyl alcohol. Then, 200 µl of binder (5 wt% of nafion in isopropyl alcohol) was added to this mixture (LIQUionTM). The resulting ink was sonicated for 30 minutes. Lastly, 10 µl ink was dropped on glassy carbon RDE and dried. The electrode area was 0.196 cm^2.

Electrodes for standard three electrode setup were prepared via PTFE binder and carbon black conductive additive. The weight ratio of active material: PTFE: carbon black was 80:10:10. These materials with the given weight ratio were mixed and kneaded until a uniform dough was obtained. Then, it was pressed on Nickel foam and dried. Typical active material loading of an electrode was about 8 mg.

Three electrochemical tests were performed on the cells: cyclic voltammetry (CV), galvanostatic charge and discharge (GCD), and electrochemical impedance spectroscopy (EIS). CV was conducted at scan rates of 10, 30, and 50 mV/s and 100 mV/s between -0.5 V to 0.6 V vs. Hg/HgO, with the 10th cycle displayed in all

figures. GCD tests were carried out at the current density of 2 A/g up to 0.6 V, with the 10th charge-discharge curve shown in the figures and discharge curves used for capacitance calculations. EIS measurements were conducted over frequencies ranging from 200 kHz to 10 mHz, with a 10 mV sine wave applied.

OER activities of the active materials were tested with linear sweep voltammetry (LSV), chronopotentiometry (CP) and EIS. LSV was applied between the potentials of 0 V and 0.7 V vs. Hg/HgO, at the sweep rate of 5 mV/s. The potentials were converted to the reversible hydrogen electrode (RHE) according to the following formula:

$$E(RHE) = E(Hg/HgO) + E_0(Hg/HgO) + 0.0592pH$$

where E(RHE) is the RHE potential, E(Hg/HgO) is the potential measured with the Hg/HgO reference electrode, E_0(Hg/HgO) stands for the standard electrode potential for Hg/HgO. The electrolyte was 1 M KOH, and the pH of the electrolyte was taken as 14.

Chronopotentiometry tests were conducted at 10 mA/cm^2 current density. EIS were conducted at 0.7 V vs Hg/HgO, over frequencies ranging from 200 kHz to 10 mHz, with a 10 mV sine wave applied.
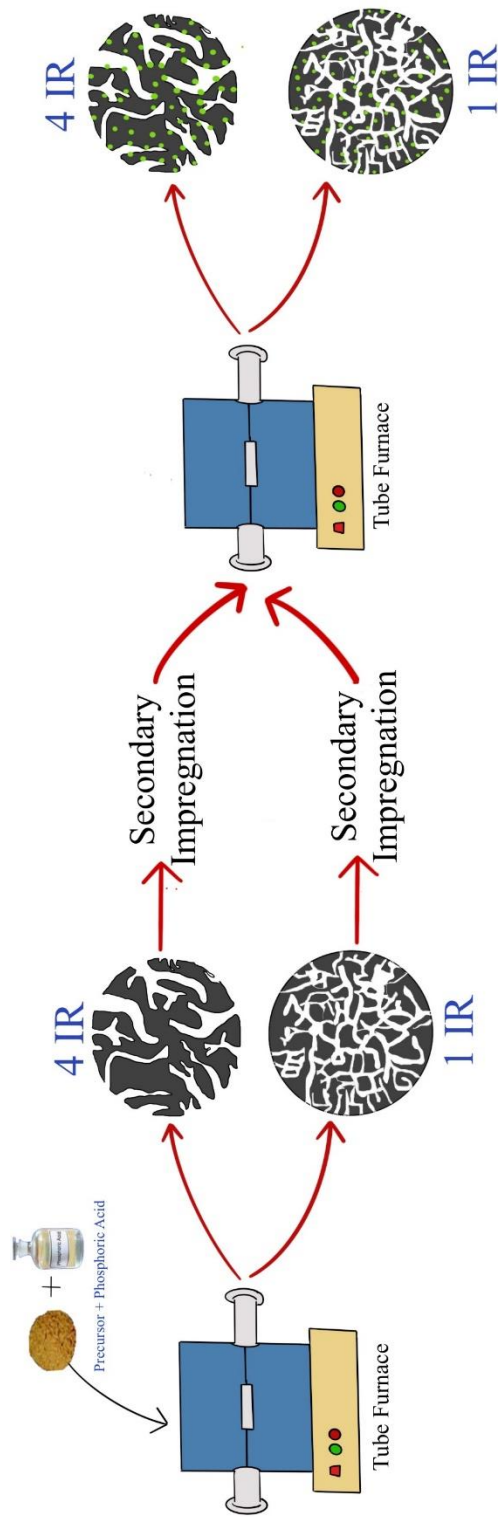
Figure 2. Schematic drawing of AC/TMP production method

CHAPTER 4

AC/NI PHOSPHIDE COMPOSITE PRODUCTION AND THEIR ELECTROCHEMICAL PERFORMANCE EVALUATION

Adsorption isotherms of the active materials are given in Figure 3. According to BDDT classification [70], 1IR AC and its composites show type I isotherm, indicating mainly microporosity (Figure 3. a). On the other hand, 4IR AC and its composites have micro and mesoporosity, as their behavior can be classified into type IV (Figure 3. b). These findings are similar to previous reports; as a result of enhancement in the impregnation ratio, share of mesoporosity in total porous structure increases [71,72]. Furthermore, BET surface areas of the composite samples are smaller than the bare AC samples (see Table 3). This effect is more pronounced as Ni loading increases for both 1 IR and 4 IR based composites; yet, BET surface areas of the composites do not decrease dramatically. This observation indicates that most of AC porosity is preserved even after Ni loading, open for EDL formation.
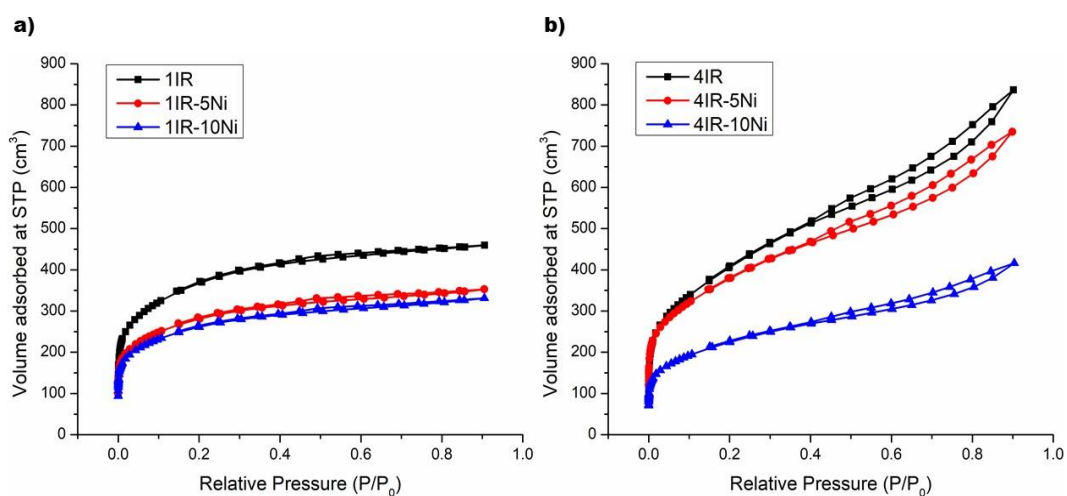
Figure 3. Adsorption isotherms of a) 1IR AC and b) 4IR AC based composites.

X-ray diffractograms of the active materials are given in Figure 4 and Figure 5. Firstly, there are two broad humps around 26° and 44° in the XRD pattern of 1IR AC. These humps were observed in the XRD patterns of AC, when the heat treatment temperature did not exceed 1000 °C and the carbonaceous structure was not graphitized [73]. The composite structures also have the humps, as well as the peaks corresponding to Ni phosphide phases. There are two Ni phosphide phases found; hexagonal Ni_2P and tetragonal $Ni_{12}P_5$ (ICSD numbers of the phases are 27162 and 27158, respectively). As Rietveld refinement results given in Table 4 suggest, Ni phosphide phase generated on the surface of AC is always nearly pure Ni_2P, except for the 1IR-10Ni sample. The reason of different phase formation in this sample can be attributed to P/Ni molar ratio [74]. Since smaller amount of H_3PO_4 was used in the activation step of 1IR AC, the amount of phosphorus groups to be utilized in Ni phosphide production is also smaller compared to 4 IR AC. Therefore, increasing Ni content from 5 wt % to 10 wt % resulted in the formation of high Ni containing $Ni_{12}P_5$ phase for 1IR AC based composites. However, this phase does not form in 4IR AC based composites, since the phosphorus amount is adequate to form Ni_2P even for 10 wt % Ni containing 4IR-10Ni sample.

Table 3. BET surface areas of the active materials.

Sample	S_{BET} (m^2/g)
1IR	1304
1IR-5Ni	1002
1IR-10Ni	935
4IR	1333
4IR-5Ni	1266
4IR-10Ni	760

Table 4. Rietveld analysis results of the active materials.

	Ni$_2$P			Ni$_{12}$P$_5$			
	a	c	at %	a	c	at %	Rwp
1IR-5Ni	5.882 ± 0.001	3.392 ± 0.002	100	-	-	0	3.67
1IR-10Ni	5.890 ± 0.004	3.393 ± 0.002	34.98	8.666 ± 0.004	5.0904 ± 0.003	65.0	3.37
4IR-5Ni	5.870 ± 0.002	3.389 ± 0.001	100	-	-	0	9.35
4IR-10Ni	5.862 ± 0.001	3.385 ± 0.001	100	-	-	0	8.31
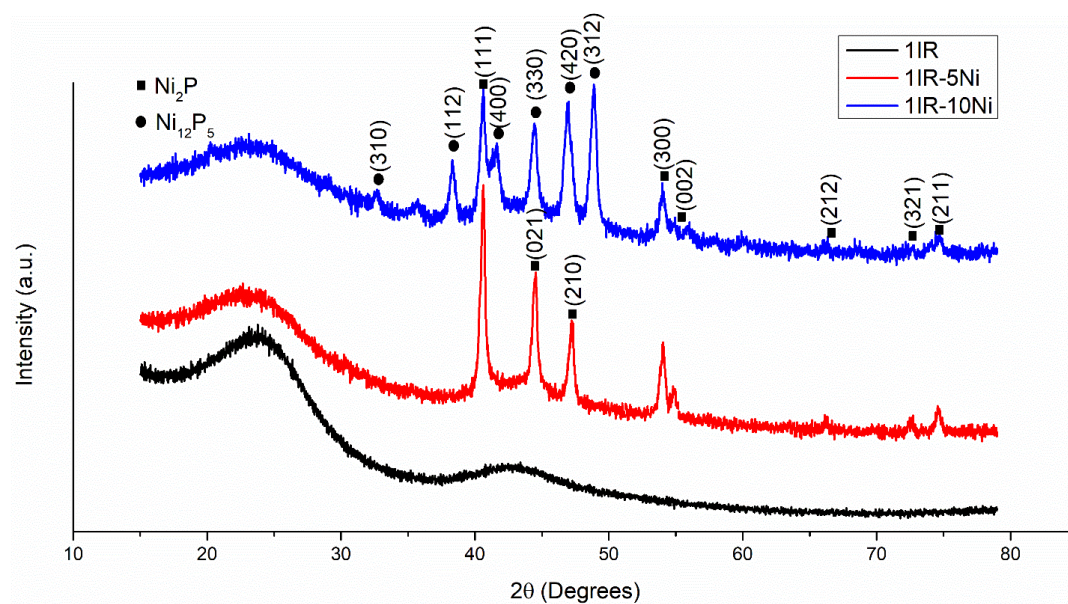
Figure 4. X-ray diffractograms of 1IR AC and its composites.
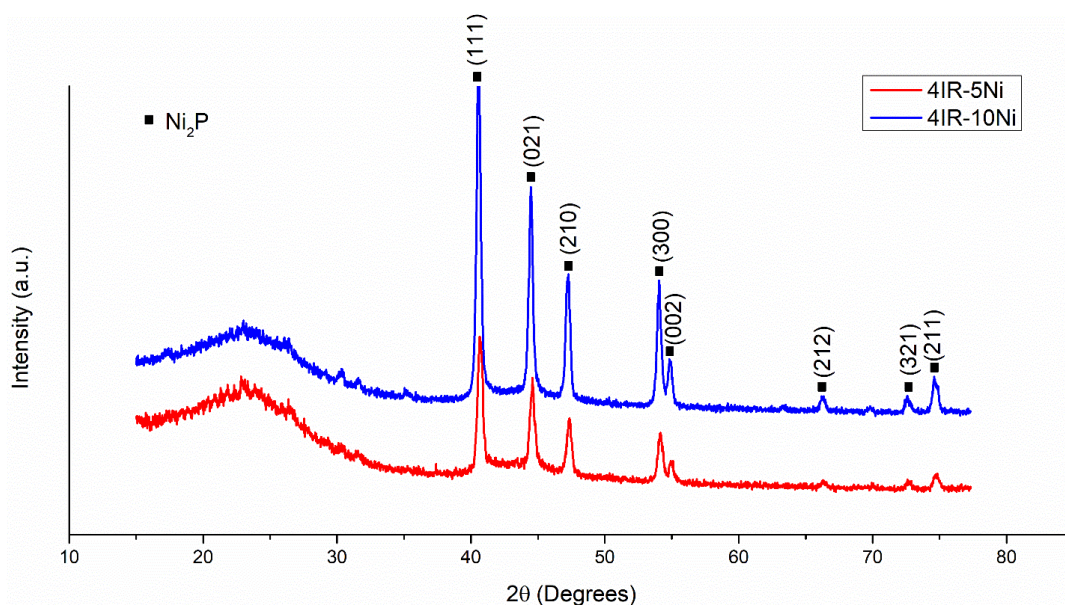
Figure 5. X-ray diffractograms of 4IR AC based composites.

SEM micrographs of AC and AC/Ni phosphides are given in Figure 6Figure 1 and Figure 7. In a, bare AC surface can be seen. In b and c, one can see spherical Ni_xP_y particles on AC surface. There is no obvious difference in the morphologies between Ni_2P and $Ni_{12}P_5$ phases. Moreover, the particle size distribution is not narrow; there are particles at both nano and micro regime. Comparing with the 4IR impregnated samples in Figure 7, 1IR impregnated samples have more number density of the phosphide phase. However, careful examination of the 4IR impregnated samples show that the phosphide phase grow interior of the particles. This could be attributed to porosity difference of the carbons. Mesoporosity present in the 4IR AC can act as a nucleation and growth site for the TMP phase, so that they grew interior of the AC particles. This results in the partial blockage of the mesoporosity of 4IR AC. Furthermore, hexagonal large particles are observed in 4IR-10Ni (see Figure 7(d)). This can be linked to both high amount of Ni loading and higher amount of phosphorus left on the surface result in the growth of Ni_2P particles to their equilibrium crystal shape. Although not in the hexagonal shape, large particles were also observed in 1IR-10Ni sample (see Figure 8).

32
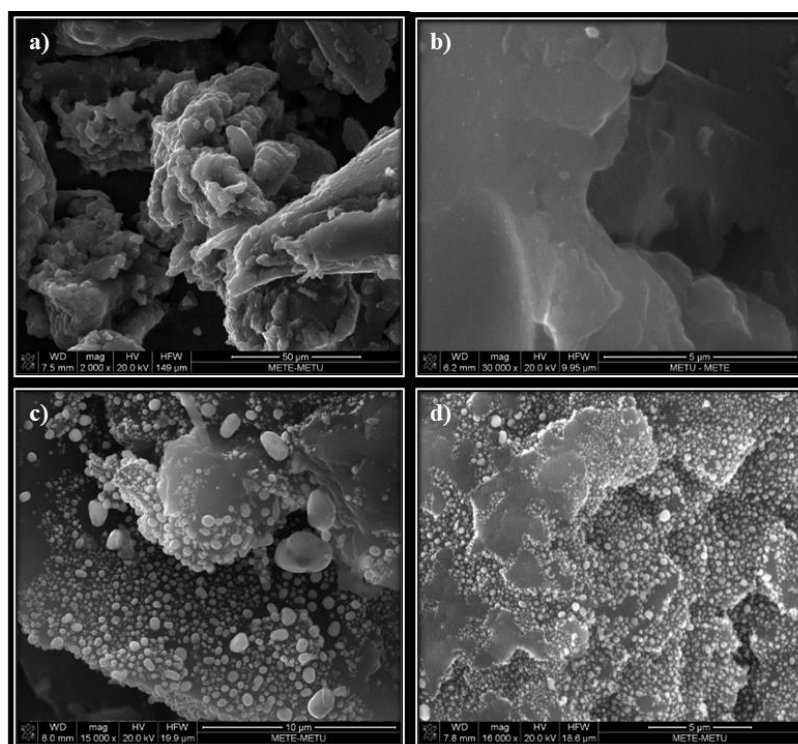
Figure 6. SEM micrographs of a) 1IR, b) 1IR-1Ni, c) 1IR-5Ni and d) 1IR-10Ni
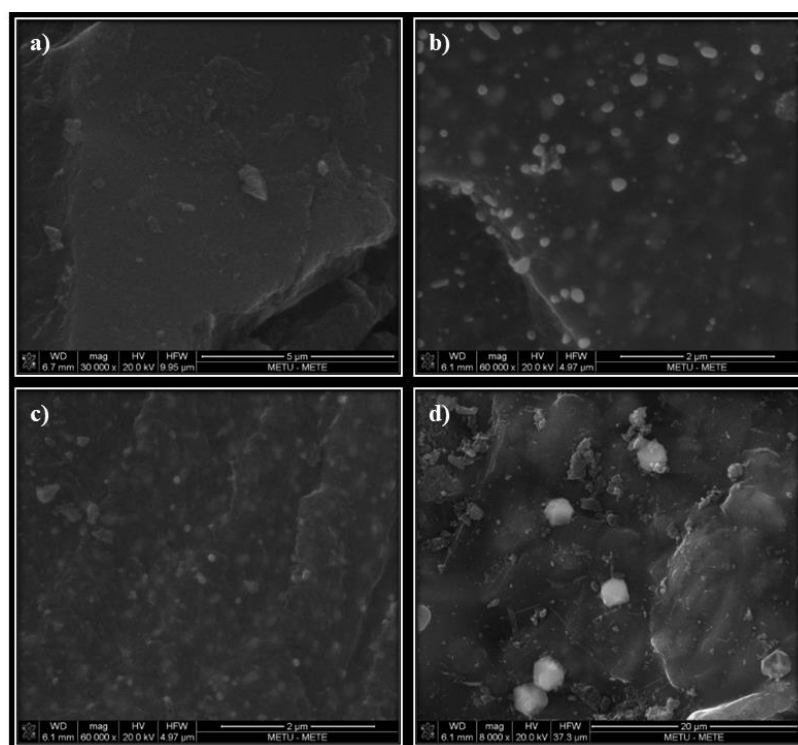
Figure 7. SEM micrographs of a) 4IR-1Ni, b) 4IR-5Ni, c) and d) 4IR-10Ni.
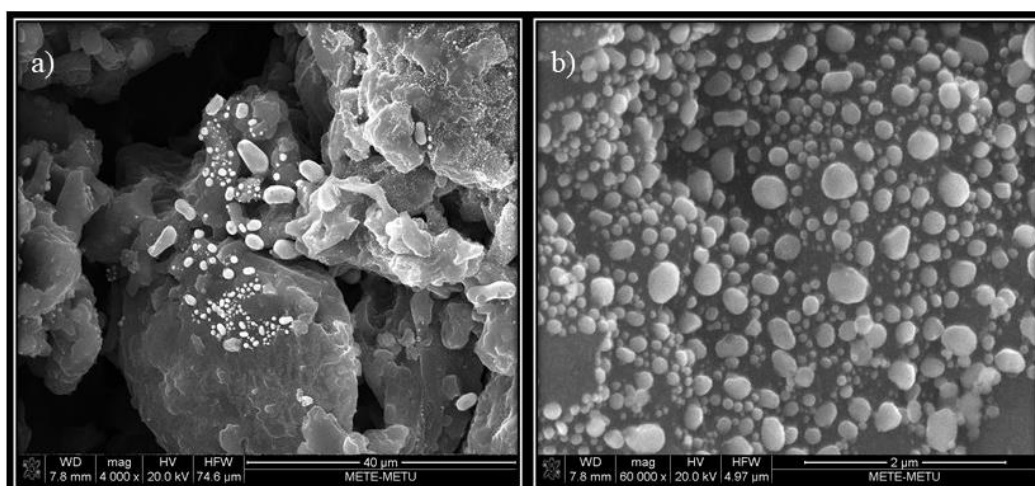
Figure 8. SEM micrographs of 1IR-10Ni sample at a) 4000x, b) 60000x magnification.

To assess the loading of transition metals (TMs) derived from biomass in TMP, Inductively Coupled Plasma Optical Emission Spectroscopy (ICP-OES) was employed on the active materials (seeTable 5). Firstly, significant amounts of Na, Ca, K, and Mg originating from biomass precursors were observed. These metals may positively influence the OER performance, as suggested by previous studies citing the improved performance of AC due to its higher ash and TM content. Moreover, even if the Fe content is infinitesimal (except 4IR-10Ni), addition of this transition metal was shown to be highly effective in OER catalysis[75]. The difference in the Fe content of the samples can be linked to the inhomogeneities originating from biomass precursor. Furthermore, values found in the ICP-OES can be considered as consistent with the impregnation loadings. This finding also supports that the precursor to product conversion efficiency is high in the process. Ni content is even higher than the impregnated value for the 4IR AC samples. This can be attributed to the higher concentration of phosphorus groups in 4IR AC likely enhances TMP production yield.

Table 5.ICP-OES results of AC/Ni phosphide materials.

	Ca wt%	Fe wt%	Mg wt%	Mn wt%	Na wt%	Ni wt%	K wt%
1IR-1Ni	0.26	0.02	0.07	0.01	0.88	**1.20**	0.03
1IR-5Ni	0.24	0.07	0.07	0.09	0.59	**4.36**	0.02
1IR-10Ni	0.20	0.02	0.08	0.01	0.86	**9.84**	0.03
4IR-1Ni	0.27	0.03	0.07	0.01	0.95	**1.48**	0.02
4IR-5Ni	0.27	0.03	0.07	0.01	0.96	**12.04**	0.04
4IR-10Ni	0.26	0.24	0.07	0.02	0.79	**14.26**	0.03

FTIR spectroscopy results of the active materials are given in Figure 9. There are a number of absorption bands associated with the surface functional groups on AC. The effect of Ni phosphide phases formed on the surface of AC for the composites is not taken into consideration for FTIR spectroscopy, since they do not show IR absorption bands [76]. The broad peak around 3400 cm^{-1} especially apparent in the spectrum of 1IR sample is linked to O-H stretching vibrations in hydroxyl groups. The small bands around 3000 and 2920 cm^{-1} correspond to C-H stretching vibrations in aliphatic chains. Note that these peaks do not appear in 1IR sample, but present in 1IR-5Ni, 1IR-10Ni and high temperature vacuum treated $ZnCl_2$ activated AC (see Supplementary). This is linked to the structural reorganization upon high temperature heat treatment in AC/Ni phosphide composites. The bands around 2300-2400 cm^{-1} can be ascribed to the vibrations in alkynes or ketenes [77,78]. Furthermore, there is a broad band from 2000-1650 cm^{-1}, having peaks around 1900 and 1750 cm^{-1}. These bands can be attributed to C-O stretching vibrations in carboxylic acids, lactones and aldehydes [79]. The band around 1580 cm^{-1} can be ascribed to C=C aromatic ring stretching vibrations and quinones [80]. Lastly, there is an overlapping band, occupying the interval from 1300 cm^{-1} to 900 cm^{-1}. One of the consitituents of these complex band peaks around 1200 cm^{-1}. This peak has contributions from both phosphate groups and C–O stretching vibrations in alcohols, phenols, acids, ethers [81]. This peak is intense in 1IR sample; however, it loses its intensity in 1IR-5Ni and 1IR-10Ni samples. This situation is linked to the disappearance of phosphate groups at high heat treatment temperature, and the remaining shallow peak is due to the C-

O bond. The peak around 1100 cm^{-1} has contributions from C-OH stretching vibrations and O-H bending. This peak is sharper in composite samples and high temperature vacuum treated AC. The peak around 1000 cm^{-1} in 1IR sample is ascribed to C-O-P linkage, P-O stretching in P=OOH, P-O-P stretching in polyphosphates. Considering the disappearance of this band in 1IR-5Ni and 1IR-10Ni, one can argue that the phosphorus groups are greatly reduced in number in composite production step.
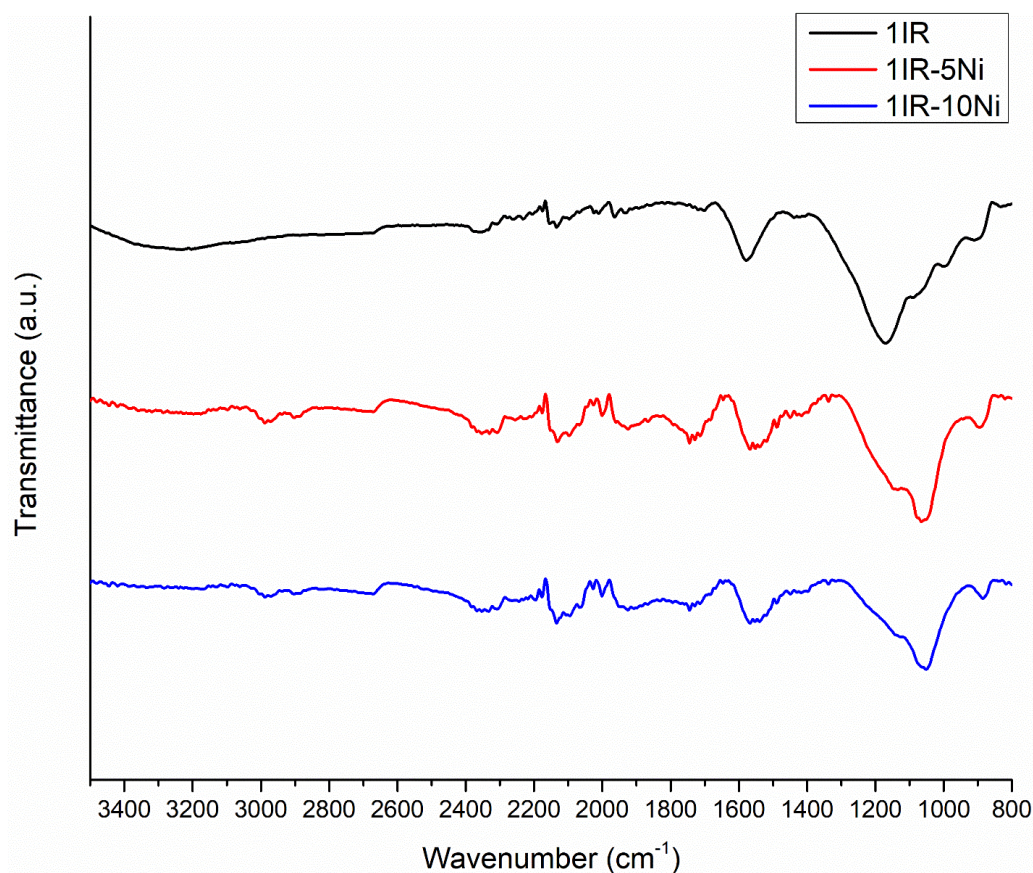
Figure 9. FTIR spectra of 1IR AC, 1IR-5Ni and 1IR-10Ni.

The surface chemistry of AC and AC/Ni phosphide composites further evaluated by XPS. C 1s, O 1s, P 2p and Ni 2p excitation signals were deconvoluted and the results from 1IR-10Ni sample are given in Figure 10, and the peaks' positions and relative integrated areas are given in Table 6 and Table 7. Firstly, C 1s peak is deconvoluted into four peaks. The matchup of these peaks with the surface groups on AC is as

follows: the first peak (peak A, red) arises from graphitic structure in carbon; the second peak (peak B, green) is attributed to aliphatic carbon chains; the third peak results from carbon excitations in alcohol (R-OH), ether (R-O-R) or C-O-P groups; the fourth peak (peak C, blue) is linked to carbonyl, carboxyl and ester groups and π-π* transitions in aromatic rings [51,53]. O 1s peaks are deconvoluted into two peaks. Peak A is assigned to double bonded oxygen to carbon or phosphorus (C=O or P=O). Peak B is linked to single bonded oxygen such as C-O and C-O-P [82]. P 2p peaks are composed of two peaks, which correspond to phosphorus in Ni phosphide species (peak A) and phosphates (peak B) [83]. Note that peak A in P 2p excitation does not appear in the spectra of 1IR and 4IR samples since they do not have Ni phosphide species.

Electrical conductivity measurements are also given in Table 8. The values are dependent on the applied pressure; therefore, they are used only for comparison purposes. As expected, conductivity of 1IR is smaller than the others. The reason is two fold: one is associated with electronic energy band of carbons are given as a function of heat treatment temperature. The reduction of band gap, and consequently increase in conductivity is associated with delocalized electrons of π bonds, which reside in sp^2 clusters of aromatic rings. The other is surface functional groups decrease the electrical conductivity, since they are obstacles for electron movement. This is especially well studied in oxygen functional groups; however, there is no detailed work analyzing effect of phosphorus groups on electrical conductivity of AC as to the best of our knowledge. Yet, it is reasonable to suggest part of the resistive behavior of 1IR comes from phosphorus functional groups.
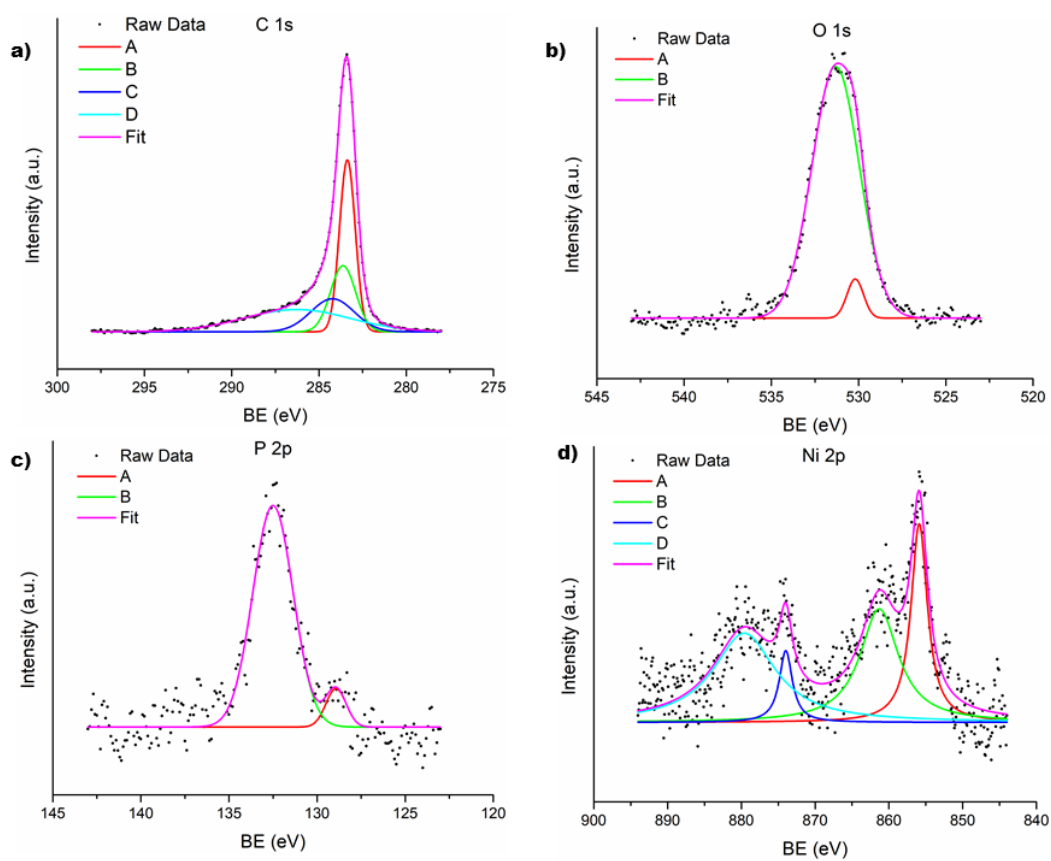
Figure 10. XPS spectra of 1IR-10Ni sample: (a) C 1s, (b) O 1s, (c) P 2p, (d) Ni 2p

Table 6. Peak positions and integrated areas of C 1s excitation in active materials.

	C 1s							
	A		B		C		D	
	Position (eV)	Int. Area (%)	Position (eV)	Int. Area (%)	Position (eV)	Int. Area (%)	Position (eV)	Int. Area (%)
1IR	283.2	46.0	283.7	22.0	284.8	29.7	289.5	2.3
1IR-10Ni	283.4	33.1	283.6	20.3	284.2	17.5	286.3	29.0
4IR	283.5	48.0	284.1	20.4	285.3	28.9	289.9	2.7
4IR-5Ni	283.8	18.0	284	32.0	284.5	25.6	286.6	24.5
4IR-10Ni	283.9	21.7	284	28.6	284.6	20.7	286.7	29.0

Table 7. Peak positions and integral areas of O 1s and P 2p excitations in active materials.

	O 1s				P 2p			
	A		B		A		B	
	Position (eV)	Int. Area (%)	Position (eV)	Int. Area (%)	Position (eV)	Int. Area (%)	Position (eV)	Int. Area (%)
1IR	529.3	13.9	531.4	86.1	-	-	132.3	100.0
1IR-10Ni	530.2	5.2	531.3	94.8	128.9	7.9	132.5	92.1
4IR	529.7	6.4	532	93.6	-	-	133.5	100.0
4IR-5Ni	530.1	15.6	532.1	84.4	129.4	1.8	132.7	98.2
4IR-10Ni	530.2	14.3	532.4	85.7	129.8	5.5	133	94.5

Table 8. DC electrical conductivities of AC and AC/Ni phosphide composites.

Sample	Conductivity (S/cm)
1IR	3.6E-06
1IR-8	8.9E-05
1IR-5Ni	1.3E-04
1IR-10Ni	2.2E-04

The electrochemical behavior of the developed active materials can be evaluated as two distinct regions in cyclic voltammograms (Figure 11 and Figure 12). In -0.5V – 0.3 V region, AC and electrical double layer formation is dominant, while in 0.3V – 0.6 V region, redox reactions on Ni phosphide phase is determinant. Although the first region is dominant with capacitive current, there may be other contributions to the current depending on the potential. TMP phases were shown to have ORR catalytic activity[84], which has onset potentials between 0 V - 0.2 V vs. Hg/HgO. Indeed, AC/TMP materials produced in this study demonstrated a similar activity (see Figure S5). Therefore, the behavior on the negative potential region should not only be attributed to the capacitance of the active materials.

It is observed that Nickel loading is dominant in the second region. In this region, there are oxidation and reduction reactions of Ni^{2+}/Ni^{3+} redox couple. From cyclic voltammograms of 4IR-1Ni and 1IR-1Ni samples, it implies that 1 wt% Ni loading is not effective for capacitive contribution. Comparing the CV curves of 1IR-5Ni and 4IR-5Ni, the redox peak intensity and consequently the charge storage behavior is close, as a result of the same amount of Ni loading. However, 1IR based one has slightly sharper peaks, which can be linked to higher number density of Ni phosphide at surface. The sharpest peaks and biggest contribution come from 4IR-10Ni. This can be expected as a result of high Ni loading; however, its EDL contribution and rate capability is better than 4IR based composites. This can be attributed to the blockage effect of surface phosphorus groups is more dominant than that of Ni phosphide phase.

When the CVs of 1IR AC based samples are examined, it is observed that the OER tendency of the 1IR-1Ni sample is very high, but it does not show the same high performance in faradaic charge storage. The reason for this can be attributed to the small amount of Ni_2P phase in the 1IR-1Ni sample, but they are in the nano regime. While nanosized particles increased the OER activity thanks to their high active surface area, the capacitive effect is not as significant due to the insufficient amount of Ni_2P phase. Additionally, the performance difference between 1IR-5Ni and 1IR-10Ni samples is attributed to the difference between the nickel phosphide phases. The ΔE_p value of the 1IR-10Ni sample, which is approximately 65 at% $Ni_{12}P_5$, is significantly lower than the 1IR-5Ni sample. This can be explained by the fact that the $Ni_{12}P_5$ phase, which contains a higher amount of Ni, has better conductivity than Ni_2P[85]. Besides, the 1IR-5Ni sample has more capacitance even though it contains less amount of Ni phosphide. Although there can be a redox mechanism difference between these two phases resulting in this behavior, it was not explained clearly in the previous studies. In this regard, the particle growth in the Ni phosphide phase in the 1IR-10Ni sample may have played a role in reducing the active surface area and thus, having smaller capacitance.
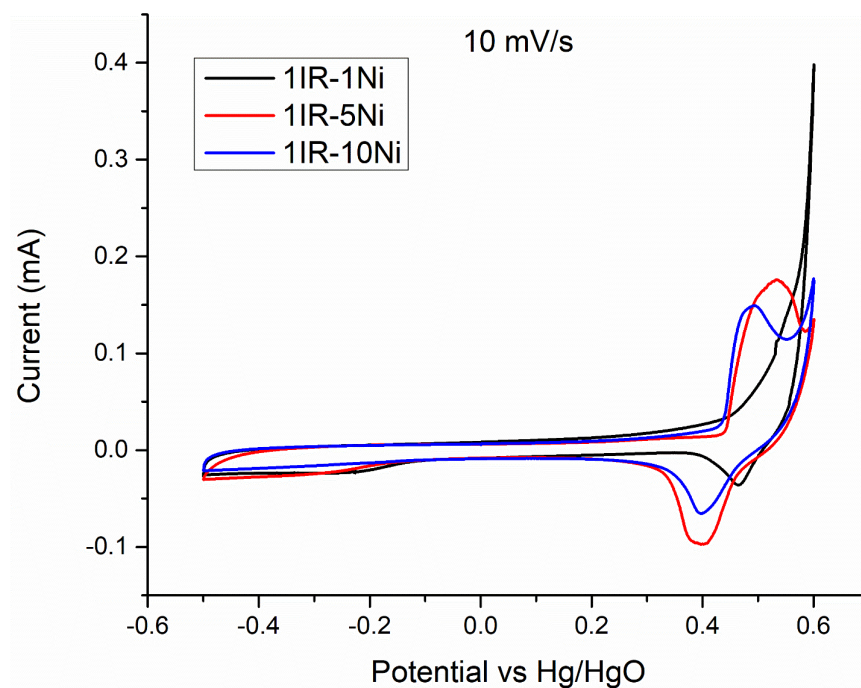
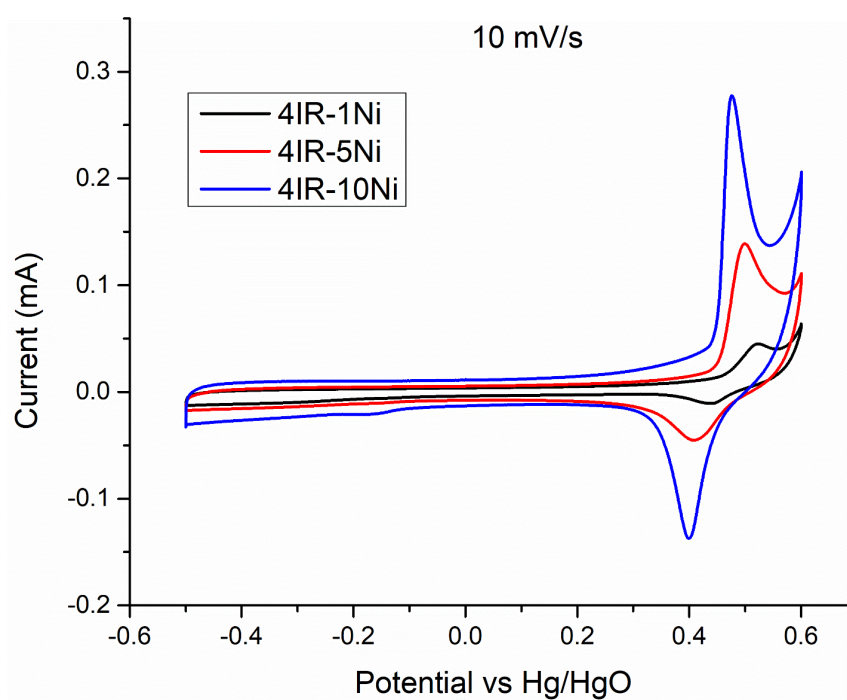Figure 11. Cyclic voltammograms of 1IR AC and its composites at 10 mV/s at RDE.

Figure 12. Cyclic voltammograms of 4IR AC and its composites at 10 mV/s at RDE.

Cyclic voltammograms also reveal the peak position shifts correlated to Ni loading amounts. The oxidation and reduction peak potentials, and the potential difference between them (ΔEp) are given in Table 9. It is apparent in this table that both the oxidation and reduction peaks shift to lower potentials as Ni loading enhances. This can be attributed to diffusion limitation of OH$^-$ ions, which are responsible for the redox reactions is these systems, in the composites with excess phosphate at the surface. Furthermore, the potential difference between oxidation and reduction peaks shows smaller values for 4IR AC based composites, suggesting comparably closer character to reversible kinetics. Among them, 4IR-10Ni has smallest ΔEp value.

Galvanostatic discharge curves of the AC/Ni phosphide composites are given in Figure 10. In these curves, the behavior observed in the cyclic voltammograms are validated; as a matter of fact, two distinct regions show the characteristics of faradaic charge storage and EDL capacitance. The former is responsible for the plateau around 0.4 – 0.35 V; whereas, the latter leads to linear potential-time dependence below 0.3 V. As expected, heavily Ni loaded samples such as 1IR-10Ni and 4IR-10Ni have wider plateau, indicating more faradaic charge storage from the reduction in Ni^{2+}/Ni^{3+} redox couple. Furthermore, nearly the same slope in the linear region proposed that EDL capacitance on the surface of AC is similar in all samples.

Table 9. Peak positions of the active materials in cyclic voltammograms.

	Oxidation Peak (V)	Reduction Peak (V)	ΔEp (mV)
1IR-1Ni	0.553	0.464	89
1IR-5Ni	0.529	0.412	117
1IR-10Ni	0.491	0.397	94
4IR-1Ni	0.525	0.442	83
4IR-5Ni	0.499	0.411	88
4IR-10Ni	0.475	0.402	73
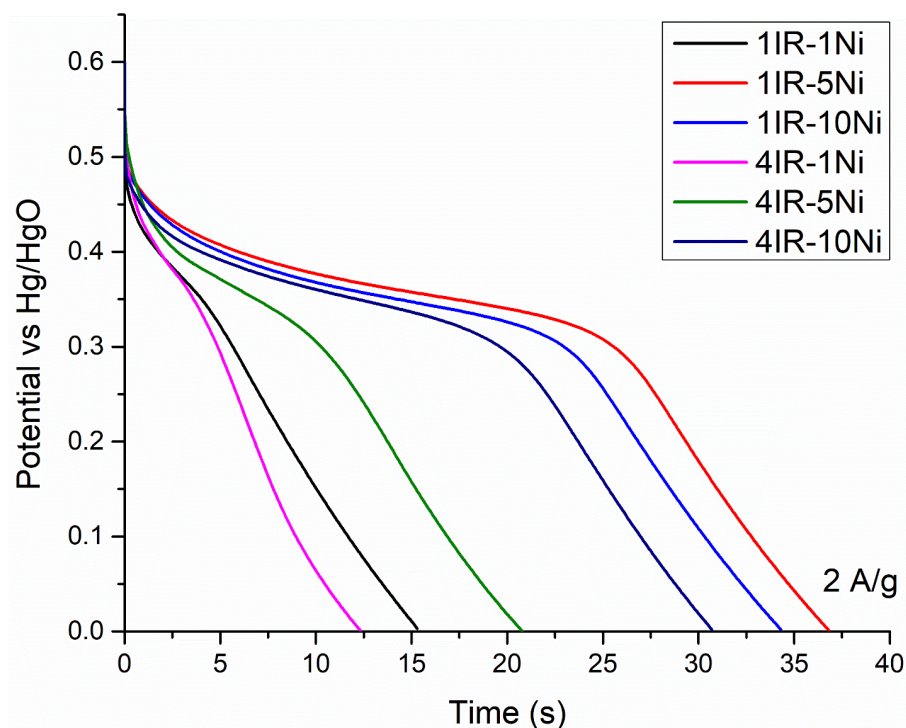
Figure 13. Galvanostatic discharge curves of the active materials.

The change in the specific capacitance for 500 cycles is given in Figure 14. Specifically in higher Ni loaded samples (1IR-5Ni, 1IR-10Ni and 4IR-10Ni), there is an enhancement observed in the capacitance values. This behavior was reported in several studies, however, the route of the observation is controversial. In the study of Zhou [1], the reason of the capacitance increase was attributed to the enabling effect of repetition of charging and discharging to ion movement. It is also reported that Ni phosphide species have gradual phase transition to oxides upon cycling. The possible explanation can be about a core shell structure with phosphorus involves in it. With this enhancement, the highest specific capacitance is achieved in 25th cycle of 1IR-10Ni sample. However, capacitance retention of 4IR-10Ni sample is better. Furthermore, the increase in the capacitance values are not observed for 1IR-1Ni, 4IR-1Ni and 4IR-5Ni samples. The reason of the lack of capacitance enhancement can be linked to the insufficient amount of Ni phosphide for 1IR-1Ni and 4IR-1Ni

samples; whereas, it can be attributed to ineffective utilization of Ni phosphide phase due to porosity blockage for 4IR-5Ni sample.
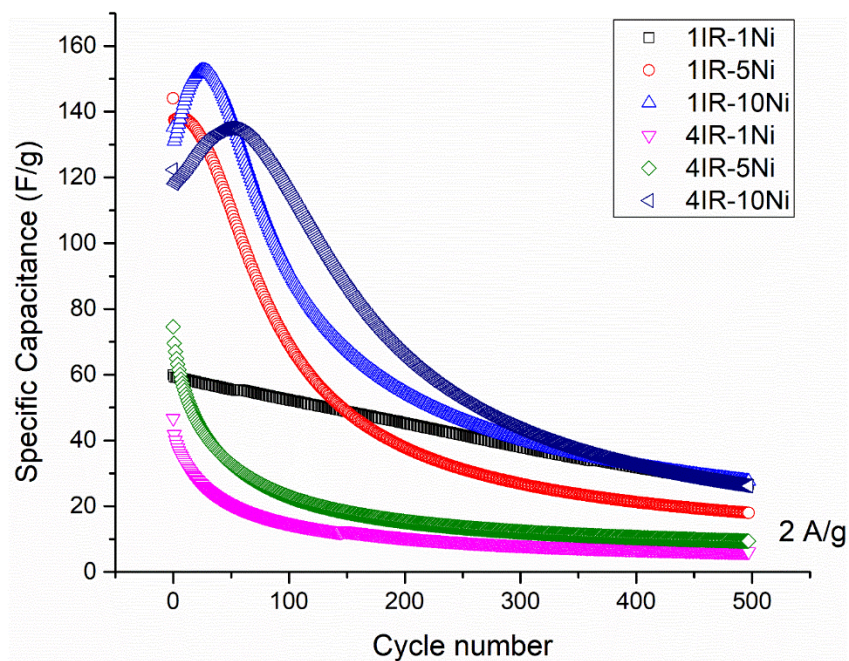
Figure 14. Specific capacitance as a function of cycle number.

Electrochemical impedance spectroscopy results are given in Nyquist plots in Figure 15 and Figure 16. The spectra obtained at 0 V reflects typical EC behavior; they all have a semicircle at the high frequency region and nearly vertical straight-line characteristics of double layer capacitance. The spectra obtained at 0.5 V vs. Hg/HgO demonstrates two deppressed semicircles. The high frequency semicircle is linked to the double layer capacitance; whereas, low frequency region demonstrates the redox reactions taking place on Ni phosphides.
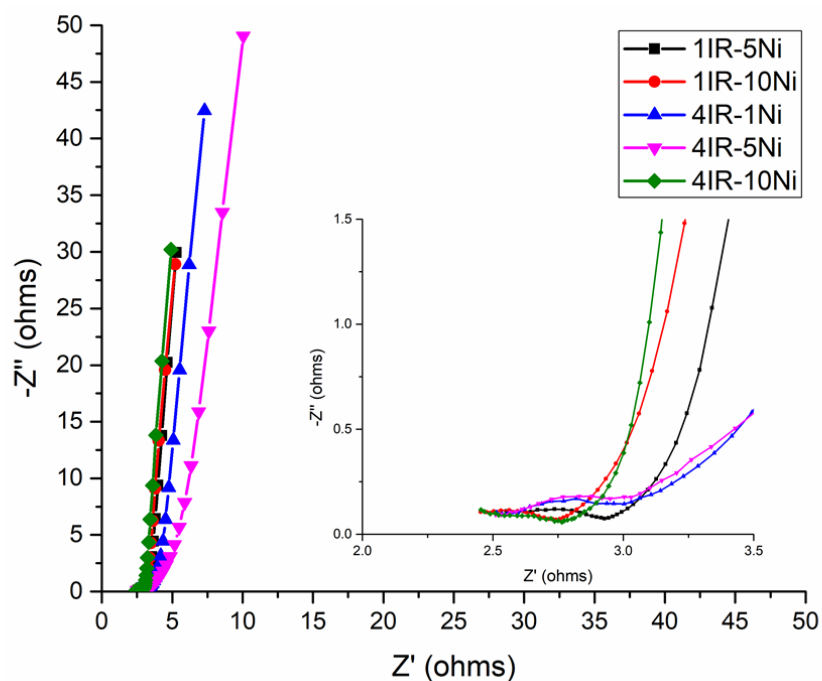
Figure 15. Nyquist plots of the active materials, spectra obtained at 0 V vs. Hg/HgO.

The results of equivalent circuit modelling of EIS spectra are given in Table 10 . In this model (see Figure 17), R1 is attributed to the electrolyte resistance, R2 is linked to the resistance originating from capacitive charge storage in porous electrodes, Q2 stands for the constant phase element and M2 is ascribed to restricted diffusion. R1 gives the solution resistance for both models, giving the values from 2.1 ohms to 2.4 ohms. Constant phase element is used in the model to account for the divergence from the pure capacitive response, as evident from the depressed semicircles in the high frequency region. It was obseved that the R2 values given in Table 10 did not change much for different samples. From this observation, it can be concluded that the resistance associated with capacitance in the produced samples does not show large changes. A difference could be expected between 1IR AC-based samples, where microporosity was dominant, and 4IR AC-based samples, where microporosity was combined with mesoporosity, but this effect is not dominant. The

45

more significant difference can be seen in the Rd2 values, which symbolize the resistance caused by restricted diffusion. One can argue that in 4IR AC-based samples, the porosity is filled by the Ni phosphide phase, creating an obstacle for diffusion, and for this reason, the Rd2 value in 4IR-1Ni and 4IR-5Ni samples was found to be higher than other samples. The fact that a similar effect is not observed in the 4IR-10Ni sample can be attributed to most of the Ni phosphide phase does not fill the porosity due to precipitation in chunky hexagonal morphology on the surface. A similar conclusion can be made by examining diffusion time (Td2) values. These high calculated values for 4IR-1Ni and 4IR-5Ni indicate longer effective diffusion distance for these samples.
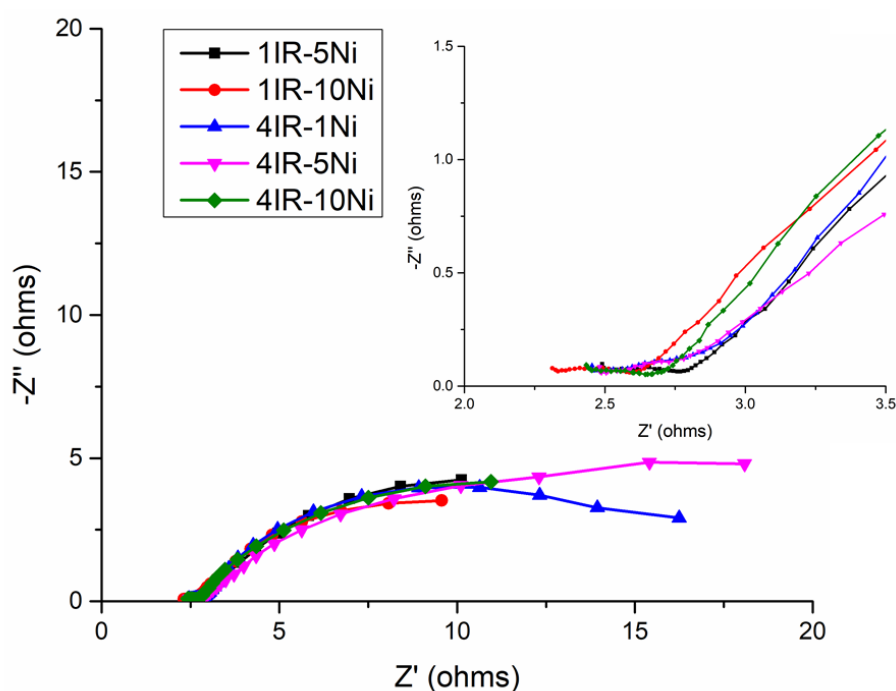
Figure 16. Nyquist plots of the active materials, spectra obtained at 0.5 V vs. Hg/HgO.
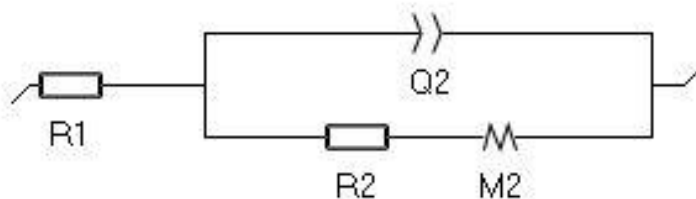
Figure 17. Equivalent circuit model utilized for the EIS spectra of the samples at 0 V vs Hg/HgO

Table 10. Results of EIS equivalent circuit modelling at 0 V

	1IR-5Ni	1IR-10Ni	4IR-1Ni	4IR-5Ni	4IR-10Ni
R1 (Ohm)	2.396	2.202	2.375	2.448	2.268
Q2 (F.s(a-1))	0.0153	0.0155	0.0150	0.0201	0.0121
a2	0.461	0.445	0.479	0.501	0.443
R2 (ohm)	0.529	0.528	0.613	0.548	0.493
Rd2 (ohm)	1.375	1.444	3.175	6.469	1.047
Td2 (s)	0.667	0.724	1.047	1.678	0.519

Utilization of AC/Ni phosphide active materials as OER catalyst are given below. Linear sweep voltammograms in Figure 18. Linear sweep voltammograms of the active materials. reflects that the OER has started when potential increases to 0.6 V vs Hg/HgO and up. In the evaluation of LSV, one can argue that 4IR-1Ni and 4IR-5Ni do not show good catalyst characteristics since they do not reach high current values at moderate potentials compared to 1IR AC based composites. On the other

hand, 1IR-1Ni, 1IR-10Ni and 4IR-10Ni seem to reflect good catalyst characteristics, reaching 10 mA/cm^2 current densities about 0.65 V vs Hg/HgO. This situation can also be seen in initial overpotential values in Table 11. However, examination of overpotential values at 3 hours after at 10 mA/cm^2 ascertains that even the samples with high initial overpotential values have considerable potential for OER catalysis. Moreover, stability curves given in Figure 16 account for the discrepancy between initial and 3 h overpotentials; all samples have activation especially at the first 2 hours of the test. The activation step in 4IR AC based samples have a gradual decrease as Ni loading increases; 4IR-1Ni has huge activation step in the first three hours whereas 4IR-10Ni shows only small increase in activity. The reason of activation is generally thought to be about phase transition and surface oxidation of Ni phosphide species. This can be also the case in this study; however, there should be another explanation in especially 4IR AC based catalysts considering its small Ni amount and huge activation step. The reason of this improvement can be ascribed to intensive phosphate groups in 4IR AC, partially withdrawn from the surface as catalysis process proceeds. Furthermore, the longer lasting samples (1IR-1Ni, 4IR-1Ni, 1IR-10Ni) reflect secondary activation after 15h. The reason of the activation can be attributed to phase transition on Ni phosphide species.
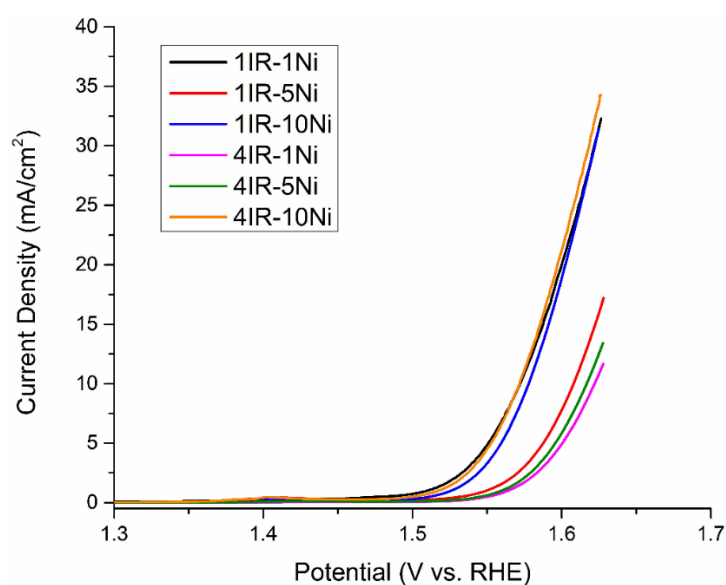
Figure 18. Linear sweep voltammograms of the active materials.

Table 11. Initial and 3 h overpotentials at 10 mA/cm^2.

	Overpotential at 10 mA/cm^2 (mV) (Initial)	Overpotential at 10 mA/cm^2 (mV) (3 h)
1IR-1Ni	347	345
1IR-5Ni	363	348
1IR-10Ni	359	342
4IR-1Ni	403	359
4IR-5Ni	368	352
4IR-10Ni	344	342
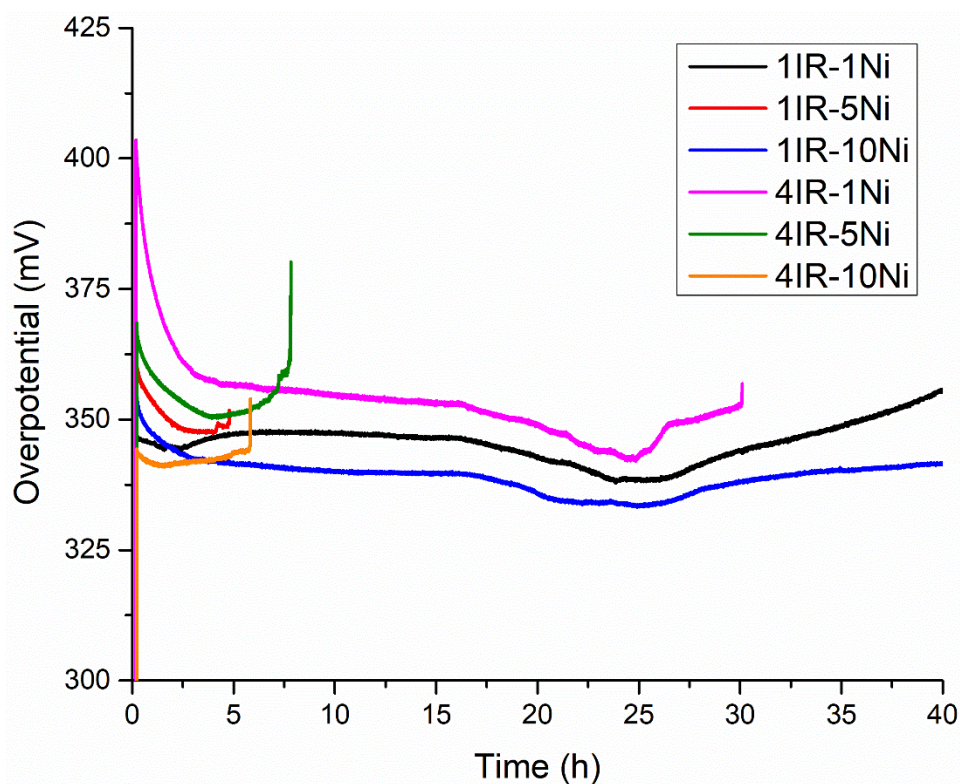
Figure 19. Stability test curves of the samples at 10 mA/cm^2

EIS results of the catalysts taken at 0.7 V vs Hg/HgO is given in Figure 20. The spectra show depressed semi-circles, which is characteristics of OER catalysis. In

the visual evaluation of the spectra, one can correlate the diameter of the depressed semi-circle with the overall resistance of the catalysis process. Indeed, comparison of initial overpotential values with the semi-circle diameters monitors this relationship; the one with the higher diameter have the largest initial overpotential. Furthermore, equivalent circuit modelling (inset of Figure 20) is conducted on the samples and the results are given in Table 12. In this model, R1 stands for solution resistance, R2 comes from the resistance of the catalysis reaction, R3 is related with the intrinsic resistivity of the active material. R3 results given in the Table 12 reveals that contribution of intrinsic resistivity of to the overall impedance is relatively small. Moreover, R3 values do not scatter in a great extent, which is consistent with DC electrical conductivity results given in

.
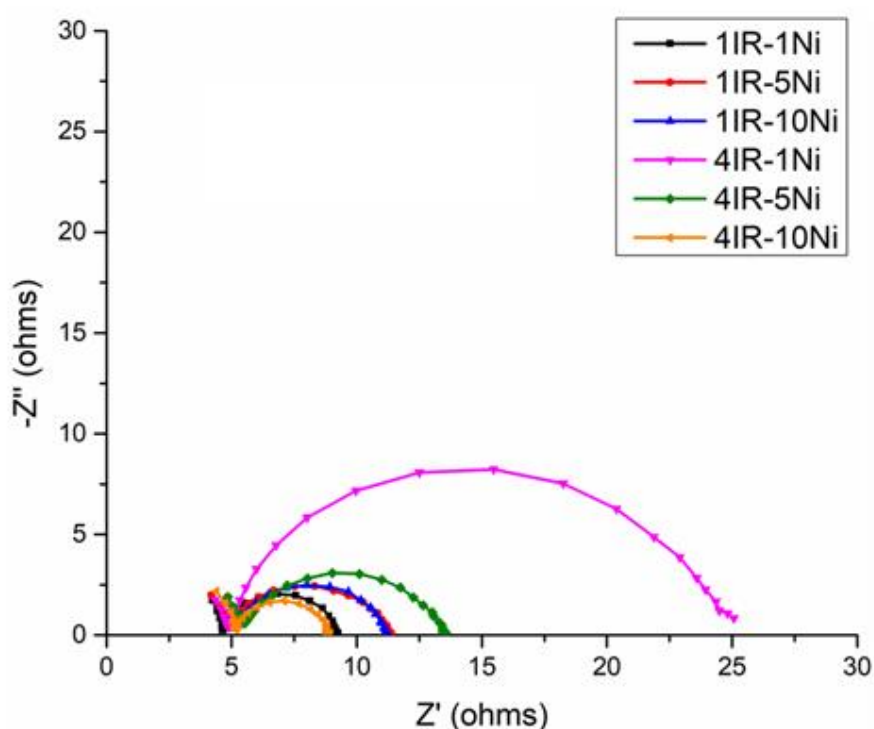
Figure 20. EIS results taken at 0.7 V vs Hg/HgO

50

Table 12. Equivalent circuit modelling results of EIS at 0.7 V vs Hg/HgO

	1IR-1Ni	1IR-5Ni	1IR-10Ni	4IR-1Ni	4IR-5Ni	4IR-10Ni
R1 (ohm)	4.343	4.543	4.759	4.409	4.981	4.772
R2 (ohm)	4.683	6.137	6.012	18.87	7.765	4.005
C1 (F)	0.032	0.012	0.025	0.028	0.010	0.052
R3 (ohm)	0.482	0.623	0.594	0.775	0.924	0.513
C2 (F)	0.122 e-3	47.59e-6	89.82e-6	54.81e-6	33.3e-6	0.123 e-3

CONCLUSIONS

In the first part of the study, AC/TMP composite is produced to be used in EC and OER catalyst applications. Firstly, AC is produced with phosphoric acid activation method. The surface of the phosphoric acid activated carbons is rich in phosphorus, and this affects the properties of the AC. TMP's on the other hand, are promising materials for EC usage, and there are numerous studies based on the TMP in EC. These studies include both bare and composite structures. Composite structures are generally beneficial for EC performance, if the production characteristics are carefully designed.

Two types of AC were produced with distinct impregnation ratios: 1IR and 4IR. N_2 adsorption experiments indicate that 1IR AC-based samples possess mainly microporosity, whereas 4IR AC-based ones exhibit both micro and mesoporosity. XRD analysis reveals the formation of TMP with a hexagonal Ni_2P and $Ni_{12}P_5$ crystal structure across all samples. SEM observations illustrate the influence of transition metal and AC impregnation ratio on the morphologies of the TMP phases.

XPS analysis primarily characterizes the valence states of secondary transition metals, unveiling the surface chemical state of the composites, which impacts both EC and OER catalysis.

CHAPTER 5

AC/BIMETALLIC TMP COMPOSITE PRODUCTION AND THEIR ELECTROCHEMICAL PERFORMANCE EVALUATION

The results of the N_2 adsorption experiment at 77 K are given as adsorption isotherms in Figure 21 and as BET surface area values in Table 13. The adsorption isotherms demonstrate that the origin of the different adsorption behavior stems from the impregnation ratio of AC. 1IR-NiFeP, 1IR-NiMnP, and 1IR-NiCoP samples have isotherms classified as type I, whereas 4IR-NiCoP has type IV isotherm according to BDDT classification. This situation also has implications for the porous structure of the composites. Indeed, 1IR based ones with type I isotherms are mainly microporous adsorbents, while 4IR based one with type IV isotherm contains both meso and microporosity. The change in porous structure with an increasing impregnation ratio is consistent with the previous results reported in the literature [86,87]. Moreover, around 1000 m^2/g surface area is obtained in 1IR based composites, and it is even higher in 4IR-NiCoP. Since the central portion of porosity is expected to originate in AC, it is normal to have a slight decrease in surface area as a result of porosity blockage after the composite structure is developed. Nonetheless, the reduction in surface area is not detrimental, leaving enough space for electrical double layer formation and OER active sites. Particularly 4IR-NiCoP sample shows promising textural characteristics due to its high surface area and mesoporosity for ion transportation.
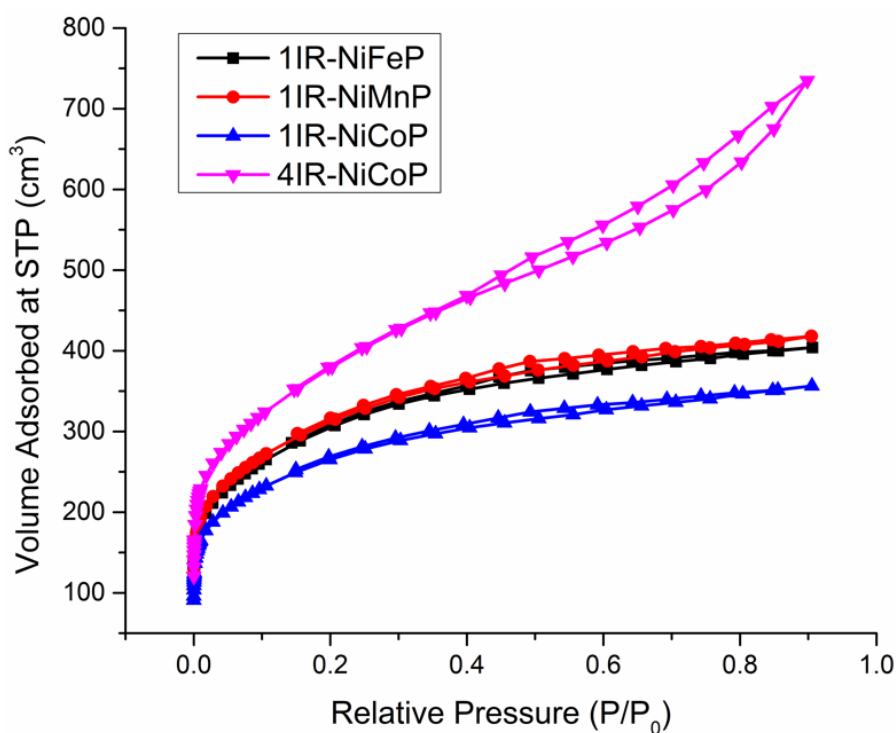
Figure 21. Adsorption isotherms of the AC/Bimetallic TMP composites.

Table 13. BET surface area values of the AC/Bimetallic TMP composites.

Sample	S_{BET} (m^2/g)
1IR-NiFeP	1064
1IR-NiMnP	1083
1IR-NiCoP	939
4IR-NiCoP	1266

XRD results of the active materials are given in Figure 22. Firstly, there is a hump around 38-48° in all composite samples, ascribed to AC in the structure [88]. In addition, this hump is more explicit in 1IR AC-based ones, whereas it is not pronounced in 4IR-NiCoP. This observation is linked to a more significant amount of bimetallic TMP formation on the surface of AC due to greater phosphorus content

in 4IR AC. Furthermore, the peaks at the diffractograms reflect the Ni_2P phase (hexagonal, P-62m); however, the peaks shift slightly as the bimetallic structure affects the lattice parameters. As a result, bimetallic TMP production was successful in all samples, based on XRD patterns.
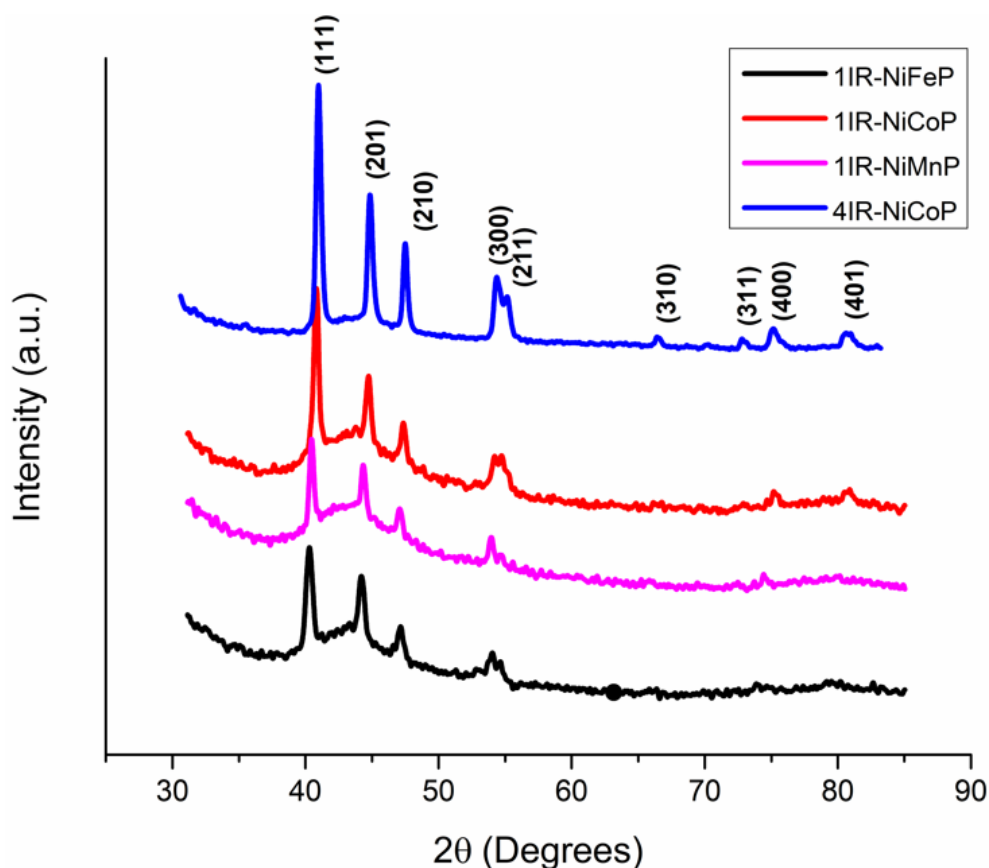
Figure 22. X-ray diffractograms of the AC/Bimetallic TMP composites.

SEM micrographs of AC/Bimetallic TMP specimens are given in Figure 23. In all micrographs, AC serves as a matrix and has second phases on the surface. There are two distinct morphologies in 1IR-NiFeP and 1IR-NiMnP (a, b and c). EDS analysis on certain regions of specimens reveals that the rod-like phase in (a) in region 1 has higher Fe content. In contrast, as given in Table 14, the secondary spherical phase is rich in Ni since the overall concentration of Ni is higher. Bi-modal phase distribution is also seen in 1IR-NiMnP. Bigger spherical precipitates around 300 nm contain

higher Mn amounts; however, EDS taken at the general structure demonstrates higher Ni amounts. Ni-rich phase seems to precipitate as nm range spheres, while the second transition metal determines the other phases' morphology for these two samples. On the contrary, no clear distinction between the morphologies of the phases is detected in 1IR-NiCoP and 4IR-NiCoP (d and e). EDS results also support this observation; inasmuch as general and regional transition metal ratios do not differ in a tremendous amount, Co/Ni at% ratio ranges between 0.90 – 1.10. Therefore, Ni and Co produce the most homogenous bimetallic TMP in this study. Moreover, bimetallic TMP loading shows a significant discrepancy between 1IR-NiCoP and 4IR-NiCoP, in favor of the latter. Not only is the loading amount, but also the size of the TMP phase is bigger in 4IR-NiCoP. It is linked to the greater amount of phosphorus groups in 4IR AC having brought about a high driving force for bimetallic TMP formation.

To characterize the transition metal loading amount of TMP and metals stem from the biomass, ICP-OES was conducted on the active materials (see Table 15). Although transition metal (TM) amount was adjusted to yield 10 wt% of TM in the composite, this value could not be realized in 1IR AC-based composites. In fact, the total TM amount is only 2-3 wt%. However, the total TM amount is even higher than the aimed value (also 10 wt%) in 4IR-NiCoP. This observation is contradictory to the AC/Ni phosphide samples given in the previous chapter, in which the transition metal values in the ICP spectra were in line with the impregnation loadings. There can be two reasons to account for this result. One of them can be the greater amount of phosphorus groups of 4IR AC increasing the yield of the TMP production process. The other may be linked to the mesoporous structure and higher surface area, providing greater nucleation and growth sites for bimetallic TMP.
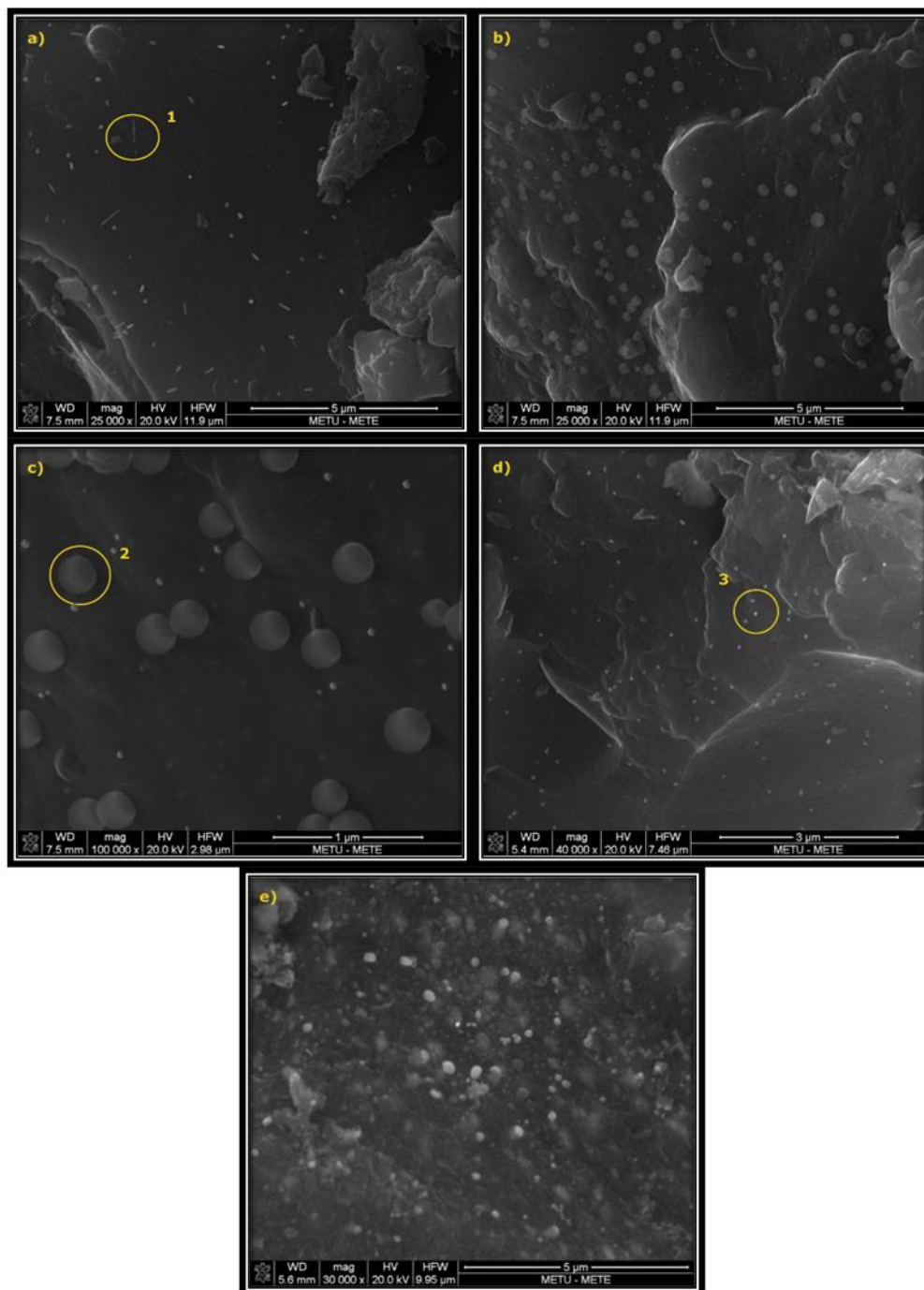
Figure 23. SEM micrographs of a) 1IR-NiFeP, b and c) 1IR-NiMnP, d) 1IR-NiCoP,and e) 4IR-NiCoP

Table 14. Transition metal at% ratios in EDS analysis on the general structure and selected regions.

Regions in Samples	Ni at%	Secondary TM at%	Secondary TM/Ni at% Ratio
Region 1 in 1IR-NiFeP	1.71	2.78	1.63
General in 1IR-NiFeP	1.42	1.24	0.87
Region 2 in 1IR-NiMnP	1.28	5.60	4.38
General in 1IR-NiMnP	1.39	1.08	0.78
Region 3 in 1IR-NiCoP	1.72	1.81	1.05
General in 1IR-NiCoP	0.40	0.38	0.95

Furthermore, the difference between the AC/Ni phosphide and AC/Bimetallic phosphide can stem from the higher formation energy of bimetallic phosphides, which can decrease the overall yield of the TMP formation process. In addition, there are considerable amounts of Na, Ca, K, and Mg attributed to biomass precursors. These metals can have an ameliorating effect on especially OER performance, as one of the studies refers to the better performance of AC to its higher ash and TM content.

Table 15. ICP-OES analysis on AC/Bimetallic TMP samples.

	Ca wt%	Co wt%	Cu wt%	Fe wt%	Mg wt%	Mn wt%	Na wt%	Ni wt%	K wt%
1IR-NiFeP	0.37	-	-	**0.87**	0.07	0.01	1.06	**1.15**	0.02
1IR-NiCuP	0.37	-	**1.850**	0.02	0.07	0.01	1.18	**1.23**	0.02
1IR-NiMnP	0.28	-	-	0.04	0.07	**1.38**	0.94	**1.46**	0.01
1IR-NiCoP	0.20	**1.26**	-	0.02	0.05	0.01	0.61	**1.42**	0.01
4IR-NiCoP	0.28	**5.66**	-	0.05	0.08	0.01	0.90	**6.71**	0.02

To identify surface chemical characteristics and particularly understand the effect of second transition metal in bonding, XPS is conducted on the samples. The complex peak structure in partial scans of secondary transition metals in the AC/bimetallic TMP composite is deconvoluted in Figure 24 (a), (b) and (c). Firstly, the Fe 2p spectrum of 1IR-NiFeP is deconvoluted into five peaks. The peaks at around 712.3 eV and 728.7 eV are assigned to Fe $2p_{3/2}$ and Fe $2p_{1/2}$ components of Fe^{3+}, particularly in oxide form, respectively. The peaks at approximately 709.8 eV and 724.5 eV correspond to Fe $2p_{3/2}$ and Fe $2p_{1/2}$ components of Fe^{2+} in the oxide phase. The little hump at around 708 eV and the peak at around 718.1 eV are linked to Fe-P bonding[89,90]. Moreover, the Mn 2p spectrum of 1IR-NiMnP is deconvoluted into four peaks. The dominant peaks are located around 641.6 eV and 653.8 eV in the $2p_{3/2}$ and $2p_{1/2}$ region in Mn 2p, and these peaks are assigned to the Mn-P bond [91,92]. The peaks at around 644.2 eV and 658.5 eV are set to Mn^{4+}, which stems from surface oxidation. Furthermore, Co 2p in 1IR-NiCoP has 3 peaks, the peaks at around 780.6 eV in $2p_{3/2}$ and 797.3 eV in $2p_{1/2}$ are assigned to Co^{2+}, and the peak at around 784.3 eV is linked to Co^{3+}, both of them in oxides[93,94]. These spectra suggest that the surface of the bimetallic phase is partially oxidized, and the secondary transition metals have mixed-valence states. In addition, the Ni 2p spectrum of these samples has peaks around 855 eV assigned to Ni^{2+}. However, the signal is weak, especially for the 1IR-NiFeP sample, suggesting that the second transition metal mainly governs surface properties. C 1s, O 1s and P 2p spectra of the samples show the effect of surface functional groups on AC (see Appendix, Figure S1). Particularly, P 2p spectra shows a dominant peak around 133 eV, which is attributed to phosphate groups remaining on the surface of AC. Phosphorus in bimetallic TMP should have been at around 129-130 eV; however, the amount of TMP on AC is not adequate to show this peak.
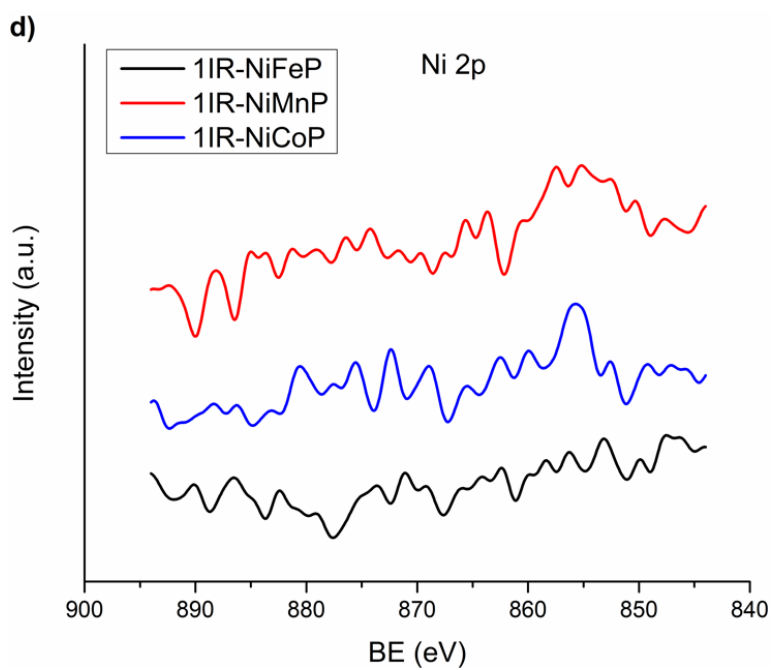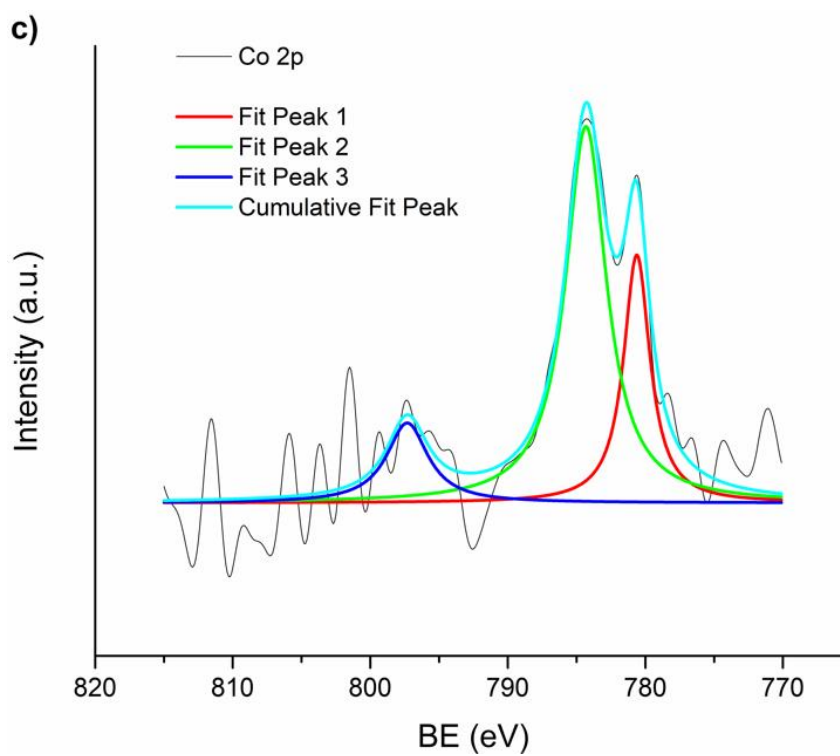
c)

d)
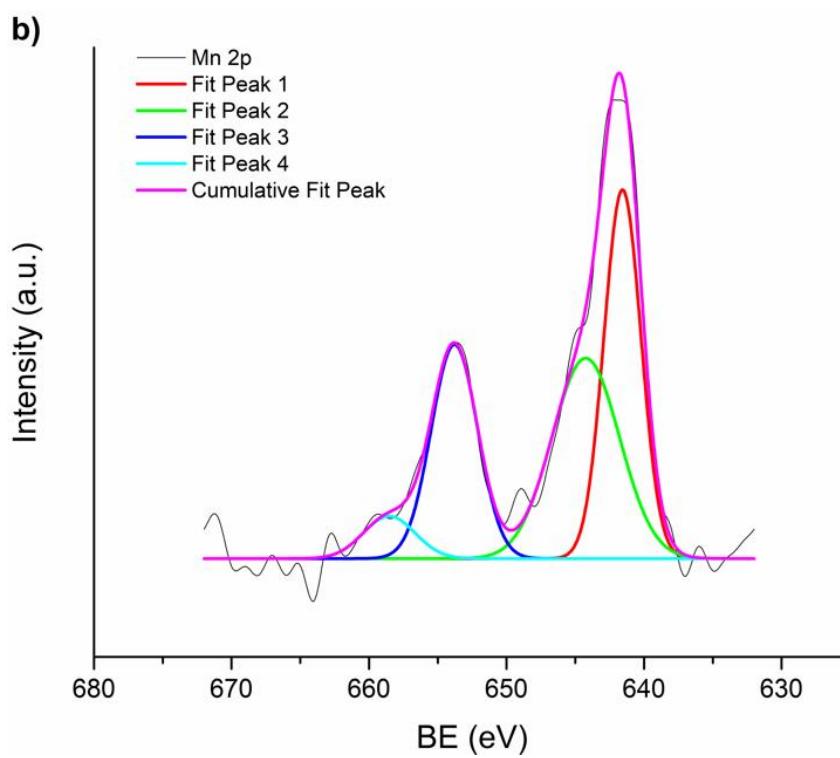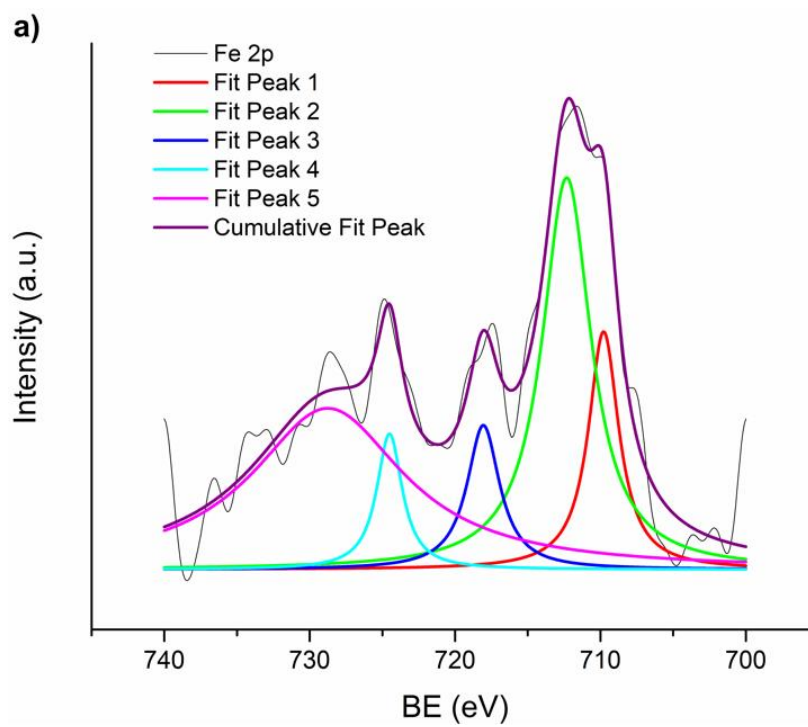
Figure 24. XPS partial scans of a) Fe 2p in 1IR-NiFeP, b) Mn 2p in 1IR-NiMnP, c) Co 2p in 1IR-NiCoP, and d) Ni 2p in 1IR-NiFeP, 1IR-NiMnP, and 1IR-NiCoP samples.

EC performance of AC/Bimetallic TMP composites is given in Figure 25. First, two distinct regions are apparent in cyclic voltammograms in (a) and (b). RDE was utilized to obtain CVs to differentiate the effect of each element in redox potentials. The first region is from -0.5V to 0.2V vs. Hg/HgO, where the CV is quasi rectangular. The rectangular-shaped CV is typical for electrical double-layer capacitors utilizing porous active materials. The rectangular-shaped curve was not attained when only 1IR AC was utilized as active material in RDE (see Appendix, Figure S2). The resistive behavior apparent in CV curve of 1IR AC is attributed to low electrical conductivity of 1IR AC as a result of the low heat treatment temperature. As a consequence, the response on this region is dominated by the textural properties of AC in the composite. The area under the curve, which is a direct remark of the material's capacitance, is close to one another in this region. This result is unexpected since 4IR AC has a mesoporous structure and more surface area compared to 1IR AC to be utilized in electrical double layer formation. The lack of performance enhancement of 4IR AC based composites can be attributed to the high amount of TMP loading and bigger size of them, as evidenced by SEM, partially blocking the porosity. Similar behavior was reported in a study based on the capacitive performance evaluation of AC/MnO_2 composite when MnO_2 loading exceeds a certain level [95]. Moreover, there are oxidation and reduction peaks in the second region, approximately from 0.2V to 0.6V vs. Hg/HgO. The peaks at this region are ascribed to oxidation and reduction of transition metals in bimetallic TMP phases. Particularly, Ni phosphides are well documented with the utilization of Ni^{2+}/Ni^{3+} redox pair involving OH^- ion with exceptional charge storage capabilities [1,96]. It is not abrupt that the addition of secondary transition metal changes the redox mechanism. Indeed, one can realize the difference in peak shapes in CVs, as well as peak potentials in Table 16. Although there are bumps in the reduction region, the oxidation potential cannot be differentiated in the 1IR-NiFeP sample due to a strong tendency to have OER. Both OER tendency and lack of considerable capacitive contribution of redox reactions with OH^- ion are ascribed to the strong affinity of surface Fe to OH^-, preventing Ni from having redox reactions. In 1IR-NiCoP and

62

4IR-NiCoP, there are broad redox peaks. Since Co is also reported to have redox reactions in alkaline medium, it is envisioned that these peaks have contributions from both Ni and Co redox couples. To account for this envisage, Co phosphide on AC was produced with the same method and tested (see Appendix, Figure S3). It demonstrates two small and broad oxidation peaks at around 0.27 and 0.49 V vs. Hg/HgO, and also two reduction peaks at about 0.18 and 0.37 V vs. Hg/HgO, probably pointing out two different mechanisms. There is undoubtedly a contribution of Ni in these processes with the NiCoP phase; the mechanism is yet unclear.
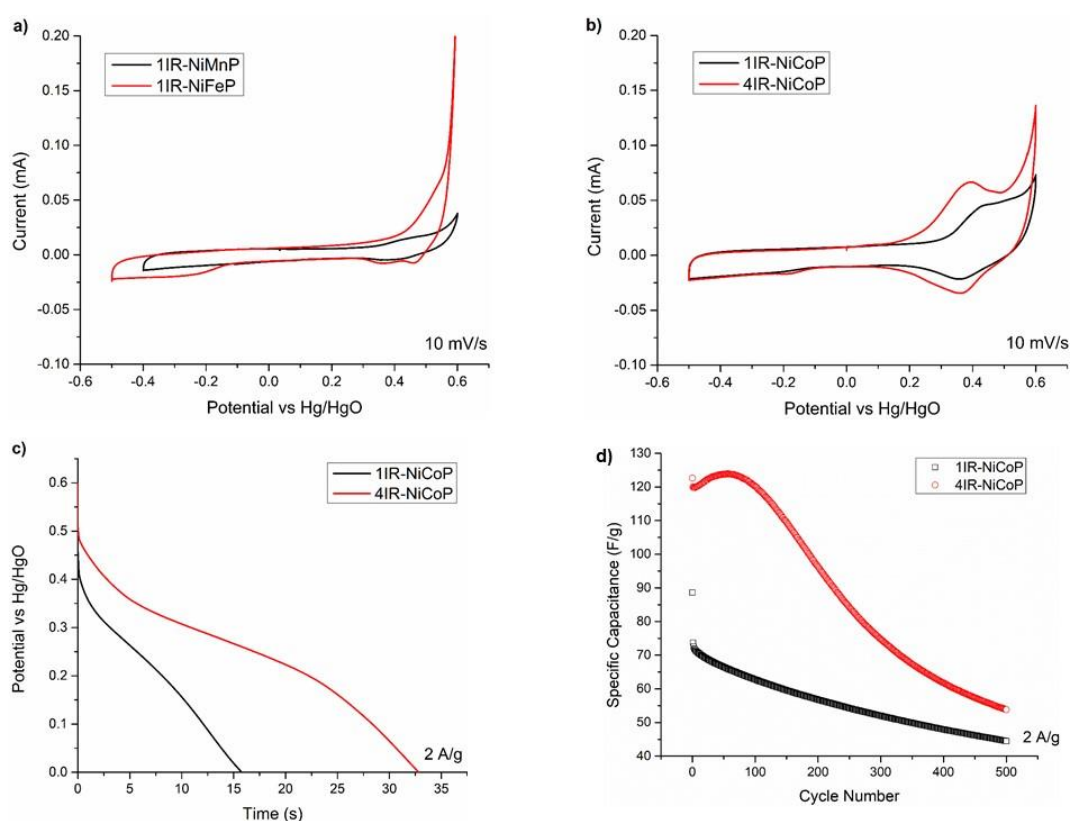
Figure 25. EC performance of AC/Bimetallic TMP active materials. a) CV of 1IR-NiMnP and 1IR-NiFeP samples (RDE, 1M KOH), b) CV of 1IR-NiCoP and 4IR-NiCoP samples (RDE, 1M KOH), c) Galvanostatic discharge curves, and d) Areal capacitance as a function of cycle number of 1IR-NiCoP and 4IR-NiCoP samples.

As far as capacitive properties are concerned, the most promising samples are 1IR-NiCoP and 4IR-NiCoP, resulting from the greater area under the curve in the second region of CV's. Therefore, the capacitive properties of these samples were evaluated

with thicker electrodes using a PTFE binder. Galvanostatic discharge curves and areal capacitance as a function of cycle number in this electrode setup are given in Figure 25 (c) and (d). The discharge curve of 4IR-NiCoP remarks two regions; a plateau around 0.4-0.2 V as a consequence of redox reactions and a linear part between 0.2 – 0V vs. Hg/HgO, originating from double layer formation. The redox region in 1IR-NiCoP is not that apparent, probably due to small bimetallic TMP loading compared to 4IR-NiCoP. The loading difference can also be seen in areal capacitance, resulting in greater values for 4IR-NiCoP. The highest areal capacitance was achieved in this sample with 837 mF/cm^2. However, the increase in loading also has an adverse effect on cycle life, bringing about relatively quick capacitance fade of the same sample.

Table 16. Oxidation and reduction peak potentials in cyclic voltammograms.

	Oxidation Peak (V)	**Reduction Peak (V)**	**ΔEp (mV)**
1IR-NiMnP	0.461	0.404	57
1IR-NiCoP	0.426	0.360	66
4IR-NiCoP	0.395	0.371	24

OER catalysis performance of AC/Bimetallic TMP materials was evaluated by LSV, EIS, and CP, and the results are given in Figure 26. Polarization curves in Figure 26 (a) and overpotential values given in Table 17 demonstrate excellent catalytic activity, specifically in 1IR-NiFeP and 1IR-NiMnP, such low values as 313 and 316 mV, respectively. Moreover, they show 44 mV/dec Tafel slopes indicating fast reaction kinetics. Although not that impressive, the performance of 1IR-NiCoP and 4IR-NiCoP samples are also promising with low overpotentials and minimal Tafel slopes. These specialties of the AC/bimetallic TMP structures as OER catalysts are

64

ascribed to a number of factors. Firstly, both of the composite structure components contribute to OER catalysis. AC prevents agglomeration of TMP and provides electrical conductivity, and serves as catalyst itself due to the porous structure and impurity content. Secondly, TMP materials, especially Ni phosphide are well-known OER catalysts due to their higher electronic conductivity than TMO materials [97]. Thirdly, the second transition metal addition and bimetallic TMP construction alters the electron configuration and provides active sites for OER catalysis. Further, the superior performances of 1IR-NiFeP and 1IR-NiMnP samples are linked to the oxyphilic nature of Fe and Mn elements, increasing the tendency to Fe-O and Mn-O bond formation [98,99].

b)

c)
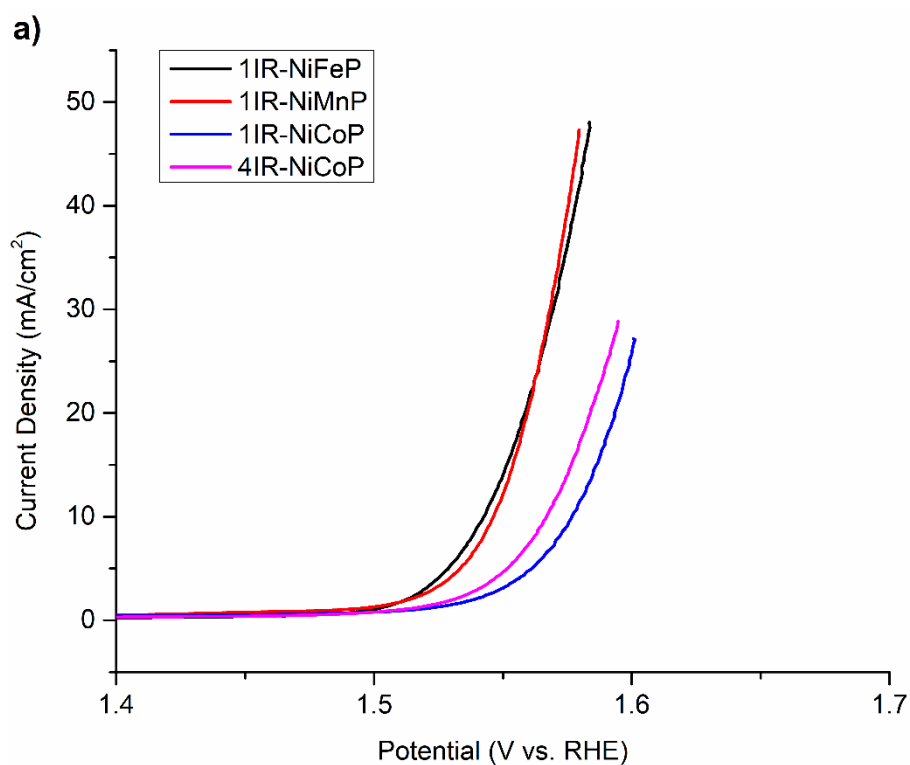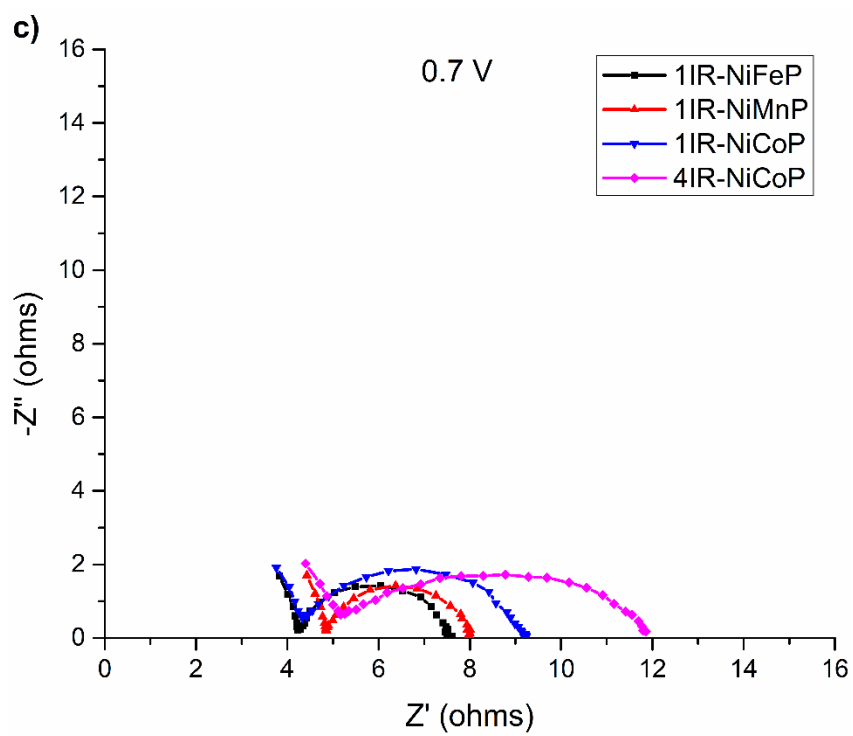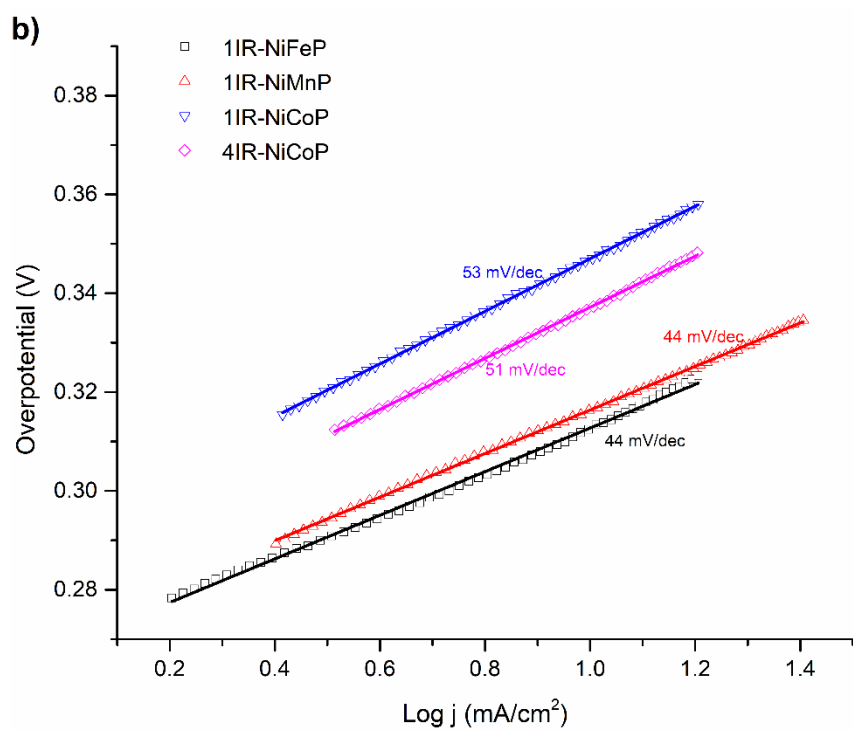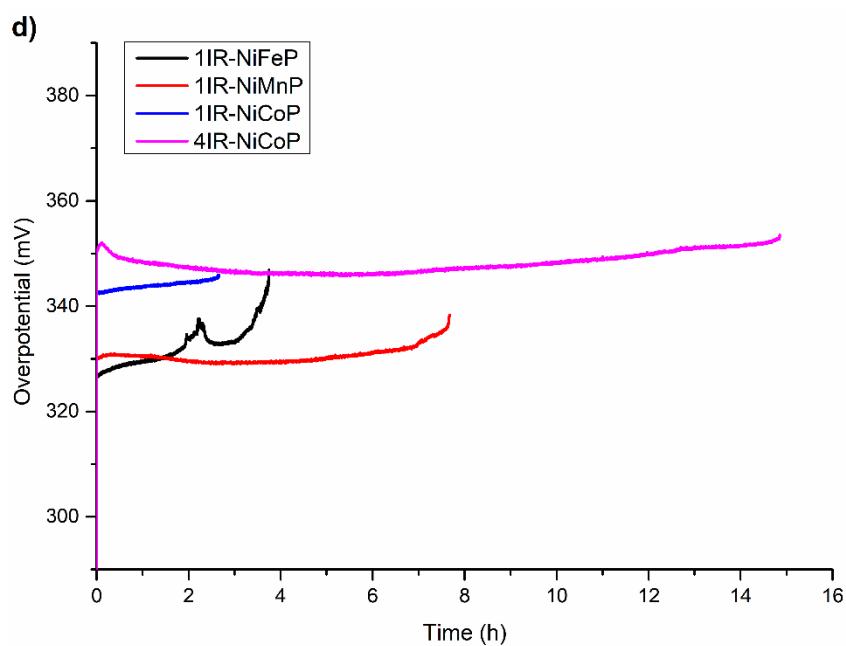
Figure 26. OER performance of AC/Bimetallic TMP catalysts. a) Polarization curves, b) Tafel plots, c) EIS at 0.7 V vs. Hg/HgO, d) Chronopotentiometry at 10 mA/cm^2

Table 17. Overpotential values at 10 mA/cm^2 from LSV curves.

Sample	Overpotential at 10 mA/cm^2 (mV)
1IR-NiFeP	313
1IR-NiMnP	316
1IR-NiCoP	347
4IR-NiCoP	337

EIS results given in the Nyquist plot in Figure 6 (c) are modeled with the equivalent circuit given as R1+C2/R2+C3/R3, to better understand the catalysis process. R1

stands for solution resistance, R2 is ascribed to intrinsic resistivity of the catalyst, and R3 gives the charge transfer resistance of the OER process. The results of this modeling are given in Table 18. Tafel slopes and charge transfer resistances exhibit agreement as a general trend; the ones with faster kinetic have both small Tafel slopes and low R3 values. This situation has one exception; although 4IR-NiCoP has a slightly smaller Tafel slope than 1IR-NiCoP, its R3 value is somewhat higher. Higher TMP loading on AC surface, which increased the intrinsic resistivity of the 4IR-NiCoP sample as the R2 value suggested, is linked to this observation.

Table 18. Equivalent circuit modeling results of EIS at 0.7V vs. Hg/HgO

	1IR-NiFeP	1IR-NiMnP	1IR-NiCoP	4IR-NiCoP
R_1 (ohm)	4.297	4.829	4.347	5.236
C_2 (F)	0.225e-3	0.390e-3	37.220e-6	29.010e-6
R_2 (ohm)	1.564	0.294	1.552	2.418
C_3 (F)	0.546e-3	0.256 2e-3	87.510e-6	0.301e-3
R_3 (ohm)	1.617	2.793	3.011	3.588

Stability tests are conducted on the samples via chronopotentiometry at 10 mA/cm2 (see Figure 26 (d)). The initial overpotential values obtained from LSV are getting higher at the beginning of the test; however, these values start to drop within the first hour of the test in 1IR-NiMnP and 4IR-NiCoP samples. This performance increase is linked to Ni centers of the catalyst, having NiOOH phase formation and rate-boosting Ni-O-P film at the surface [100]. The decrease in overpotential as the stability test goes on is not observed in the 1IR-NiFeP sample. Ni phosphides and the other TMP's have oxide formation in the strong oxidizing environment of OER [26]. In addition, it is claimed that Mn and Fe oxides have too strong an OH- bond strength that diminishes the OER performance [101]. This effect seems to be eliminated in the

1IR-NiMnP sample, possibly due to the activity of Ni centers. Nonetheless, it is seen dramatically in the 1IR-NiFeP sample since XPS results present that Fe surrounds the surface of bimetallic TMP species, which plays a critical role in OER catalysis.

CONCLUSIONS

In this study, biomass-derived AC/Bimetallic TMP composites were produced and tested for EC and OER catalysis for the first time, to the best of our knowledge. The synergistic effect of the composite structure and change in the properties of the TMP phase by the addition of the secondary transition metal provide enhanced performance for both EC and OER catalysis applications. Furthermore, facile method of active material synthesis and corresponding structure enables great activity especially in OER catalysis, which can provide a prospect in an industrial application. There were two AC produced with two impregnation ratios: 1IR and 4IR. N_2 adsorption experiments showed that 1IR AC-based ones have prominently microporosity, while 4IR AC-based ones have microporosity and mesoporosity. XRD results revealed that bimetallic TMP with hexagonal Ni_2P crystal structure is formed in all of the samples. SEM reflected the effect of secondary transition metal and impregnation ratio of AC on the morphologies of the bimetallic TMP phases. XPS was utilized to characterize mainly the valence states of the secondary transition metals, revealing the composites' surface chemical state, which influences both EC and OER catalysis. The most promising active material in EC application was 4IR-NiCoP as far as capacitance is concerned due to high TMP loading and multiple redox sites of NiCoP. However, a relatively rapid capacitance decline should be improved for further utilization. 1IR-NiFeP and 1IR-NiMnP showed excellent catalytic activity in OER with 44 mV/dec Tafel slopes and 313 and 316 mV overpotentials, respectively. This performance was attributed to the contribution of both components of the composite structure to OER catalysis and the oxophylic nature of Fe and Mn elements increasing the activity of the catalyst. Similarity of the

catalytic activity of 1IR-NiFeP and 1IR-NiMnP samples disrupts and goes in 1IR-NiMnP's favor when the stability behaviors are examined. As a result, Co and Mn are found to be the best performing transition metals among the ones chosen in this study, when used with Ni for EC and OER catalyst applications, respectively.

CHAPTER 6

$Ni_xCo_{1-x}P$ SYNTHESIS AND THEIR ELECTROCHEMICAL PERFORMANCE EVALUATION

X-ray diffractogram of the $Ni_xCo_{1-x}P$ samples are given in Figure 27. Consistent with the diffraction experiments with AC composites, the crystal structure is the same as Ni_2P phase (hexagonal, P-62m). Even in the $Ni_{0.25}Co_{0.75}P$ sample with high Co concentration, there is no peak apparent for Co_2P phase (orthorhombic, Pnma, 62). The first apparent distinction in the diffractogram is the shift in 2θ to higher values, when Co concentration increases. This observation is linked to the fact that Co incorporation into the lattice changes the lattice parameters. In fact, it was suggested that Co incorporation decreases the lattice parameter "a", whereas it increases the lattice parameter "c" [102]. The second feature of the diffractogram is the overlapping in the (300) and (002) peaks, when Co concentration increases. As a consequence of contraction and expansion in the lattice parameters, the peaks' positions slightly changed, resulting in an overlapped peak.

SEM micrographs of the $Ni_xCo_{1-x}P$ samples are given in Figure 28. All of the samples consist of agglomerated submicron particles. The size of the particles range from tens of nanometers to micrometer level. The dominant shape of the particles are spherical, although angular shaped particles are also observed. The angular shaped particles are generally seen in the coarsened particles. The coarsening effect is more pronounced as Co concentration increases. In fact, the most homogeneous particle size distribution can be seen in Figure 28 (a), the micrograph of Ni_2P. Although the reason for grain growth in NiCoP samples, especially as the amount of Co increases, is not known exactly, this phenomenon has been reported before [102]. In addition to grain growth, void structures were also observed in Co-rich samples

in the same system. This situation was explained by the difference in diffusivity between nickel and cobalt in the phosphide lattice, creating the Kirkendall effect.

The effect of particle structure on electrochemical behavior is directly related to the electrode preparation procedure. In conventional electrode preparation methods (PTFE mixed with active material, then dough making and kneading), the electrode slurry is not constantly exposed to intense shear force. Therefore, one can assume that this agglomerated structure is largely preserved at the electrode. In this study and in general in studies where OER or ORR catalytic properties are measured, ultrasonic probe treatment (for half an hour in this study) is applied. It was shown that this process breaks the agglomerated structure, increases the active material surface area and creates a dispersed catalyst ink [103]. As a consequence, it can be assumed that the particle size affecting the electrochemical results in this study is the single particle size, not the agglomerate size.
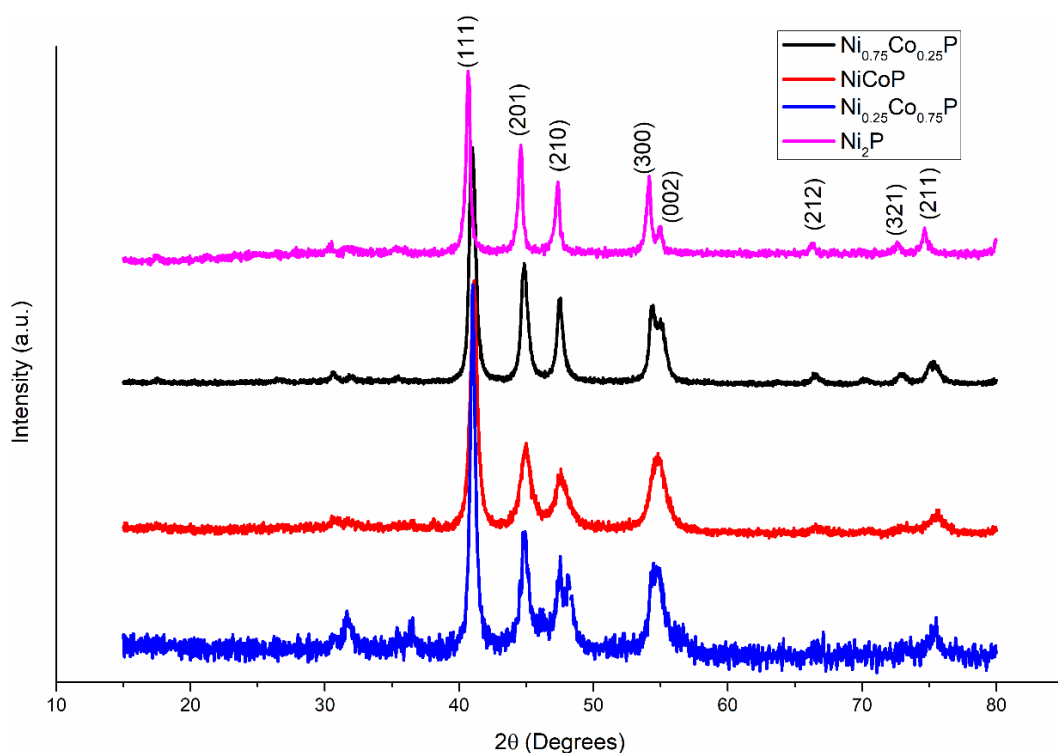

Figure 27. X-ray diffractogram of TMP samples.
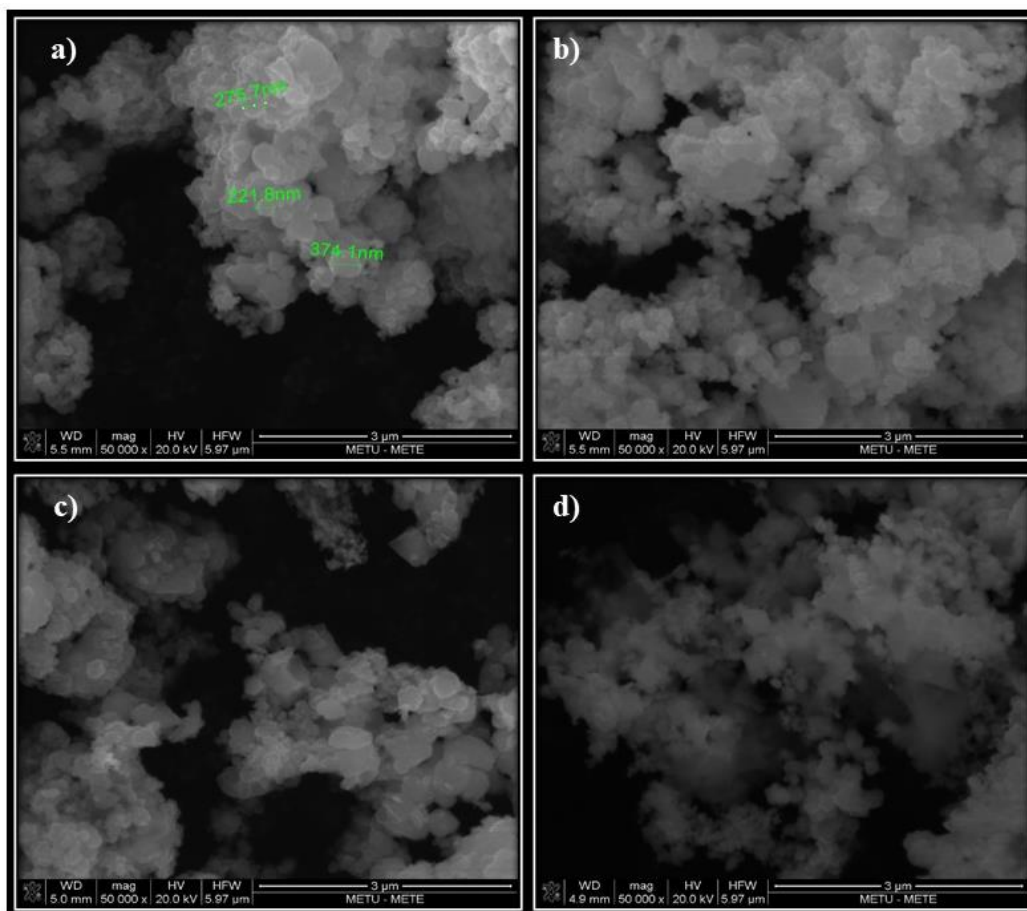
Figure 28. SEM micrographs of (a) Ni_2P, (b) $Ni_{0.75}Co_{0.25}P$, (c) NiCoP, (d) $Ni_{0.25}Co_{0.75}P$.

Cyclic voltammograms of the $Ni_xCo_{1-x}P$ samples are given in Figure 29. As in the first and second chapters of this study, the voltammograms can be divided into two parts. The first part covers the redox reactions in the potential zone greater than 0.1 V vs Hg/HgO; whereas, second part in negative potential region there is no such activity. The shoulder starting from -0.2 V is linked to the ORR activity of the $Ni_xCo_{1-x}P$ active materials. Although they are generally regarded as OER catalysts, it was shown that they also possess ORR catalytic activity [104]. Another observation in this zone is the lack of capacitive contribution. Since the active materials do not incorporate highly porous active materials, the decrease in capacitive contribution compared to samples containing activated carbon is comprehensible.

The part of the voltammogram that includes positive potentials provides information about the redox behavior of active materials. The largest impact on the redox potential of materials comes from the chemical composition of the material. Looking at Table 19, it can be seen that the dominant oxidation peak decreases as the amount of Co increases. This can be attributed to the fact that cobalt has a smaller oxidation potential than nickel in an alkaline environment. As the amount of nickel in the samples increases, the oxidation and reduction potentials become distinct and at a single point, while with the increase in the amount of cobalt it can be seen that they spread to a window of almost 0.4 volts. This is understandable since two different redox couples of cobalt (Co^{2+}/Co^{3+} and Co^{3+}/Co^{4+}) are effective in this region. The mentioned spreading effect is the reason for the high capacitance in the NiCoP sample. It is obvious that the dominant oxidation peak in this sample is related to cobalt. The second oxidation peak is at a potential very close to the Ni oxidation peak (see Figure S4). Further charaterization is needed to reach a full conclusion about the mechanism of the reaction. Moreover, when the cobalt is further increased, the mentioned spreading effect is still seen in the $Ni_{0.25}Co_{0.75}P$ sample, but the capacitance is very low. Although microstructure and bigger particle size also play a role here, the more important thing is that the oxidation and reduction of cobalt did not create as capacitive an effect as that of nickel.

The method of electrode preparation has a drastic effect on both the properties of the CV's and calculated areal capacitance values. Note that the active material is prepared as an ink with Nafion binder and measured in RDE. This method is typically used for electrocatalyst studies. In the method the loading amount per area is small; therefore, areal capacitances are very low when compared the literature. However, the method has the advantage of resolution in CV. Indeed, the studies relying on conventional electrode preparation method do not provide detailed information on reduction and oxidation potentials of $Ni_xCo_{1-x}P$ samples.

Table 19. Oxidation and reduction peak potentials and areal capacitances of the samples.

	Dominant Ox. Peak (V)	Dominant Red. Peak (V)	Areal Capacitance (mF/cm^2)
Ni$_2$P	0.518	0.39	18.5
Ni$_{0.75}$Co$_{0.25}$P	0.455	0.346	15.8
NiCoP	0.418	0.298	19.2
Ni$_{0.25}$Co$_{0.75}$P	0.385	0.32	4.5

The catalytic activities of the Ni$_x$Co$_{1-x}$P samples in OER are measured by LSV, EIS and chronopotentiometry. LSV curves of the samples are given in Figure 30. The OER overpotentials at 10 mA/cm^2 current density for Ni$_{0.25}$Co$_{0.75}$P, NiCoP and Ni$_{0.75}$Co$_{0.25}$P are calculated as 329, 343 and 350 mV, respectively. Contrary to its capacitive effect, Co concentration affect the catalytic activity in OER in a positive manner. In a study on the OER performance of NiCo-LDH, it was argued that Co^{2+} irreversibly transforms to Co^{3+}, which forms CoOOH as a result of surface reconstruction [105]. When this phase is coupled with Ni^{3+}, OER activity increases. However, the effect of Co centers have a bigger impact on the OER activity. Moreover, the high current region in the LSV curves show different behavior for the samples. In NiCoP sample, it shows a typical polarization response; however, in the other samples, some deviations were observed. This observation can be linked to the instability of the electrode at higher currents. The catalyst ink preparation procedure were kept the same to systematically investigate the catalytic properties. However, there are numerous studies highlighting the importance of catalyst ink production parameters including ionomer concentration, shape and morphology of the active materials, ionomer to carbon ratio, dispersion method etc.[106,107]. Since the particle size and morphology are inhomogeneous, some of the electrodes produced by the same ink preparation procedure could not withstand the degrading environment of OER.
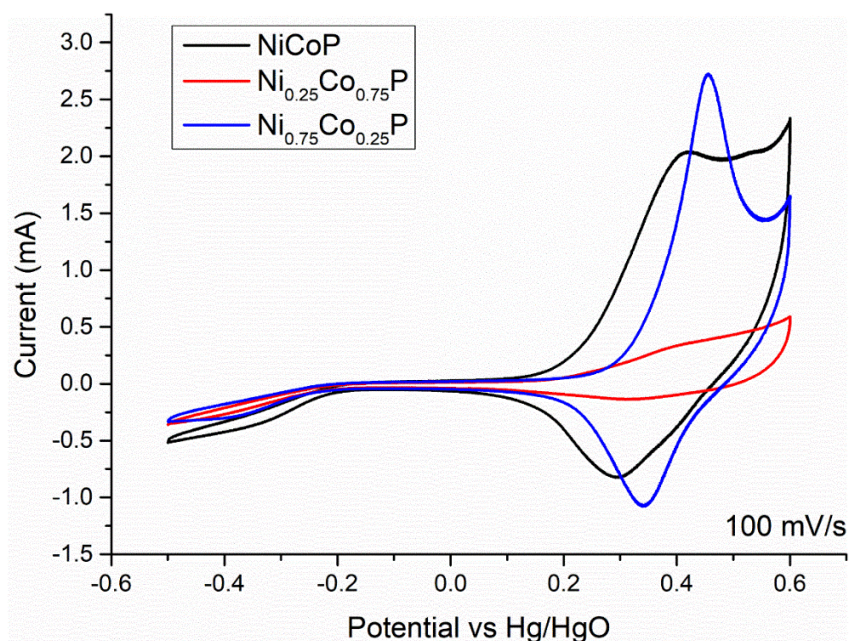
Figure 29. Cyclic voltammograms of $Ni_xCo_{1-x}P$ samples at 1600 rpm in RDE.

The Nyquist plot displayed in Figure 31 illustrates the EIS findings, which are analyzed using an equivalent circuit represented by R1+C2/R2+C3/R3. This model aims to enhance comprehension of the catalysis mechanism. R1 represents the resistance of the solution, R2 denotes the inherent resistivity of the catalyst, and R3 signifies the charge transfer resistance related to the OER process. The outcomes of this modeling can be found in Table 20.

In the Nyquist plots, there are depressed semi circles. Among these depressed semicircles, NiCoP has the lowest radius, implying that this sample has the fastest kinetics. In fact, there is a discrepancy here with the overpotential results from LSV. Normally, the sample that is expected to have the fastest kinetics based on overpotential data is $Ni_{0.25}Co_{0.75}P$. However, according to EIS, this sample has the slowest kinetics. It is thought that the reason for this is the same as the degradation in the polarization curve. Relative to the Hg/HgO electrode, a potential of 0.7 V has sufficient oxygen oxidation rate to disrupt the physical structure of the working electrode. The sample that was least affected by this situation and thus preserved its OER catalytic abilities stood out as NiCoP.
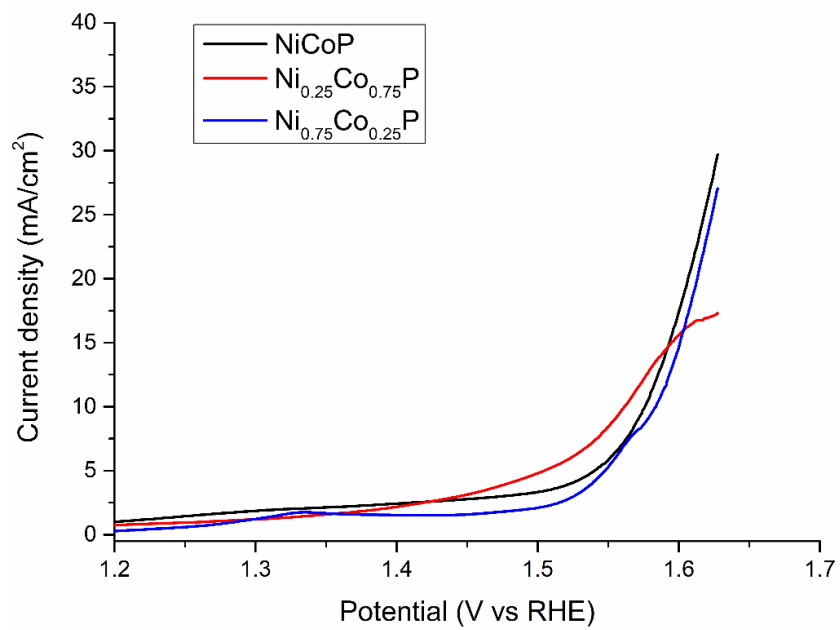
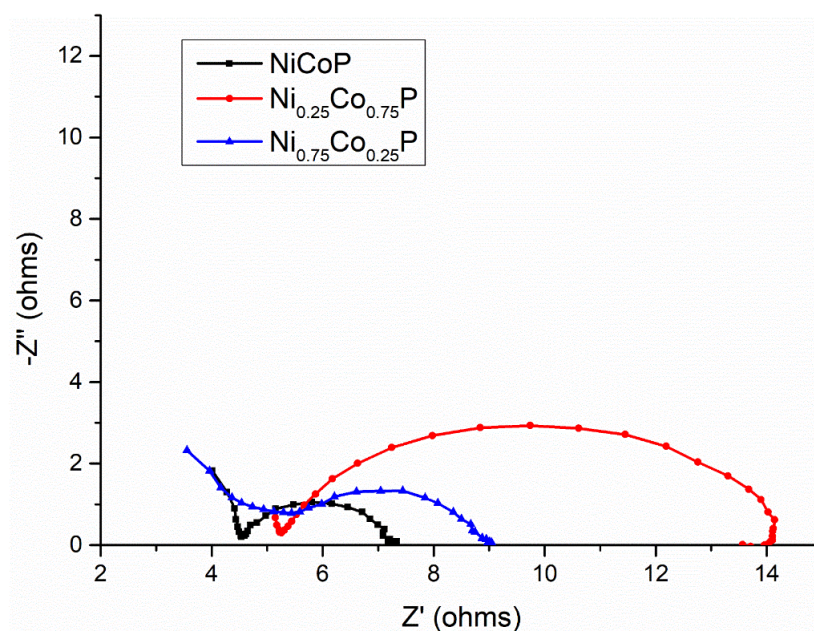Figure 30. LSV curves of $Ni_xCo_{1-x}P$ samples, measured in RDE with 1600 rpm at 5 mV/s.

Figure 31. Nyquist plots of the $Ni_xCo_{1-x}P$ samples, measured in RDE at 1600 rpm at 0.7V vs Hg/HgO.

Table 20. EIS equivalent circuit modelling results for $Ni_xCo_{1-x}P$ samples.

	$Ni_{0.25}Co_{0.75}P$	$Ni_{0.75}Co_{0.25}P$	NiCoP
R1 (ohm)	5.340	4.236	4.573
C2 (F)	49.010e-6	0.112e-3	0.253e-3
R2 (ohm)	3.331	2.845	1.047
C3 (F)	0.240e-3	7.248e-6	0.776e-3
R3 (ohm)	5.096	1.494	1.523

Chronopotentiometry results of $Ni_xCo_{1-x}P$ samples are given in Figure 32. Since chronopotentiometry experiments were performed at 10 mA/cm^2, it is not observed that the electrode degradation effect intensely here. The samples are activated like the samples in other chapters. One can attribute the reason to the –OOH structure forming on the surface and increasing the activity. The NiCoP sample shows the greatest activation, reaching an overpotential performance below 300 mV. Stability durations are much lower than AC/TMP composite structures. As a result, it has been observed that catalyst ink preparation parameters affect not only high current densities in polarization but also stability performance at relatively low current densities.
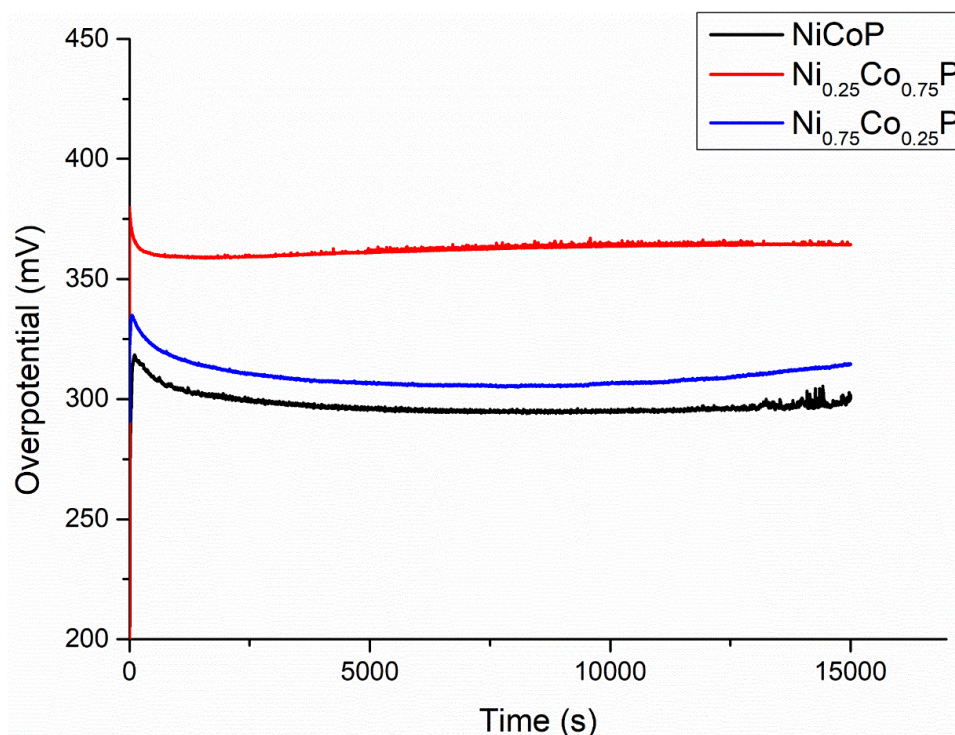
Figure 32. Chronopotentiometry results of $Ni_xCo_{1-x}P$ samples, measured at 10 mA/cm^2 current density.

CONCLUSIONS

In this study, $Ni_xCo_{1-x}P$ materials were synthesized and their capacitive and OER catalytic responses were evaluated. The crystal structure of these materials were characterized by XRD. All the samples have hexagonal, P-62m crystal structure, which is also the structure for Ni_2P. The same crystal structure of the materials in all composition range prove the method of production without second phase (or undetectable amount by XRD). Microstructural analysis by SEM showed that there are agglomerated submicron particles in all the samples. Particle coarsening was seen some of the samples, especially pronounced in the Co rich one.

The CV's reveal insights into the redox behavior of $Ni_xCo_{1-x}P$ active materials. This behavior is largely influenced by the material's chemical composition. Increasing

cobalt content decreases the dominant oxidation peak, attributed to cobalt's lower oxidation potential than nickel in an alkaline environment. As nickel content rises, oxidation and reduction potentials merge, while with cobalt, they spread over a wider voltage range due to multiple cobalt redox couples.

The catalytic activities of $Ni_xCo_{1-x}P$ samples in OER were evaluated using various techniques including LSV, EIS, and chronopotentiometry. LSV curves indicated that $Ni_{0.25}Co_{0.75}P$ exhibited the lowest overpotential for achieving a current density of 10 mA/cm^2, followed by NiCoP and $Ni_{0.75}Co_{0.25}P$. Surprisingly, contrary to its capacitive effect, increasing cobalt concentration positively affected the catalytic activity in OER.

CHAPTER 7

CONCLUSIONS AND FUTURE PERSPECTIVES

In the first part of the study, an AC/TMP composite was produced to be used in EC and as an OER catalyst. Firstly, AC was obtained utilizing the phosphoric acid activation method, resulting in a phosphorus-rich surface with the surface functional groups that influences its properties. Moreover, TMP's are considered promising materials for EC applications, with a great number of studies exploring both their bare and composite forms. Composite structures mainly enhance EC performance when production characteristics are meticulously optimized. Two types of AC were produced with different impregnation ratios: 1IR and 4IR. N_2 adsorption experiments demonstrated that 1IR AC-based samples were primarily microporous, while 4IR AC-based samples showed both micro and mesoporosity. XRD analysis confirmed the formation of TMP with hexagonal Ni_2P and tetragonal $Ni_{12}P_5$ crystal structures in the samples. SEM observations highlighted how the transition metal and AC impregnation ratio impacted the TMP phase morphologies. XPS analysis was used to examine the valence states of secondary transition metals, disclosing the surface chemical state of the composites, which affects both EC and OER catalysis.

In the second phase of the study, biomass-derived AC/bimetallic TMP composites were obtained and tested for applications in EC and OER catalysis. The composite structure's synergistic effect and the changing the TMP phase characteristics by adding a secondary transition metal increased performance in both EC and OER catalysis. Moreover, the straightforward synthesis method and the emerging structure exhibited significant activity, particularly in OER catalysis, giving indication for potential for industrial applications. Two types of AC were produced with different impregnation ratios: 1IR and 4IR. As in the first part of the study, N_2 adsorption experiments indicated that 1IR AC-based samples were primarily microporous, while 4IR AC-based samples exhibited both microporosity and

mesoporosity. XRD results revealed the formation of bimetallic TMP with a hexagonal Ni_2P crystal structure in all samples, no $Ni_{12}P_5$ phase was found. SEM analysis showed the impact of the secondary transition metal and the AC impregnation ratio on the sizes and morphologies of the TMP phases. XPS was utilized for characterization of the valence states of the secondary transition metals, indicating the surface chemical states of the composites, which influence both EC and OER catalysis. The 4IR-NiCoP composite showed the highest capacitance in EC applications due to high TMP loading and multiple redox sites of NiCoP, although its capacitance decrease needs improvement. The 1IR-NiFeP and 1IR-NiMnP composites showed excellent OER catalytic activity with Tafel slopes of 44 mV/dec and overpotentials of 313 and 316 mV, respectively, attributed to the contributions of both components and the oxophilic nature of Fe and Mn. When stability responses were examined, 1IR-NiMnP outperformed 1IR-NiFeP. Therefore, Co and Mn were found to be the best-performing transition metals among those studied for EC and OER catalysis applications, respectively, when combined with Ni.

In the third phase of the study, $Ni_xCo_{1-x}P$ materials were synthesized and tested for their capacitive and OER catalytic responses. The crystal structures of these materials, characterized by XRD, were found to be hexagonal P-62m, similar to Ni_2P. The same and intended crystal structure across all compositions points out a successful production method without detectable secondary phases. SEM microstructural analysis exhibited agglomerated submicron particles in all samples, with some particle coarsening, particularly in the Co-rich samples. CV provided insights into the redox behavior of the $Ni_xCo_{1-x}P$ active materials, which varied with chemical composition. As cobalt content is enhanced, the dominant oxidation peak is reduced, due to cobalt's lower oxidation potential compared to nickel in an alkaline environment. With higher nickel content, oxidation and reduction potentials converged, whereas with higher cobalt content, these potentials spread over a wider potential range due to multiple cobalt redox couples in this potential region. The catalytic activities of the $Ni_xCo_{1-x}P$ samples for OER were assessed using techniques such as LSV, EIS, and chronopotentiometry. LSV curves showed that $Ni_{0.25}Co_{0.75}P$

had the lowest overpotential to achieve a current density of 10 mA/cm², followed by NiCoP and $Ni_{0.75}Co_{0.25}P$. Contrary to its capacitive behavior, increasing cobalt concentration increased the catalytic activity in OER.

In this study, a promising production method was found and it was aimed to obtain more catalytically active and capacitive materials with different strategies. In order to develop this method further, the phases produced on the AC must be controlled in terms of size and morphology. Future studies may aim to better understand and control phosphorus functionalities on the carbon surface. Because being able to control these functionalities can make it possible to produce the subsequent TMP phase in a controlled manner.

REFERENCES

1. Zhou, K. *et al.* Ultrahigh-Performance Pseudocapacitor Electrodes Based on Transition Metal Phosphide Nanosheets Array via Phosphorization: A General and Effective Approach. *Adv. Funct. Mater.* **25**, 7530–7538 (2015).

2. Wang, D., Kong, L. Bin, Liu, M. C., Luo, Y. C. & Kang, L. An Approach to Preparing Ni-P with Different Phases for Use as Supercapacitor Electrode Materials. *Chem. - A Eur. J.* **21**, 17897–17903 (2015).

3. Hou, S. *et al.* Carbon-incorporated Janus-type Ni2P/Ni hollow spheres for high performance hybrid supercapacitors. *J. Mater. Chem. A* **5**, 19054–19061 (2017).

4. Xie, S. & Gou, J. Facile synthesis of Ni2P/Ni12P5 composite as long-life electrode material for hybrid supercapacitor. *J. Alloys Compd.* **713**, 10–17 (2017).

5. Moosavifard, S. E., Kaverlavani, S. K., Shamsi, J. & Bakouei, A. Hierarchical multi-shelled nanoporous mixed copper cobalt phosphide hollow microspheres as a novel advanced electrode for high-performance asymmetric supercapacitors. *J. Mater. Chem. A* **5**, 18429–18433 (2017).

6. Chen, Y. C., Chen, Z. B., Lin, Y. G. & Hsu, Y. K. Synthesis of Copper Phosphide Nanotube Arrays as Electrodes for Asymmetric Supercapacitors. *ACS Sustain. Chem. Eng.* **5**, 3863–3870 (2017).

7. Chen, X., Cheng, M., Chen, D. & Wang, R. Shape-Controlled Synthesis of Co2P Nanostructures and Their Application in Supercapacitors. *ACS Appl. Mater. Interfaces* **8**, 3892–3900 (2016).

8. Elshahawy, A. M. *et al.* Sulfur-doped cobalt phosphide nanotube arrays for highly stable hybrid supercapacitor. *Nano Energy* **39**, 162–171 (2017).

9. Zheng, Z. *et al.* Three-Dimensional Cobalt Phosphide Nanowire Arrays as

Negative Electrode Material for Flexible Solid-State Asymmetric Supercapacitors. *ACS Appl. Mater. Interfaces* **9**, 16986–16994 (2017).

10. Hu, Y. M. *et al.* One-pot hydrothermal synthesis of porous nickel cobalt phosphides with high conductivity for advanced energy conversion and storage. *Electrochim. Acta* **215**, 114–125 (2016).

11. Wan, H. *et al.* One pot synthesis of Ni12P5 hollow nanocapsules as efficient electrode materials for oxygen evolution reactions and supercapacitor applications. *Electrochim. Acta* **229**, 380–386 (2017).

12. Ding, R., Li, X., Shi, W., Xu, Q. & Liu, E. One-pot solvothermal synthesis of ternary Ni-Co-P micro/nano-structured materials for high performance aqueous asymmetric supercapacitors. *Chem. Eng. J.* **320**, 376–388 (2017).

13. Callejas, J. F., Read, C. G., Roske, C. W., Lewis, N. S. & Schaak, R. E. Synthesis, Characterization, and Properties of Metal Phosphide Catalysts for the Hydrogen-Evolution Reaction. *Chem. Mater.* **28**, 6017–6044 (2016).

14. Deng, C., Hong, X., Wang, G., Dong, W. & Liang, B. Research advance of NiCoP-based materials for high-performance supercapacitors. *J. Energy Storage* **58**, 106379 (2023).

15. Jin, Y. *et al.* Preparation of mesoporous Ni2P nanobelts with high performance for electrocatalytic hydrogen evolution and supercapacitor. *Int. J. Hydrogen Energy* **43**, 3697–3704 (2018).

16. He, S. *et al.* 3D nickel-cobalt phosphide heterostructure for high-performance solid-state hybrid supercapacitors. *J. Power Sources* **467**, 228324 (2020).

17. Gao, M., Wang, W. K., Zhang, X., Jiang, J. & Yu, H. Q. Fabrication of Metallic Nickel-Cobalt Phosphide Hollow Microspheres for High-Rate Supercapacitors. *J. Phys. Chem. C* **122**, 25174–25182 (2018).

18. Li, B. *et al.* High energy ball milling to synthesize transition metal vanadates

with boosted lithium storage performance. *Mater. Today Commun.* **37**, (2023).

19. Zhang, M., Du, H., Wei, Z., Zhang, X. & Wang, R. Facile Electrodeposition of Mn-CoP Nanosheets on Ni Foam as High-Rate and Ultrastable Electrodes for Supercapacitors. *ACS Appl. Energy Mater.* **5**, 186–195 (2022).

20. Chebrolu, V. T. *et al.* The one-step electrodeposition of nickel phosphide for enhanced supercapacitive performance using 3-mercaptopropionic acid. *New J. Chem.* **44**, 7690–7697 (2020).

21. Anuratha, K. S. *et al.* High-performance hybrid supercapacitors based on electrodeposited amorphous bimetallic nickel cobalt phosphide nanosheets. *J. Alloys Compd.* **897**, 163031 (2022).

22. Zhang, N. *et al.* High-Performance Flexible Solid-State Asymmetric Supercapacitors Based on Bimetallic Transition Metal Phosphide Nanocrystals. *ACS Nano* **13**, 10612–10621 (2019).

23. Tahir, M. *et al.* Electrocatalytic oxygen evolution reaction for energy conversion and storage: A comprehensive review. *Nano Energy* **37**, 136–157 (2017).

24. Huang, C. J. *et al.* A review of modulation strategies for improving catalytic performance of transition metal phosphides for oxygen evolution reaction. *Appl. Catal. B Environ.* **325**, 122313 (2023).

25. Ramasubramanian, B. *et al.* Progress and Complexities in Metal–Air Battery Technology. *Energy Technol.* **2301375**, 1–22 (2024).

26. Jin, S. Are Metal Chalcogenides, Nitrides, and Phosphides Oxygen Evolution Catalysts or Bifunctional Catalysts? *ACS Energy Lett.* **2**, 1937–1938 (2017).

27. Liang, H. *et al.* Amorphous NiFe-OH/NiFeP electrocatalyst fabricated at low temperature for water oxidation applications. *ACS Energy Lett.* **2**, 1035–

1042 (2017).

28. Shifa, T. A. *et al.* In Situ-Generated Oxide in Sn-Doped Nickel Phosphide Enables Ultrafast Oxygen Evolution. *ACS Catal.* **11**, 4520–4529 (2021).

29. Wang, X., Li, W., Xiong, D., Petrovykh, D. Y. & Liu, L. Bifunctional Nickel Phosphide Nanocatalysts Supported on Carbon Fiber Paper for Highly Efficient and Stable Overall Water Splitting. *Adv. Funct. Mater.* **26**, 4067–4077 (2016).

30. Li, Y. *et al.* A review: Target-oriented transition metal phosphide design and synthesis for water splitting. *Int. J. Hydrogen Energy* **46**, 5131–5149 (2021).

31. Ryu, J., Jung, N., Jang, J. H., Kim, H. J. & Yoo, S. J. In Situ Transformation of Hydrogen-Evolving CoP Nanoparticles: Toward Efficient Oxygen Evolution Catalysts Bearing Dispersed Morphologies with Co-oxo/hydroxo Molecular Units. *ACS Catal.* **5**, 4066–4074 (2015).

32. Chang, J. *et al.* Surface Oxidized Cobalt-Phosphide Nanorods As an Advanced Oxygen Evolution Catalyst in Alkaline Solution. *ACS Catal.* **5**, 6874–6878 (2015).

33. Zhang, G. *et al.* Highly Active and Stable Catalysts of Phytic Acid-Derivative Transition Metal Phosphides for Full Water Splitting. *J. Am. Chem. Soc.* **138**, 14686–14693 (2016).

34. Aziz, S. K. T. *et al.* Bimetallic Phosphides for Hybrid Supercapacitors. *J. Phys. Chem. Lett.* **12**, 5138–5149 (2021).

35. Zhu, Y. P., Liu, Y. P., Ren, T. Z. & Yuan, Z. Y. Self-supported cobalt phosphide mesoporous nanorod arrays: A flexible and bifunctional electrode for highly active electrocatalytic water reduction and oxidation. *Adv. Funct. Mater.* **25**, 7337–7347 (2015).

36. Yu, X.-Y., Feng, Y., Guan, B., (David) Lou, X. W. & Paik, U. Carbon coated porous nickel phosphides nanoplates for highly efficient oxygen

evolution reaction. *Energy Environ. Sci.* **9**, 1246–1250 (2016).

37. Stern, L.-A., Feng, L., Song, F. & Hu, X. Ni2P as a Janus catalyst for water splitting: the oxygen evolution activity of Ni2P nanoparticles. *Energy Environ. Sci.* **8**, 2347–2351 (2015).

38. Chang, J. *et al.* Core-shell structured Ni12P5/Ni3(PO4)2 hollow spheres as difunctional and efficient electrocatalysts for overall water electrolysis. *Appl. Catal. B Environ.* **204**, 486–496 (2017).

39. Man, H. *et al.* Tailored transition metal-doped nickel phosphide nanoparticles for the electrochemical oxygen evolution reaction (OER). *Chem. Commun.* **54**, 8630–8633 (2018).

40. Feng, L. & Xue, H. Advances in Transition-Metal Phosphide Applications in Electrochemical Energy Storage and Catalysis. *ChemElectroChem* **4**, 20–34 (2017).

41. Badruzzaman, A., Yuda, A., Ashok, A. & Kumar, A. Recent advances in cobalt based heterogeneous catalysts for oxygen evolution reaction. *Inorganica Chim. Acta* **511**, 119854 (2020).

42. Hei, J. *et al.* NiFeP nanosheets on N-doped carbon sponge as a hierarchically structured bifunctional electrocatalyst for efficient overall water splitting. *Appl. Surf. Sci.* **549**, 149297 (2021).

43. Hu, F. *et al.* Amorphous Metallic NiFeP: A Conductive Bulk Material Achieving High Activity for Oxygen Evolution Reaction in Both Alkaline and Acidic Media. *Adv. Mater.* **29**, 1–9 (2017).

44. Xu, P. *et al.* Efficient overall water splitting over Mn doped Ni2P microflowers grown on nickel foam. *Catal. Today* **355**, 815–821 (2020).

45. Xu, S. *et al.* Three-dimensional (3D) hierarchical coral-like Mn-doped Ni 2 P e Ni 5 P 4 / NF catalyst for ef fi cient oxygen evolution. **826**, (2020).

46. Chen, T. *et al.* Nanosheet self-assembled NiCoP microflowers as efficient bifunctional catalysts (HER and OER) in alkaline medium. *Int. J. Hydrogen Energy* **46**, 29889–29895 (2021).

47. Liu, Z., Zhang, G., Zhang, K., Liu, H. & Qu, J. Facile Dispersion of Nanosized NiFeP for Highly Effective Catalysis of Oxygen Evolution Reaction. *ACS Sustain. Chem. Eng.* **6**, 7206–7211 (2018).

48. Béguin, F., Presser, V., Balducci, A. & Frackowiak, E. Carbons and electrolytes for advanced supercapacitors. *Adv. Mater.* **26**, 2219–2251 (2014).

49. Yahya, M. A., Al-Qodah, Z. & Ngah, C. W. Z. Agricultural bio-waste materials as potential sustainable precursors used for activated carbon production: A review. *Renewable and Sustainable Energy Reviews* at https://doi.org/10.1016/j.rser.2015.02.051 (2015).

50. Zhi, M., Xiang, C., Li, J., Li, M. & Wu, N. Nanostructured carbon–metal oxide composite electrodes for supercapacitors: a review. *Nanoscale* **5**, 72–88 (2013).

51. Puziy, A. M., Poddubnaya, O. I. & Ziatdinov, A. M. On the chemical structure of phosphorus compounds in phosphoric acid-activated carbon. *Appl. Surf. Sci.* **252**, 8036–8038 (2006).

52. Caturla, F., Molina-Sabio, M. & Rodríguez-Reinoso, F. Preparation of activated carbon by chemical activation with ZnCl2. *Carbon N. Y.* **29**, 999–1007 (1991).

53. Puziy, A. M., Poddubnaya, O. I., Socha, R. P., Gurgul, J. & Wisniewski, M. XPS and NMR studies of phosphoric acid activated carbons. *Carbon N. Y.* **46**, 2113–2123 (2008).

54. An, C. *et al.* Facile synthesis and superior supercapacitor performances of Ni2P/rGO nanoparticles. *RSC Adv.* **3**, 4628–4633 (2013).

55. Parra-Puerto, A. *et al.* Supported Transition Metal Phosphides: Activity Survey for HER, ORR, OER, and Corrosion Resistance in Acid and Alkaline Electrolytes. *ACS Catal.* **9**, 11515–11529 (2019).

56. Zhang, N., Amorim, I. & Liu, L. Multimetallic transition metal phosphide nanostructures for supercapacitors and electrochemical water splitting. *Nanotechnology* **33**, (2022).

57. Theerthagiri, J. *et al.* Recent progress on synthetic strategies and applications of transition metal phosphides in energy storage and conversion. *Ceram. Int.* **47**, 4404–4425 (2021).

58. Jiang, W., Lehnert, W. & Shviro, M. The Influence of Loadings and Substrates on the Performance of Nickel-Based Catalysts for the Oxygen Evolution Reaction. *ChemElectroChem* **10**, 1–9 (2023).

59. Ma, T., Qiu, Y., Zhang, Y., Ji, X. & Hu, P. A. Iron-Doped Ni5P4 Ultrathin Nanoporous Nanosheets for Water Splitting and On-Demand Hydrogen Release via NaBH4 Hydrolysis. *ACS Appl. Nano Mater.* **2**, 3091–3099 (2019).

60. Li, J. *et al.* Highly Efficient and Robust Nickel Phosphides as Bifunctional Electrocatalysts for Overall Water-Splitting. *ACS Appl. Mater. Interfaces* **8**, 10826–10834 (2016).

61. Tang, C., Asiri, A. M., Luo, Y. & Sun, X. Electrodeposited Ni-P Alloy Nanoparticle Films for Efficiently Catalyzing Hydrogen- and Oxygen-Evolution Reactions. *ChemNanoMat* **1**, 558–561 (2015).

62. Liu, L. *et al.* Quasi-layer Co2P-polarized Cu3P nanocomposites with enhanced intrinsic interfacial charge transfer for efficient overall water splitting. *Nanoscale* **11**, 6394–6400 (2019).

63. Chen, L. *et al.* Cobalt layered double hydroxides derived CoP/Co2P hybrids for electrocatalytic overall water splitting. *Nanoscale* **10**, 21019–21024

(2018).

64. Jiang, N., You, B., Sheng, M. & Sun, Y. Electrodeposited Cobalt-Phosphorous-Derived Films as Competent Bifunctional Catalysts for Overall Water Splitting. *Angew. Chemie - Int. Ed.* **54**, 6251–6254 (2015).

65. Lv, X. *et al.* Self-supported Al-doped cobalt phosphide nanosheets grown on three-dimensional Ni foam for highly efficient water reduction and oxidation. *Inorg. Chem. Front.* **6**, 74–81 (2019).

66. Liang, H. *et al.* Plasma-Assisted Synthesis of NiCoP for Efficient Overall Water Splitting. *Nano Lett.* **16**, 7718–7725 (2016).

67. Li, J. *et al.* Mechanistic Insights on Ternary Ni2−xCoxP for Hydrogen Evolution and Their Hybrids with Graphene as Highly Efficient and Robust Catalysts for Overall Water Splitting. *Adv. Funct. Mater.* **26**, 6785–6796 (2016).

68. Zhang, L. *et al.* Rational construction of macroporous CoFeP triangular plate arrays from bimetal–organic frameworks as high-performance overall water-splitting catalysts. *J. Mater. Chem. A* **7**, 17529–17535 (2019).

69. Liu, Y. *et al.* Porous Mn-doped cobalt phosphide nanosheets as highly active electrocatalysts for oxygen evolution reaction. *Chem. Eng. J.* **425**, 131642 (2021).

70. Brunauer, S., Deming, L. S., Deming, W. E. & Teller, E. On a Theory of the van der Waals Adsorption of Gases. *J. Am. Chem. Soc.* **62**, 1723–1732 (1940).

71. Olivares-Marín, M., Fernández-González, C., Macías-García, A. & Gómez-Serrano, V. Porous structure of activated carbon prepared from cherry stones by chemical activation with phosphoric acid. *Energy and Fuels* **21**, 2942–2949 (2007).

72. Nahil, M. A. & Williams, P. T. Pore characteristics of activated carbons

from the phosphoric acid chemical activation of cotton stalks. *Biomass and Bioenergy* **37**, 142–149 (2012).

73. Zhao, J., Yang, L., Li, F., Yu, R. & Jin, C. Structural evolution in the graphitization process of activated carbon by high-pressure sintering. *Carbon N. Y.* **47**, 744–751 (2009).

74. Tian, F. Y., Hou, D., Zhang, W. M., Qiao, X. Q. & Li, D. S. Synthesis of a Ni2P/Ni12P5 bi-phase nanocomposite for the efficient catalytic reduction of 4-nitrophenol based on the unique n-n heterojunction effects. *Dalt. Trans.* **46**, 14107–14113 (2017).

75. Anantharaj, S., Kundu, S. & Noda, S. "The Fe Effect": A review unveiling the critical roles of Fe in enhancing OER activity of Ni and Co based catalysts. *Nano Energy* **80**, 105514 (2021).

76. Zhao, H., Sun, S., Jiang, P. & Xu, Z. J. Graphitic C3N4 modified by Ni2P cocatalyst: An efficient, robust and low cost photocatalyst for visible-light-driven H2 evolution from water. *Chem. Eng. J.* **315**, 296–303 (2017).

77. Saka, C. BET , TG – DTG , FT-IR , SEM , iodine number analysis and preparation of activated carbon from acorn shell by chemical activation with ZnCl2 Journal of Analytical and Applied Pyrolysis BET , TG – DTG , FT-IR , SEM , iodine number analysis and preparation . *J. Anal. Appl. Pyrolysis* **95**, 21–24 (2018).

78. Fanning, P. E. & Vannice, M. A. A DRIFTS study of the formation of surface groups on carbon by oxidation. *Carbon N. Y.* **31**, 721–730 (1993).

79. Gonçalves, R. *et al.* Preparation of activated carbons from cocoa shells and siriguela seeds using H 3 PO 4 and ZnCL 2 as activating agents for BSA and α -lactalbumin adsorption. *Fuel Process. Technol.* **126**, 476–486 (2014).

80. Sych, N. V *et al.* Porous structure and surface chemistry of phosphoric acid activated carbon from corncob. *Appl. Surf. Sci.* **261**, 75–82 (2012).

81.   Puziy, A. M. & Poddubnaya, O. I. Synthetic carbons activated with phosphoric acid I . Surface chemistry and ion binding properties. **40**, 1493–1505 (2002).

82.   Elmouwahidi, A., Bailón-García, E., Pérez-Cadenas, A. F., Maldonado-Hódar, F. J. & Carrasco-Marín, F. Activated carbons from KOH and H3PO4-activation of olive residues and its application as supercapacitor electrodes. *Electrochim. Acta* **229**, 219–228 (2017).

83.   Lv, Z., Zhong, Q. & Bu, Y. In-situ conversion of rGO / Ni 2 P composite from GO / Ni-MOF precursor with enhanced electrochemical property. *Appl. Surf. Sci.* **439**, 413–419 (2018).

84.   Huo, D. *et al.* One-step synthesis of carbon-encapsulated nickel phosphide nanoparticles with efficient bifunctional catalysis on oxygen evolution and reduction. *Int. J. Hydrogen Energy* **46**, 8519–8530 (2021).

85.   Zhang, D. *et al.* Selective synthesis of Ni12P5 and Ni2P nanoparticles: Electronic structures, magnetic and optical properties. *Mater. Sci. Eng. B* **273**, 115389 (2021).

86.   Suárez-García, F., Martínez-Alonso, A. & Tascón, J. M. D. Activated carbon fibers from Nomex by chemical activation with phosphoric acid. *Carbon N. Y.* **42**, 1419–1426 (2004).

87.   Yagmur, E., Ozmak, M. & Aktas, Z. A novel method for production of activated carbon from waste tea by chemical activation with microwave energy. *Fuel* **87**, 3278–3285 (2008).

88.   Quan, C. Nitrogen - doping activated biomass carbon from tea seed shell for CO 2 capture and supercapacitor. 1218–1232 (2020) doi:10.1002/er.5017.

89.   Xiong, D., Wang, X., Li, W. & Liu, L. Facile synthesis of iron phosphide nanorods for efficient and durable electrochemical oxygen evolution. *Chem. Commun.* **52**, 8711–8714 (2016).

90. Xiao, Y. *et al.* Immobilization of Fe-Doped Ni2P Particles Within Biomass Agarose-Derived Porous N,P-Carbon Nanosheets for Efficient Bifunctional Oxygen Electrocatalysis. *Front. Chem.* **7**, 1–11 (2019).

91. Wang, X. *et al.* One-pot synthesis of Mn2P-Mn2O3 heterogeneous nanoparticles in a P, N -doped three-dimensional porous carbon framework as a highly efficient bifunctional electrocatalyst for overall water splitting. *Chem. Eng. J.* **428**, 131190 (2022).

92. Chen, Q. *et al.* Hierarchical Design of Mn2P Nanoparticles Embedded in N,P-Codoped Porous Carbon Nanosheets Enables Highly Durable Lithium Storage. *ACS Appl. Mater. Interfaces* **12**, 36247–36258 (2020).

93. Lukashuk, L. *et al.* Operando Insights into CO Oxidation on Cobalt Oxide Catalysts by NAP-XPS, FTIR, and XRD. *ACS Catal.* **8**, 8630–8641 (2018).

94. Bian, J. & Sun, C. NiCoFeP Nanofibers as an Efficient Electrocatalyst for Oxygen Evolution Reaction and Zinc–Air Batteries. *Adv. Energy Sustain. Res.* **2**, 2000104 (2021).

95. Deng, D., Kim, B. S., Gopiraman, M. & Kim, I. S. Needle-like MnO2/activated carbon nanocomposites derived from human hair as versatile electrode materials for supercapacitors. *RSC Adv.* **5**, 81492–81498 (2015).

96. Du, W. *et al.* New asymmetric and symmetric supercapacitor cells based on nickel phosphide nanoparticles. *Mater. Chem. Phys.* **165**, 207–214 (2015).

97. Sun, M., Liu, H., Qu, J. & Li, J. Earth-Rich Transition Metal Phosphide for Energy Conversion and Storage. *Adv. Energy Mater.* **6**, 1–34 (2016).

98. Man, H.-W. *et al.* Tailored transition metal-doped nickel phosphide nanoparticles for the electrochemical oxygen evolution reaction (OER). *Chem. Commun.* **54**, 8630–8633 (2018).

99. Li, D. *et al.* Efficient Water Oxidation Using CoMnP Nanoparticles Efficient

Water Oxidation Using CoMnP Nanoparticles. (2016) doi:10.1021/jacs.6b01543.

100. Chung, Y. H. *et al.* Anomalous in situ Activation of Carbon-Supported Ni2P Nanoparticles for Oxygen Evolving Electrocatalysis in Alkaline Media. *Sci. Rep.* **7**, 1–8 (2017).

101. Subbaraman, R. *et al.* Trends in activity for the water electrolyser reactions on 3d M(Ni,Co,Fe,Mn) hydr(oxy)oxide catalysts. *Nat. Mater.* **11**, 550–557 (2012).

102. Liyanage, D. R., Danforth, S. J., Liu, Y., Bussell, M. E. & Brock, S. L. Simultaneous Control of Composition, Size, and Morphology in Discrete Ni2-xCox P Nanoparticles. *Chem. Mater.* **27**, 4349–4357 (2015).

103. Takahashi, I. & Kocha, S. S. Examination of the activity and durability of PEMFC catalysts in liquid electrolytes. *J. Power Sources* **195**, 6312–6322 (2010).

104. Dang, C. *et al.* NiCoP based carbon nanotube heterostructure for improved oxygen redox reaction kinetics in Li-O2 batteries. *Electrochim. Acta* **462**, 142771 (2023).

105. Hu, W., Liu, Q., Lv, T., Zhou, F. & Zhong, Y. Impact of interfacial CoOOH on OER catalytic activities and electrochemical behaviors of bimetallic CoxNi-LDH nanosheet catalysts. *Electrochim. Acta* **381**, (2021).

106. Yang, D. *et al.* Influence of the dispersion state of ionomer on the dispersion of catalyst ink and the construction of catalyst layer. *Int. J. Hydrogen Energy* **46**, 33300–33313 (2021).

107. Ren, H., Meng, X., Lin, Y. & Shao, Z. Structural stability of catalyst ink and its effects on the catalyst layer microstructure and fuel cell performance. *J. Power Sources* **517**, 230698 (2022).

APPENDICES

A. C 1s, O 1s, P 2p XPS Scans of the AC/Bimetallic TMP Materials
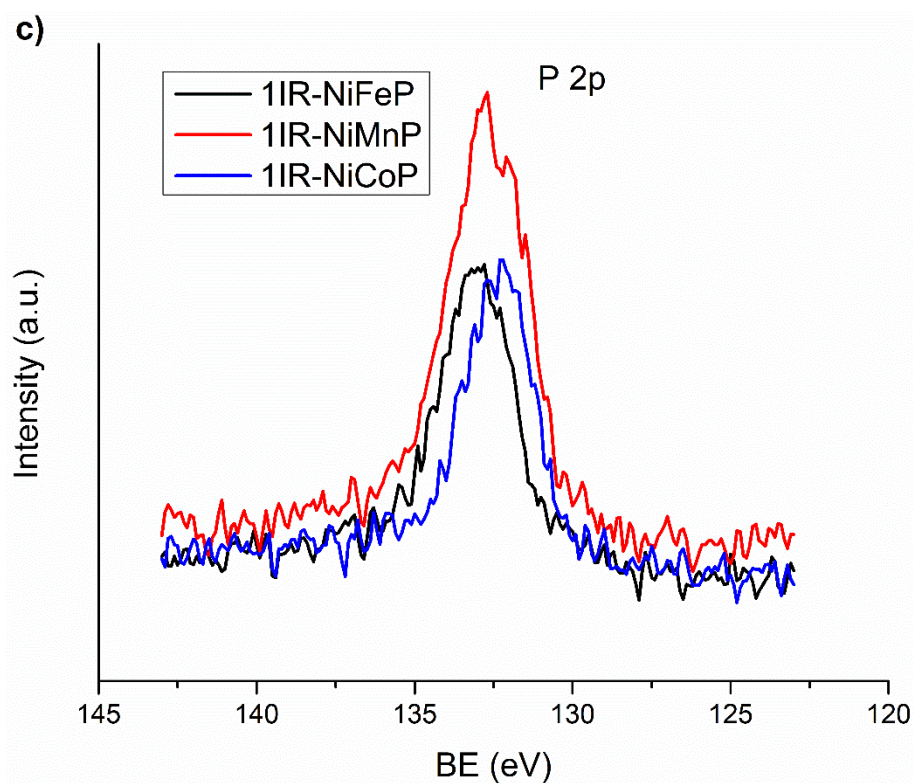
c)
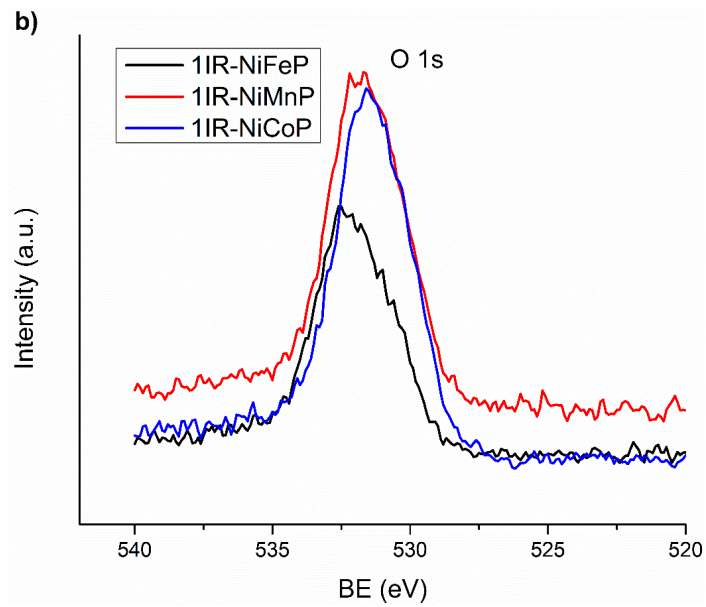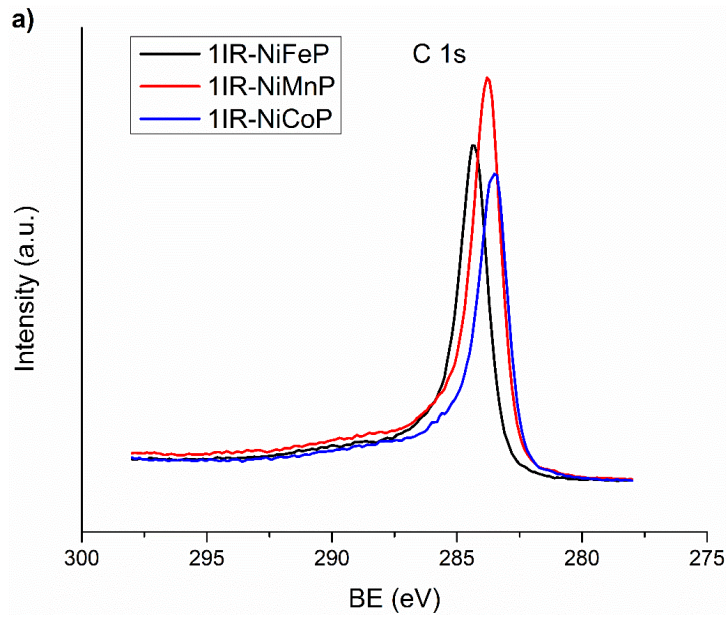
Figure S1. (a) C 1s, (b) O 1s, (c) P 2p spectra of AC/Bimetallic TMP materials.

Above given spectra indicates that surface functional groups are present on the surface of the AC. Particularly, P 2p spectra has a peak at around 133 eV, which is linked to the remaining phosphate groups at the surface. Metal-P bonding should have a peak around 129 eV; however, it is suppressed by the remaining phosphate groups.

Cyclic voltammograms of pure AC and AC-NiCoP are given in Figure S2. Resistive behavior and limited area under the curve in pure AC are attributed to low electrical conductivity.

B. Cyclic Voltammograms of 1IR and 1IR-CoP

It shows similar behavior as AC/Bimetallic TMP's given in the article at negative potentials; however, there are additional oxidation and reduction peaks at the positive potentials.
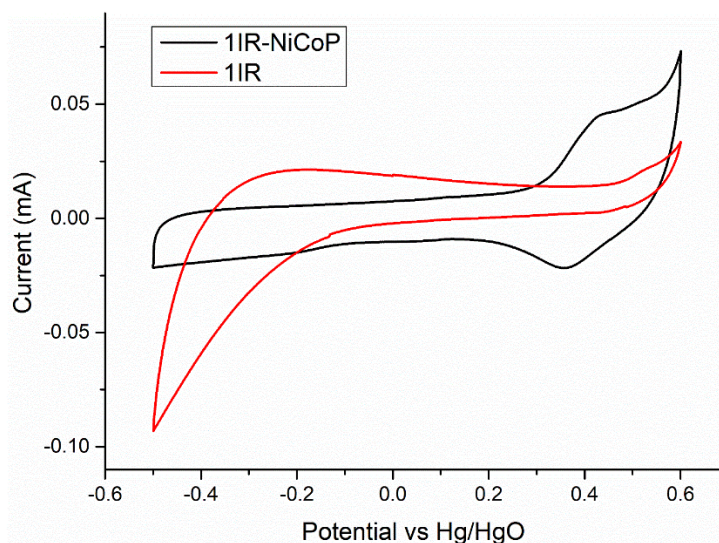

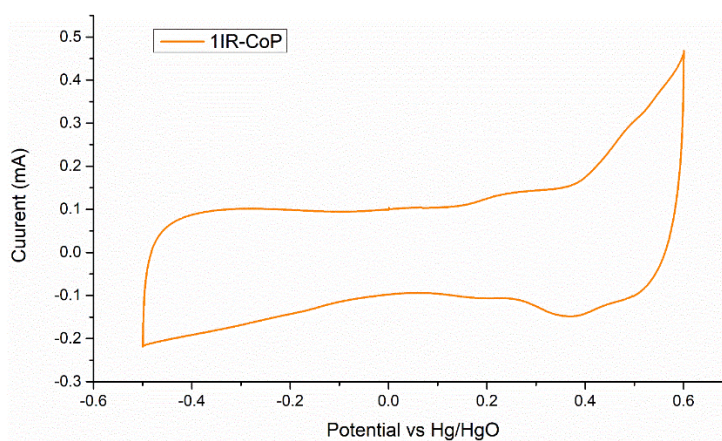Figure S2. CV of 1IR and 1IR-NiCoP at 10 mV, in RDE with 1M KOH.

Figure S3. CV of 1IR-CoP at 10 mV/s, in RDE with 1M KOH.
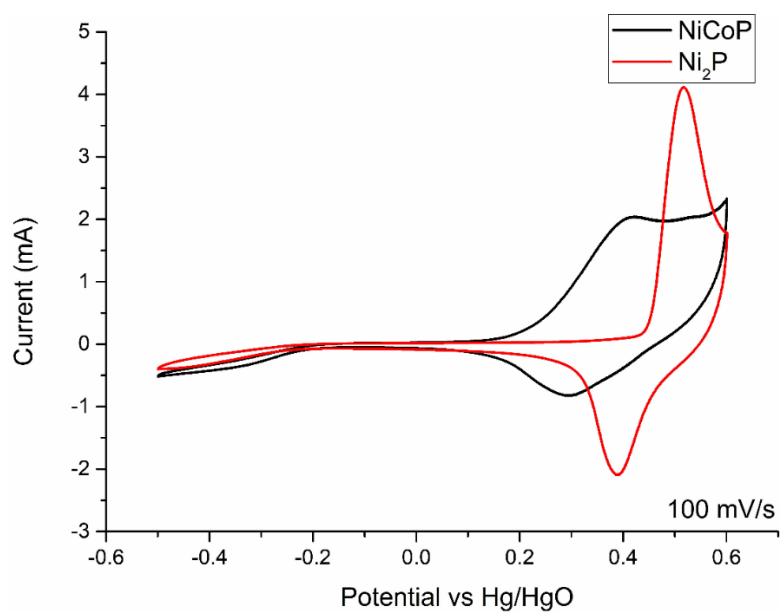
C. CV and LSV Results of AC/Bimetallic TMP Materials

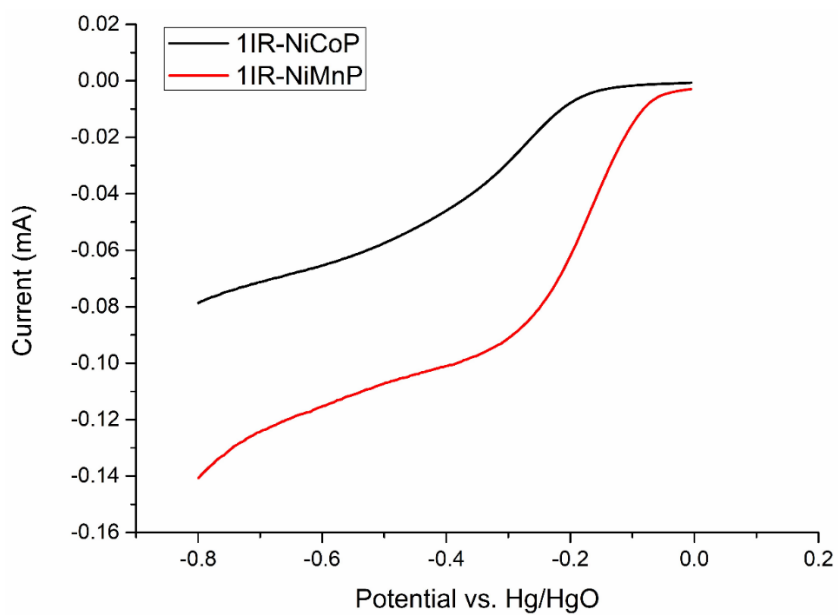Figure S4. CV of NiCoP and Ni$_2$P at 100 mV, in RDE with 1M KOH.

Figure S5. LSV of the AC/TMP samples, with 5mV/s scan rate, RDE with 1 M KOH

CURRICULUM VITAE

Surname, Name: Köse, Kadir Özgün

EDUCATION

Degree	Institution	Year of Graduation
MS	METU Metallurgical and Materials Engineering	2017
BS	METU Metallurgical and Materials Engineering	2014
High School	S.A.K Anatolian High School, Uşak	2006

FOREIGN LANGUAGES

Advanced English

PUBLICATIONS

1. Köse, K. Ö., Pişkin, B., & Aydınol, M. K. (2018). Chemical and structural optimization of ZnCl2 activated carbons via high temperature CO2 treatment for EDLC applications. *International Journal of Hydrogen Energy*, *43*(40), 18607-18616.

2. Köse, K. Ö., & Aydınol, M. K. (2022). Development of activated carbon/bimetallic transition metal phosphide composite materials for electrochemical capacitors and oxygen evolution reaction catalysis. *International Journal of Energy Research*, *46*(15), 22078-22088.